SLOVAK UNIVERSITY OF TECHNOLOGY IN BRATISLAVA

Faculty of Electrical Engineering and Information Technology

Reg. No.: FEI-104400-47586

Radiation Damage Studies of the ePix100 Detector at the EuXFEL

Dissertation thesis

2021

Ing. Ivana Klačková

SLOVAK UNIVERSITY OF TECHNOLOGY IN BRATISLAVA

Faculty of Electrical Engineering and Information Technology

Reg. No.: FEI-104400-47586

Radiation Damage Studies of the ePix100 Detector at the EuXFEL

Dissertation thesis

Study programme: Physical Engineering
Study field: Electrical and Electronics Engineering
Training workplace: Institute of Nuclear and Physical Engineering
Supervisor: doc. Ing. Andrea Šagátová, PhD.
Consultant: Dr. Steffen Hauf, Dr. Markus Kuster

Bratislava 2021 **Ing. Ivana Klačková**

Slovak University of Technology in Bratislava
Institute of Nuclear and Physical Engineering

Faculty of Electrical Engineering and Information Technology
Academic year: 2020/2021
Reg. No.: FEI-104400-47586

DISSERTATION THESIS TOPIC

Student:	**Ing. Ivana Klačková**
Student's ID:	47586
Study programme:	Physical Engineering
Study field:	Electrical and Electronics Engineering
Thesis supervisor:	doc. Ing. Andrea Šagátová, PhD.
Consultant:	Dr. Steffen Hauf, Dr. Markus Kuster
Workplace:	INPE FEEIT SUT & European XFEL, Germany

Topic: **Radiation Damage Studies of the ePix100 Detector at the EuXFEL**

Language of thesis: English

Specification of Assignment:

The aim of the PhD. thesis rests in the experimental characterization of the semiconductor pixel detector ePix100 at the EuXFEL. The experimental testing is aimed at radiation hardness of the detector to estimate its life-time at particular experiments.
1.Describe detector parameters from which radiation damage effects could be estimated and introduce the tools to analyze and characterize radiation induced effects.
2. Perform the radiation hardness tests of the ePix100 detector in the EuXFEL radiation environment.
3. Calculate the absorbed dose during the test duration and analyse impact of the dose to detector components.
4. Explain observed radiation damage effects for specific sensor design.
5. Evaluate the dose limit reducing detector operation parameters to such extent that they no longer meet pre-requirements for reliable scientific data production.
6. Estimate on the lifetime of EuXFEL detector systems based on the conducted experiments.

Assignment procedure from:	30. 08. 2017
Date of thesis submission:	30. 06. 2021

Ing. Ivana Klačková
Solver

prof. Ing. Vladimír Nečas, PhD.
Head of department

prof. Ing. Márius Pavlovič, PhD.
Study programme supervisor

Statutory Declaration

I herewith declare that I have composed the present thesis myself and without the use of any other than the cited sources and aids. The thesis in the same or similar form has not been used to achieve an academic grading and has not been published elsewhere.

________________	____________________________
date	Ivana Klačková

Acknowledgements

I would like to acknowledge the European XFEL in Schenefeld, Germany, to fund the work presented in this thesis and for the provision of an X-ray free-electron laser beam time.

I want to thank my supervisor Assoc. Prof. Andrea Šagátová for her continuous support, motivation and encouragement throughout my studies. Her dedication to research and her students were always an inspiration to me.

I would like to express my genuine gratitude to Dr. Markus Kuster for granting me the opportunity to work on the PhD project within the detector operations group. I am very grateful for his invaluable advice, supervision, and exciting discussions, which taught me to scrutinize every gained result. His profound knowledge has given me insight into the semiconductor detectors' mysteries and helped me improve my understanding of the related physical phenomena.

I would like to sincerely thank Dr. Steffen Hauf for his guidance, supervision and immense knowledge he has to offer in the field of data analysis and semiconductor detectors. His excellent advice, suggestions and ideas were always beneficial and always pushed me forward.

Many thanks go to the HED instrument team to support the realization and execution of the radiation damage experiment. Without their effort, the experiment would not have succeeded. Especially, I thank Dr. Sebastian Göde for the coordination and ideas on the experiment and Dr. Valerio Cerantola for his support throughout the experiment and training on the ePix100a operation.

I thank Dr. Theophilos Maltezopoulos for his support in analyzing the x-ray gas monitor data and the discussions accompanying it.

I would like to acknowledge SLAC National Accelerator Laboratory for providing the ePix100a detector for the conducted experiment. Moreover, I want to thank Dr. Angelo Dragone, Dr. Christopher J. Kenney and Dr. Julie Segal for the in-depth discussion on the gained results.

Special thanks belong to my colleagues from the detector operations group who were always there to offer a helping hand, give advice or have long discussions on various topics, sometimes even without coffee. I am happy to be part of this team.

Finally, I wish to thank my parents for believing in me and last but not least to my wife Veronika, who had to endure all my ups and downs, for her patience, kindness, love and support during all these years.

Abstrakt

SLOVENSKÁ TECHNICKÁ UNIVERZITA V BRATISLAVE

FAKULTA ELEKTROTECHNIKY A INFORMATIKY

ÚSTAV JADROVÉHO A FYZIKÁLNEHO INŽINIERSTVA

Študijný program:	Fyzikálne inžinierstvo
Autor:	Ing. Ivana Klačková
Vedúci práce:	doc. Ing. Andrea Šagátová, PhD.
Vedúci experimentu:	Dr. Steffen Hauf, Dr. Markus Kuster

European X-ray Free Electron Laser (EuXFEL), európsky röntgenový laser voľných elektrónov (ďalej len röntgenový laser), je v súčasnosti najväčší zdroj röntgenového laserového žiarenia na svete, ktorý sa vyznačuje vysokou brilanciou a ultrakrátkymi pulzami s vysokou opakovacou frekvenciou. Prevádzkovanie detektora v jeho radiačnom poli predstavuje pre detektor a jeho komponenty vysoké riziko radiačného poškodenia. Štúdium poškodenia indukovaného žiarením je nevyhnutné pre pochopenie jeho vplyvu na kvalitu meraní realizovaných detektorom, a tiež na odhad životnosti takéhoto detektora. Cieľom práce bolo vyhodnotenie účinkov radiačného poškodenia na detektor ePix100a. Ide o detektor, ktorý je súčasťou ePix platformy zastrešujúcej rôzne typy hybridných pixelových detektorov vyvíjaných pre použitie na röntgenových laserových zariadeniach. V EuXFEL sa používa na dvoch experimentálnych staniciach. Detektor ePix100a bol ožarovaný priamym a čiastočne odtieneným röntgenovým laserovým zväzkom za kontrolovaných podmienok. Účelom bolo systematické štúdium vplyvu radiáciou indukovaného poškodenia na operačné parametre detektora. V štúdii sme sledovali a vyhodnocovali parametre, ktoré sú podstatné pre zabezpečenie správneho fungovania detektora počas vedeckých experimentov, ako napríklad ofset, šum, konverzný faktor, alebo energetické rozlíšenie. Pri experimente sme pozorovali radiačné poškodenie nielen senzora, ale aj vyčítavacej elektroniky. V polovodičovom senzore detektora sa radiačné poškodenie prejavilo najmä nárastom zvodového prúdu. V prípade vyčítavacej elektroniky sa poškodenie prejavilo ako zmena v konverznom faktore. Získané výsledky sa použili na odhad životnosti detektora pri jeho dlhodobom používaní. Výrazné zníženie dynamického rozsahu ($R_{\mathrm{DR}} > 50\%$) sa očakáva pre absorbovanú dávku $> 7.4\,\mathrm{MGy}$ pre integračný

čas $t_{\mathrm{Int}} = 50\,\mu$s na rozhraní Si-SiO$_2$ a pre $t_{\mathrm{Int}} = 800\,\mu$s je hraničná dávka 131 kGy. Z týchto odhadov je zrejmé, že ePix100a môže byť používaný niekoľko rokov bez výrazného zhoršenia parametrov za predpokladu, že intenzita röntgenového laserového zväzku pri experimentoch nepresiahne dynamický rozsah detektora o niekoľko rádov. Získané výsledky poskytujú cenné informácie pre používanie detektora ePix100a na podobných röntgenových laserových zariadeniach. Pozorovania a závery plynúce z tejto práce sú tiež relevantné pre budúci vývoj radiačne odolnejšieho detektora pre danú aplikáciu.

Kľúčové slová: detektory RTG žiarenia, radiačné poškodenie polovodičových detektorov, charakterizácia detektora, röntgenový laser voľných elektrónov

Abstract

SLOVAK UNIVERSITY OF TECHNOLOGY IN BRATISLAVA

FACULTY OF ELECTRICAL ENGINEERING AND INFORMATION TECHNOLOGY

INSTITUTE OF NUCLEAR AND PHYSICAL ENGINEERING

Study Programme:	Physical Engineering
Author:	Ing. Ivana Klačková
Thesis Supervisor:	Assoc. Prof. Andrea Šagátová, PhD.
Experiment Supervisors:	Dr. Steffen Hauf, Dr. Markus Kuster

In September 2017, the world's fastest and most brilliant X-ray free-electron laser facility came into operation - the European X-ray Free Electron Laser (EuXFEL). It is located in northern Germany, in the Hamburg metropolitan area. The European XFEL is an international research facility, delivering an X-ray beam with unique properties and opening up new areas of scientific studies. Spatially coherent X-ray flashes in the energy range from 0.25 keV to 25 keV are provided in a unique time structure with pulses arranged in trains containing up to 2700 pulses every 100 ms with a pulse repetition rate of 4.5 MHz. The time structure, X-ray energy range, and very high intensity of the FEL beam pose demanding requirements on the EuXFEL's imaging detectors. High radiation tolerance is among the requirements of the detector system in use. Detector operation in the radiation environment of an X-ray source of high brilliance, high repetition rate, and ultra-short pulses poses a high risk of radiation damage to a detector and its components. Knowledge about radiation-induced damage is vital for understanding its influence on the quality of scientific data and a detector's lifetime. This thesis aims to evaluate the effects of radiation-induced damage on the ePix100a detector. The ePix100a is a member of the ePix detector family, providing hybrid pixel detectors to support various applications at FEL facilities. At the European XFEL, it is used at two scientific instruments: the High Energy Density (HED) instrument and the Material Imaging and Dynamics (MID) instrument. The ePix100a detector was irradiated under controlled conditions with a direct, attenuated FEL beam to systematically study the effects of the induced radiation damage on various detector parameters that

are commonly used as indicators of the good scientific performance of the detector, i.e., offset, noise, gain, and energy resolution. We have observed damage in the sensor and the Application Specific Integrated Circuit (ASIC). The observed radiation-induced damage effects in the sensor were mainly due to an increase in the leakage current. We have observed changes in detector gain on the ASIC level due to damage induced on the pixels' pre-amplifiers. Based on the obtained results, the limits for the long-term operation of the ePix100a at EuXFEL and other light sources in terms of its scientific performance have been assessed. Significant reduction of the dynamic range, i.e. $R_{\mathrm{DR}} > 50\%$ for $t_{\mathrm{Int}} = 50\,\mu\mathrm{s}$ is expected with a dose absorbed in the Si-SiO_2 interface $> 7.4\,\mathrm{MGy}$ and for $t_{\mathrm{Int}} = 800\,\mu\mathrm{s}$ at $131\,\mathrm{kGy}$. We have determined that the ePix100a can be used without significant degradation of its operating performance for several years if the incident photon beam intensities do not outperform the detector's dynamic range by several orders of magnitude. The results we have obtained provide valuable input for the ePix100a operation at FEL facilities. The observations and conclusions made are also relevant for future optimization towards radiation-harder detectors for photon science.

Key words: X-ray detectors, Radiation damage of semiconductor detectors, Detector performance characterization, Free-electron laser

Contents

1 Introduction **27**

1.1 The European XFEL . . . 27

1.2 Imaging Detectors at the EuXFEL . . . 30

1.2.1 Detector Requirements . . . 30

2 Silicon as Semiconductor Material **35**

2.1 Introduction to Semiconductors . . . 35

2.1.1 Intrinsic Silicon . . . 37

2.1.2 Extrinsic Silicon . . . 39

2.2 Interaction of X-rays with Silicon . . . 41

3 Basic Semiconductor Devices **45**

3.1 The p-n Junction . . . 45

3.2 Metal-Oxide-Semiconductor Structure . . . 51

3.2.1 Operation modes . . . 52

3.2.2 Capacitance-Voltage Characteristics . . . 56

3.2.3 Discussion to p-Type MOS . . . 58

3.2.4 Si-SiO_2 MOS Structure . . . 59

4 X-ray Radiation Induced Defects in Silicon **61**

4.1 The Si-SiO_2 Interface . . . 61

4.2 Physical Processes Underlying Surface Defects Induced by Radiation 65

4.2.1 Electron-Hole Pair Generation . . . 67

4.2.2 Hole Transport . . . 68

4.2.3 Oxide Traps . . . 69

4.2.4 Radiation-Induced Interface Traps . . . 71

4.3 Factors Influencing Surface Damage . . . 72

4.3.1 Oxide Layer Thickness . . . 72

4.3.2 Dose-Rate Effects 73
4.3.3 Time and Temperature Effects 74
4.4 Effects of Induced Radiation on MOS Devices 75
4.4.1 Threshold Voltage Change 75
4.4.2 Increase of Leakage Current 75
4.4.3 Decrease of Charge Transfer Efficiency 75
4.4.4 Decrease of Breakdown Voltage 76
4.4.5 Decrease of Charge Carrier Mobility 76

5 Dissertation Thesis Aims 79

6 Detector Performance Parameters Relevant for Radiation Damage 81
6.1 Dark Signal 81
6.2 Dynamic Range 82
6.3 Energy Resolution 83
6.4 Signal-To-Noise Separation 84
6.5 Absolute Gain 85

7 Detector Characterization 87
7.1 Dark Characterization 87
7.2 X-ray Characterization 88

8 The ePix100a Hybrid Pixel Detector 91
8.1 ePix100a Camera Description 91
8.2 Characterization of the ePix100a Performance 92
8.2.1 Dark Signal Characterization 94
8.2.2 Gain Calibration and Performance under Illumination 97
8.2.3 Signal to Noise Ratio, Dynamic Range and Energy Resolution 102

9 Radiation Damage of the ePix100a Detector 105
9.1 Motivation for the Radiation Damage Studies of the ePix100a 105
9.2 Experiment Setup 106
9.3 Experiment Methodology 107
9.4 Dose Evaluation 110
9.5 Results 115
9.5.1 Immediate Effects 115
9.5.2 Post-Irradiation Performance 116
9.6 Discussion of the Observed Effects 122

9.6.1 Unresponsive Pixels upon Beam Irradiation 122
9.6.2 Offset Surpassing the Dynamic Range of the ADC 122
9.6.3 Gain Changes 126
9.7 Lifetime Estimate of the ePix100a 127

10 Conclusions and Outlook **131**

Zhrnutie **135**

Appendices **139**

A The LPD Detector **141**
A.1 Mapping 141
A.2 Time Evolvement of the Noise 143
A.3 Spatial Distribution of the Noise 144

Bibliography **145**

List of Author's Publications **154**

List of Figures

1.1 Peak brilliance at different energies 28
1.2 Time structure of the EuXFEL 29

2.1 Energy band structure of insulators, semiconductors and conductors . 36
2.2 Conductivity of Si and W as a function of temperature 37
2.3 Diamond lattice structure of silicon 37
2.4 Valence and conduction bands as a function of lattice spacing 38
2.5 Fermi level in relation to doping 40
2.6 Mass attenuation coefficient in silicon as a function of the photon energy 41
2.7 Photoelectric effect 42
2.8 Compton scattering 43
2.9 Probability of the photoelectric effect, Compton scattering and pair production as a function of photon energy 44

3.1 p-n junction band diagram 46
3.2 I-V characteristic of an ideal diode 52
3.3 MOS energy band diagram 53
3.4 Energy band diagrams of MOS operation modes 54
3.5 C-V characteristic of pMOS 59
3.6 C-V characteristic of nMOS 60

4.1 Charges associated with thermally oxidized silicon 63
4.2 Sheet charge effect 64
4.3 MOS C-V characteristics 66
4.4 Processes leading to radiation-induced surface damage 67
4.5 Hole yield as a function of the applied electric field 68
4.6 Model of an oxide trap creation in SiO_2 69
4.7 Threshold voltage shift as a function of time 70
4.8 Dose enhancement effect in the MOS 73

4.9 Dose enhancement as a function of SiO_2 thickness for 10 keV X-rays . 74
4.10 Breakdown voltage as a function of radiation dose 76
4.11 Charge carrier mobility as a function of interface trap density 77

7.1 Detector characterization flowchart 90

8.1 Cross-section of the sensor and the readout scheme of the ePix100a . 93
8.2 Simplified schematic of the ePix100a pixel. 93
8.3 Offset maps of the ePix100a measured at $t_{\mathrm{Int}} = 50\,\mu$s and $t_{\mathrm{Int}} = 800\,\mu$s 94
8.4 Common mode correction effect on the spatial distribution of dark signal 96
8.5 Histograms of the offset subtracted dark signal and noise before and after CM correction 97
8.6 Noise maps of the ePix100a measured at $t_{\mathrm{Int}} = 50\,\mu$s and $t_{\mathrm{Int}} = 800\,\mu$s 98
8.7 Offset and noise histograms 98
8.8 Offset and noise maps of the region of interest 99
8.9 Setup used for calibration measurements of the ePix100a 100
8.10 Cu-K fluorescence spectrum of photons interacting with single pixels . 101
8.11 Relative gain map of the ePix100a 102
8.12 Cu-K fluorescence spectrum before and after relative gain correction . 103
8.13 Gaussian model of the Cu-K line and the calibrated spectrum 103

9.1 Experimental setup used to irradiate the ePix100a with a direct beam 107
9.2 The noise map of the ePix100a showing the irradiated area location on the sensor 108
9.3 Flowchart of the irradiation experiment 110
9.4 Beam profile 111
9.5 Flowchart of the steps to calculate photon intake 112
9.6 Detection of unresponsive pixels and the total photon intake 112
9.7 Per-pixel dose distribution 114
9.8 Area of saturated pixels and dark signal as function of time 115
9.9 Offset and noise changes over days 117
9.10 Ratio of the offset change at 800 μs and 50 μs 117
9.11 Radiation-induced changes of the offset and noise for $t_{\mathrm{Int}} = 800\,\mu$s . . 118
9.12 Radiation-induced changes of the offset and noise for $t_{\mathrm{Int}} = 50\,\mu$s . . . 118
9.13 Offset and noise change as a function of the absorbed dose 119
9.14 Cu-K spectrum before and after irradiation 120

9.15 Position of the Cu-K line as a function of the absorbed dose 121
9.16 Gain as a function of dose 122
9.17 Coordinate system and stencil for FDM 124
9.18 Simulated temperature distribution on the sensor 126
9.19 Schematic visualization of an ePix100a pixel when irradiated with high intensity 127
9.20 Dynamic range reduction as a function of beam energy 128
9.21 Dynamic range reduction as a function of beam time fraction 129
9.22 Reduction of signal-to-noise separation as a function of beam energy . 130
9.23 Reduction of signal-to-noise separation as a function of beam time fraction 130

10.1 Estimates for a gain decrease by 1 ADU/keV 132

A.1 Mapping of the LPD 142
A.2 RMS noise values of the selected LPD tiles collected during one year of operation 143
A.3 Spatial distribution of noise of the LPD 144

List of Tables

1.1 Performance parameters of the 2D detetcors at the EuXFEL 33

8.1 Summary of the performance characteristics of the ePix100a detector. 104

9.1 Summary of the beamline and detector parameters during the irradiation experiment 109

9.2 Dose thresholds estimates 130

List of Acronyms

ADC Analog-to-Digital Converter.

ADU Analog Digital Unit.

AGIPD Adaptive Gain Integrating Pixel Detector.

ASIC Application Specific Integration Circuit.

CCD Charge-Coupled Device.

CDS Correlated Double Sampling.

CM Common Mode.

CPE Charged Particle Equilibrium.

CSA Charge Sensitive Amplifier.

CTE Charge Transfer Efficiency.

CVD Chemical Vapour Deposition.

DE Dose Enhancement.

DR Dynamic Range.

DSSC DEPFET Sensor with Signal Compression.

EM Electromagnetic.

ENC Electronic Noise Charge.

EuXFEL European X-ray Free Electron Laser.

FDM Finite-Difference Method.

FEL Free Electron Laser.

FWHM Full Width at Half Maximum.

FXE Femtosecond X-ray experiments.

HED High Energy Density.

HF High Frequency.

LF Low Frequency.

LPD Large Pixel Detector.

MID Material Imaging and Dynamics.

MIP Minimum Ionizing Particle.

MOS Metal-Oxide-Semiconductor.

RMS Root-Mean Square.

ROI Region of Interest.

SASE Self-Amplified Spontaneous Emission.

SCR Space Charge Region.

SCS Spectroscopy Coherent Scattering.

SFX Serial Femtosecond X-ray crystallography.

SNR Signal-to-Noise Ratio.

SPB Single Particles, Clusters Biomolecules.

SQS Small Quantum Systems.

XGM X-ray Gas Monitor.

Chapter 1

Introduction

The European XFEL, an international research facility located in the metropolitan area of Hamburg, Germany, started user operation in September 2017. As the world's most brilliant X-ray source, it enables scientific research using ultrafast spatially coherent pulses with a peak brilliance up to 5×10^{33} photons/s/mm^2/mrad^2/0.1%BW. The EuXFEL provides the highest brilliance amongst FEL sources and exceeds common synchrotrons by nine orders of magnitude, as is shown in Figure 1.1. The X-ray radiation produced by the EuXFEL is of very high intensity and the short pulse duration in the femtosecond range opens possibilities to observe and investigate scientific phenomena under conditions that were previously not achievable in a laboratory environment [1].

1.1 The European XFEL

X-ray pulses in the energy range of $0.25\,\mathrm{keV} - 25\,\mathrm{keV}$ are produced by electrons accelerated in superconducting cavities up to 17.5 GeV. These highly energetic electrons are further guided through a periodical arrangement of magnets, so-called undulators, where they emit X-ray radiation. Laser-like radiation is produced by a process known as self-amplified-spontaneous emission (SASE). During the SASE process, the longitudinal velocity of accelerated electrons is modulated by means of electron–X-ray radiation interactions, which results in a series of electrons organized into micro-bunches. These emit light synchronously and with the same phase, thus creating coherent laser-like radiation [2].

The constructive interference of the radiation emitted by electron movements inside an undulator gives rise to equidistantly spaced energy levels of the photons based on the undulator settings, so-called harmonics. The first harmonic line is the

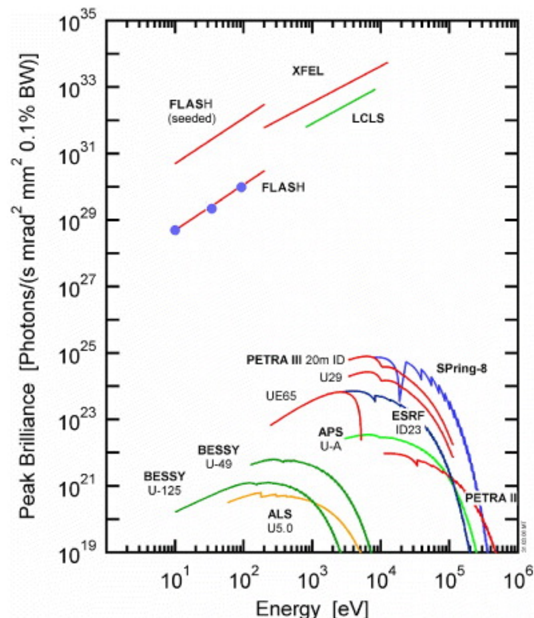

Figure 1.1: Comparison of the peak brilliance in dependency of photon energy between EuXFEL, other FEL facilities (e.g. LCLS, FLASH) and the third generation synchrotron sources [1].

strongest with the highest flux. For the purpose of this thesis, it will be denoted as the fundamental beam energy. Usually, on-axis radiation is of interest. Hence only odd harmonics are present in the generated energy lines [3].

Undulator systems with a length of 175 m and of 105 m are used to produce laser-like radiation with very short wavelengths (from units of nm to hundredths of nm; the hard X-ray regime).

A unique characteristic of EuXFEL is the time structure of the X-ray pulses. As shown in Figure 1.2, X-ray pulses with a duration of less than 100 fs are delivered in so-called trains with a maximum of 2700 pulses per train. The individual trains, lasting 600 μs, are separated by a gap of 99.4 ms resulting in a train repetition rate of 10 Hz. The number of pulses in each train is a variable parameter, adjusted according to an experiment's needs.

The linear accelerator that is used to bring electrons up to an energy of 17.5 GeV can drive several undulator systems at the same time. Each undulator system constitutes a SASE beamline. For each beamline, X-ray radiation with different properties can be generated for the different, simultaneously operating experimental endstations. At the European XFEL, three SASE beamlines are operated, each serving two scientific instruments. Thus six different experimental stations are available to

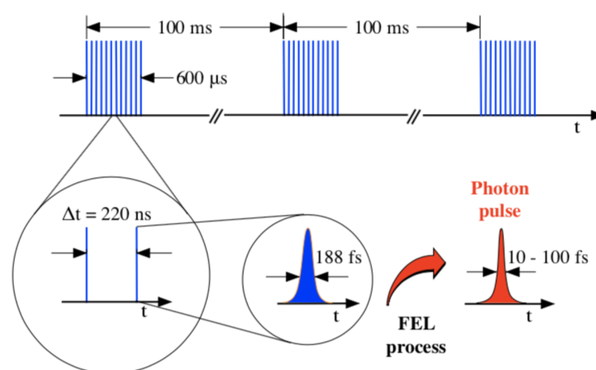

Figure 1.2: Time structure of the European XFEL. Adopted from [4].

users in total. In the following, the three SASE beamlines with their experimental station are introduced.

SASE 1

At *SASE 1* the Single Particles, Clusters, and Biomolecules & Serial Femtosecond Crystallography (*SPB/SFX*) and Femtosecond X-ray experiments (*FXE*) instruments [1] are operated.

- The *SPB/SFX* instrument's primary goal lies in determining the structure of objects at the sub-micron and μm scale, at nm resolution. Emphasis is given to the study of biological samples, such as macromolecules, viruses or cells.
- The *FXE* instrument mainly focuses on time-resolved investigation of the dynamics of the states of matter, i.e. solids, liquids, gases and plasma.

The photon energy used at the *SASE 1* beamline ranges from 3 keV to 20 keV. *SASE 1* started user operation in September 2017.

SASE 2

At *SASE 2* the Materials Imaging and Dynamics (*MID*) and High Energy Density (*HED*) instruments are hosted [1].

- The *MID* instrument determines structure and investigates the dynamics of nanoscale samples, in fields such as condensed matter physics to biology.
- The *HED* instrument investigates matter under extreme conditions, i.e. extreme pressure, temperature or electric field using hard X-ray FEL radiation.

The energy range used in *SASE 2* is from 3 keV to 25 keV. The first lasing at the *SASE 2* beamline was in May 2018 and early user experiments started in the first half of 2019.

SASE 3

At *SASE 3* the Spectroscopy & Coherent Scattering (*SCS*) and Small Quantum Systems (*SQS*) instruments are operated [1].

- Time-resolved studies of electronic and structural properties of nanosystems and of non-reproducible biological objects are performed at the *SCS* instrument.
- Fundamental processes in atoms, ions molecules and clusters in the soft X-ray regime investigation are conducted at the *SQS*.

The *SASE 3* beamline produces soft X-rays in the energy range of 0.25 keV to 3 keV. First user experiments at this beamline started in the last quarter of 2018.

1.2 Imaging Detectors at the EuXFEL

The unique properties of the EuXFEL beam and each beamline's experiments set demanding requirements towards detector performance and capabilities [5]. As there was no existing detector technology capable of satisfying the requirements resulting from the EuXFEL time structure, intensity of the FEL beam and specific needs of scientific instruments, a demand for novel detector systems arose. Each detector system was optimized to fulfil that portion of these requirements most important for the dedicated use-case of the experiment. In the following, I summarize these requirements and provide an overview of the detectors at the EuXFEL, together with their performance and operating parameters.

1.2.1 Detector Requirements

Detectors capable of recording images at 4.5 MHz are needed to match the pulse structure of the EuXFEL. This repetition rate corresponds to imaging individual pulses in a train during a burst frequency of $\frac{2700\text{ pulses}}{600\,\mu\text{s}} = 4.5\,\text{MHz}$. Moreover, the short duration of the pulses (< 100 fs) has to be taken into account. In the scenario of single pulse-per-frame detection, an image needs to be acquired and read out

within the 220 ns gap between two X-ray pulses. As a solution to this problem, on-ASIC[1] memory is used to store images, which can be later read out during the 99.4 ms gap between trains. Ideally, the detectors would have 2700 memory cells available, and thus store the maximum possible number of pulses per train. However, such a high number of memory cells would lead to an increased pixel size, which would consequently reduce the spatial resolution of the detector. Instead, a smaller number of memory cells store only a fraction of frames while maintaining reasonable spatial resolution. A veto system exists to compensate for the smaller memory depth. It rejects images that do not meet pre-specified criteria, storing only good scientific data and preserving the memory for consecutive frames from subsequent pulses [5]. As some of the experiments do not require data acquisition at 4.5 MHz pulse repetition rate, detectors with lower frame rates can be used, e.g. detectors operated at frame rate matching with the train repetition rate of 10 Hz.

Imaging at a repetition rate of 4.5 MHz results in a high data rate of the order of $10 - 12$ GB/s per detector, which requires a complex data management as well as data storage system [6].

The differing energies of the *SASE* beamlines call for optimization of the detector sensitivity to the specific energy range of a beamline. In the case of experiments with soft X-rays, (*SASE 3* beamline) detectors have to provide a low noise level, maximizing the signal-to-noise ratio, in order to retain single-photon sensitivity.

Imaging of 2D scattering experiments requires detectors with a high dynamic range as intensities within the same frame may vary significantly, between 1 ph/pixel and several thousand ph/pixel. These detectors have to resolve single photons then and integrate up to 10^6 ph/pixel/pulse, ideally in each pixel independently.

A highly intense X-ray beam can be a danger, not only to the detector's sensors but also to the co-located detector electronics. At the EuXFEL two concepts are used to avoid contact with the primary beam:

- Segmented detectors have movable parts able to create a pass-through opening for the beam flexibly;
- Detectors have physical hole laser-drilled in the sensor.

However, a pass-through opening is only a protection against instantaneous damage by the primary beam. The long-term operation of detectors under X-ray photon irradiation leads to deposition of dose in the sensor material, which is estimated

[1] ASIC: Application Specific Integrated Circuit

to be up to 1 GGy in three years of normal operation [5]. This estimate excludes accident scenarios, such as the direct beam hitting a detector or unwanted scattering on a detector resulting from a direct beam hitting parts of the experimental setup within the beam path. There is a need to design radiation-hard detector systems to cope with the high radiation dose without changing the detectors performance parameters significantly. Several studies have been made on radiation damage effects [4, 7], from which estimates for the expected radiation damage of the sensor can be made. For a detector irradiated with photons in the keV range, surface radiation damage due to an increase in the number of traps at Si–SiO_2 interfaces is expected, having the following consequences on the detector:

- increase of a leakage current,
- breakdown voltage reduction,
- increase of the depletion voltage,
- increase of the interpixel capacitance.

Even though sensors for EuXFEL detectors were designed to be radiation hard, considering the constraints and expectations based on detailed radiation-damage studies, a real-time performance study will help evaluate the actual changes in detector performance. Such a study of radiation-induced damage effects can give an estimate of a detector's lifetime based on two concepts:

1. The detector parameters have changed to a level that the performance of a detector not longer meets its scientific requirements;
2. The detector received such a high dose that sensors/electronics became dysfunctional.

Several detectors were explicitly developed for the needs of the European XFEL considering the requirements for detector performance stated earlier, i.e. the Adaptive Gain Integrating Pixel Detector (AGIPD), the DEPFET Sensor with Signal Compression (DSSC) and the Large Pixel Detector (LPD). Other detector technologies primarily developed for other FEL facilities were adapted for such use at the EuXFEL. A summary of 2D detectors in use at the European XFEL is listed in Table 1.1, providing also reference for each detector.

Table 1.1: Performance parameters of the 2D imaging pixel detectors in use at the European XFEL.

2D Detector	Pixel Size (μm^2)	Energy Range (keV)	Dynamic Range	EuXFEL Frame Rate	Maximum Frame Rate	Instrument
AGIPD [8]	200 × 200	3 – 16	10^4 ph @ 12 keV	4.5 MHz	4.5 MHz	SPB, MID
DSSC DEPFET [9]	204 × 236*	0.5 – 6	6×10^3 ph @ 1 keV	4.5 MHz	4.5 MHz	SCS, SQS
DSSC mini-SDD [10]	204 × 236*	0.5 – 6	10^2 ph @ 1 keV	4.5 MHz	4.5 MHz	SCS, SQS
ePix100a [11, 12]	50 × 50	2 – 18	10^2 ph @ 8 keV	10 Hz	240 Hz	HED, MID
FastCCD [13, 14]	30 × 30	0.25 – 6	10^3 ph @ 0.5 keV	10 Hz	120 Hz	SCS
JUNGFRAU [15]	75 × 75	3 – 25	10^4 ph @ 12 keV	10 Hz	1.1 kHz	HED
LPD [16]	500 × 500	5 – 20	10^5 ph @ 12 keV	4.5 MHz	4.5 MHz	FXE
pnCCD [17]	75 × 75	0.03 – 25	6×10^3 ph @ 1 keV	10 Hz	150 Hz	SCS, SQS

* Hexagonal pixels.

Chapter 2

Silicon as Semiconductor Material

Silicon is a semiconducting chemical element abundant in the natural environment, composing 27 % of Earth's crust and is the most commonly used material in the semiconductor industry. It occurs mainly in the form of various silicon compounds and very rarely in its pure form. In this chapter, silicon as a detector material will be discussed.

2.1 Introduction to Semiconductors

Silicon is the most commonly used semiconductor material. Materials can be classified into three categories according to their electrical conductivity: conductors, insulators or semiconductors. Electrons in an isolated atom have only discrete energies and occupy specific energy levels based on these energies. The allowed energy levels for a given quantum number (e.g. $\mathrm{n} = 1$) consist of one doubly degenerate level. For a periodically arranged crystal lattice, N atoms are present. In case the atom-to-atom separation is many times larger than the usual lattice constant, discrete energy levels of a single atom are justified. However, by reducing the atom-to-atom separation to form a crystal, the atoms start interacting. The doubly degenerate energy levels will split into two levels due to the interaction between the atoms. This interaction causes a shift in energy levels. N levels which are closely spaced are formed. When N is large, the result is a continuous energy band. The highest occupied energy band is known as the valence band, defined by the highest energy level of its electrons E_v. The conduction band is the lowest unoccupied band, characterized by free electrons, which after excitation from the valence band contribute to the material's conductivity. The conduction band is defined by the lowest electron energy in the conduction band, E_c. A region of forbidden energy states,

defined by the energy difference between the valence and the conduction band, is the so-called band gap E_g. The energy of the band gap E_g is an indicator for the electrical conductivity of material: In the case of an insulator, the band gap is so large ($E_g > 5\,eV$) that the probability of an electron to gain enough energy to move to the conduction band is close to zero, as can be seen in Figure 2.1a. If a material's valence band and conduction band overlap or the conduction band is partially filled with electrons, the material is classified as a conductor (Fig. 2.1d, e). In the case of a conductor, the band gap is zero. The band gap energy of semiconductors is low enough to create conductivity by absorption of thermal energy. The conduction band of semiconductors is entirely empty at 0 K and consequently, they behave like insulators. On the other hand, the absorption of thermal energy by a semiconductor can cause electrons to be excited from the valence to the conduction band, resulting in an increase of the semiconductor conductivity due to free electrons. The vacancies created in the valence band by these electrons are called holes, which can be seen as equivalent to a positive charge. Increase of the temperature increases the number of electrons with sufficient kinetic energy to overcome the band gap and to be excited into the conduction band. Therefore, the electrical conductivity of a semiconductor increases rapidly with increasing temperature, in contrast to the behaviour of a metal crystal, as the higher the temperature is, the higher the number of electrons excited to the conduction band is. Figure 2.2 illustrates the difference between the temperature dependence of semiconductors' and metals' conductivity.

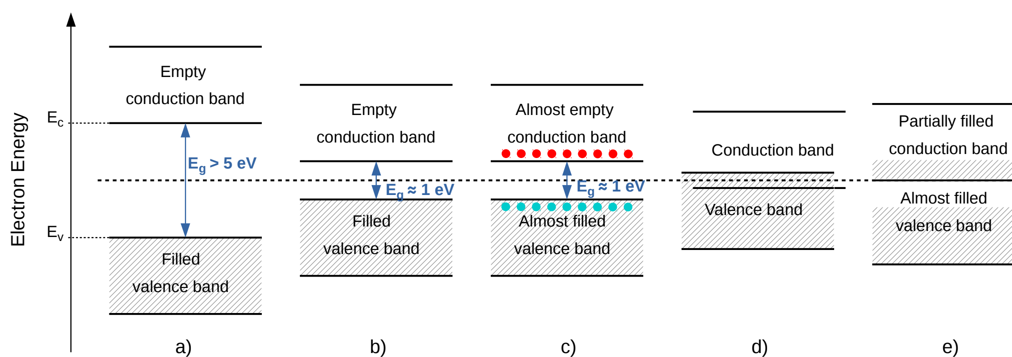

Figure 2.1: Energy band structure of insulators (a), semiconductors at $T = 0\,K$ (b), semiconductors at $T > 0\,K$ (c) and conductors (d,e).

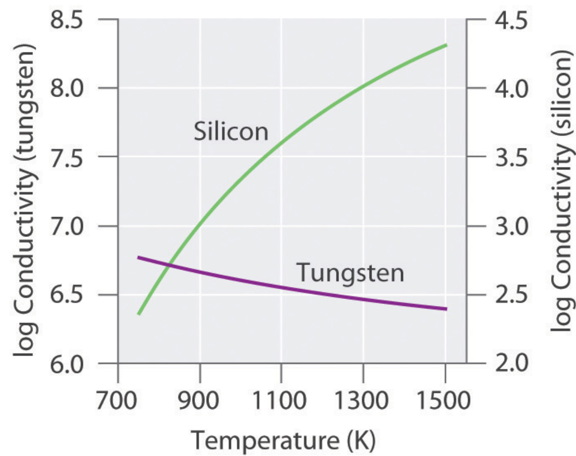

Figure 2.2: Dependency of conductivity of the semiconductor Si and the metal W on temperature [18].

2.1.1 Intrinsic Silicon

Silicon is a material of the IVth group of periodic table with atomic number 14. Its outer atomic orbital consists of four covalently bonded electrons. The silicon crystalline structure corresponds to a diamond lattice with a structure of two interpenetrating face-centered cubic (fcc) primitive lattices as shown in Figure 2.3. The lattice constant a is 5.431 Å.

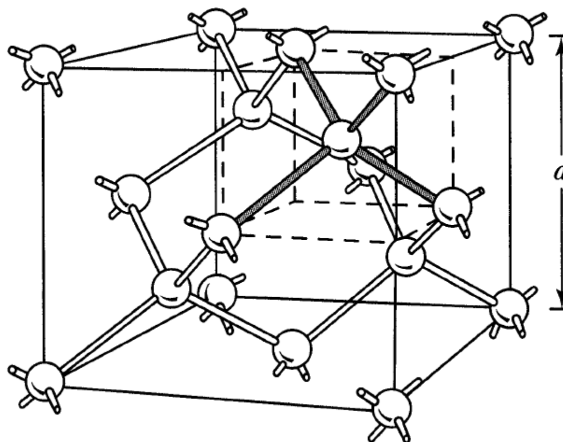

Figure 2.3: Diamond lattice structure of silicon. The parameter a represents the lattice constant of silicon [19].

Figure 2.4 shows a diagram of the silicon energy band structure in relation to the lattice constant. With decreasing interatomic distance, silicon atoms start to interact and overlap, their energy levels split to N closely spaced levels, and with N $\rightarrow$

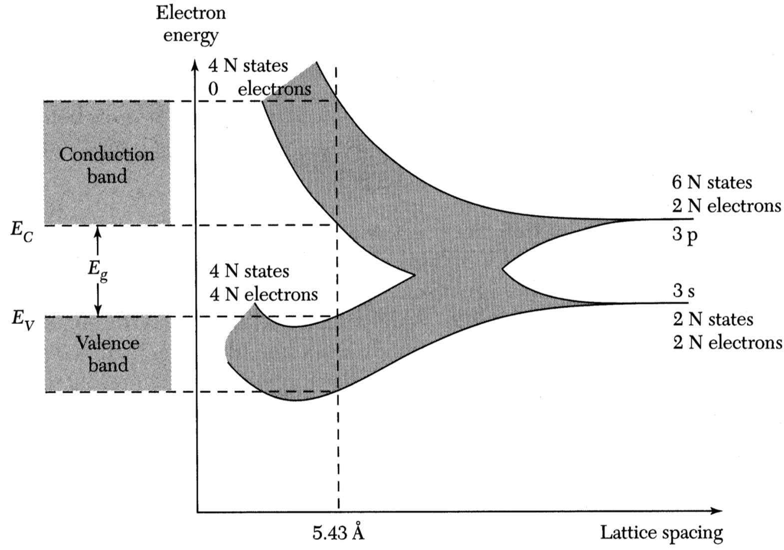

Figure 2.4: Schematic structure of the valence and conduction bands as a function of lattice spacing [19].

∞, these levels merge into the energy bands. Silicon is an indirect semiconductor, which means that the maximum energy of the valence band and the minimum energy of the conduction band occur at different values of crystal momentum. Consequently, the creation of an electron-hole pair by indirect transition has to be accompanied by a momentum change. This is achieved by an electron interaction with a phonon, the energy quantum of lattice vibration.

The probability of an electron occupying a certain energy level E of an atom is described by the Fermi-Dirac distribution function given as

$$f(E) = \frac{1}{1 + \exp(\frac{E-E_F}{k_B T})}, \tag{2.1}$$

where k_B is Boltzman constant, T the temperature and E_F represents the Fermi level. The Fermi level is a hypothetical energy level of an electron at which the state occupation probability in thermal equilibrium is one half. Using equation 2.1, the concentration of free charge carriers can be evaluated. The concentration of free electrons in the conduction band n at energy level E_c, with effective density of states N_c, is given as

$$n = N_c \exp(-\frac{E_c - E_F}{k_B T}), \tag{2.2}$$

while the concentration of free holes in the valence band p at energy E_v, with effective density of states N_v, is given as

$$p = N_v \exp(-\frac{E_F - E_v}{k_B T}). \tag{2.3}$$

For intrinsic silicon under thermal equilibrium conditions, the concentrations of electrons and holes are the same, hence (according to the mass action law)

$$\begin{aligned} n_i &= n = p, \\ n_i &= \sqrt{np} = \sqrt{N_c N_v} \exp(-\frac{E_g}{2k_B T}), \end{aligned} \tag{2.4}$$

where n_i represents the intrinsic concentration of charge carriers. At room temperature the formula given in [20] results in $n_i(300\,K) = 9.68 \times 10^9\,cm^{-3}$. The band gap energy of silicon is $E_g(300\,K) = 1.12\,\mathrm{eV}$ [21] and the average energy needed to create an electron-hole pair is $\langle E_{pair} \rangle \approx 3.6\,\mathrm{eV}$ [21].

Using the neutrality condition from equation 2.4 and rearranging yields

$$\frac{N_v}{N_c} = \exp(\frac{2E_F - E_c - E_v}{k_B T}), \tag{2.5}$$

resulting in

$$E_F = \frac{E_c + E_v}{2} + \frac{k_B T}{2} \ln \frac{N_v}{N_c} = E_i, \tag{2.6}$$

where E_i is the intrinsic energy of the Fermi level of an intrinsic semiconductor, which is located in the center between the valence and the conduction band. The deviation of the energy level from the center is due to the difference between the effective masses of electrons and holes.

2.1.2 Extrinsic Silicon

Most applications require higher conductivity than intrinsic silicon has. By introducing impurity elements, so-called dopants, the concentration of charge carriers can be altered. As silicon has four valence electrons, dopant elements from group III or V are used to incorporate additional energy levels in the band gap. If the dopant is of the IIIth element group (acceptor), one electron is trapped to create a bond between the silicon and the dopant. As a result, the concentration of electrons decreases (minority charge carriers), and hole conductivity is dominant (majority charge carriers). The resulting material is a so-called p-type semiconductor. In the case of a dopant with one more valence electron than silicon (V group element),

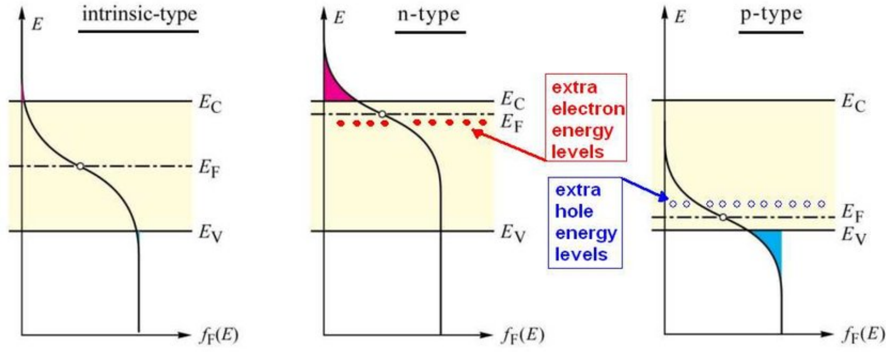

Figure 2.5: Impact of doping on the Fermi energy. Shift of the Fermi level closer to the conduction band, in case of n-type (donor doping) and close to the valence band for the p-type (acceptor doping) semiconductor [22].

this additional electron cannot form an electron pair. It is left unbound, thus increasing the conductivity of the silicon. As the electron concentration exceeds the hole concentration, the resulting semiconductor is of n-type with electrons as majority charge carriers. Dopants with excess numbers of electrons are so-called donors. This doping of silicon results in a shift in the Fermi level, as shown in Figure 2.5. The Fermi level for a donor concentration N_D with completely ionized donors and electron density $n = N_D$ is then given by

$$E_c - E_F = k_B T \ln \frac{N_c}{N_D}. \tag{2.7}$$

Likewise for an acceptor concentration N_A and hole density $p = N_A$, the Fermi level changes to

$$E_F - E_v = k_B T \ln \frac{N_v}{N_A}. \tag{2.8}$$

The carrier concentration can be expressed in terms of the Fermi level energy as

$$n = n_i \exp(\frac{E_F - E_i}{k_B T}), \tag{2.9a}$$

$$p = n_i \exp(\frac{E_i - E_F}{k_B T}). \tag{2.9b}$$

In a non-equilibrium case, where no constant Fermi level exists, a quasi-Fermi level has to be defined for electrons E_{F_n} and holes E_{F_p}, resulting in

$$n = n_i \exp(\frac{E_{F_n} - E_i}{k_B T}), \tag{2.10a}$$

$$p = n_i \exp(\frac{E_i - E_{F_p}}{k_B T}). \tag{2.10b}$$

2.2 Interaction of X-rays with Silicon

Electromagnetic radiation interacts with semiconductors mainly by the photoelectric effect, Compton scattering, Rayleigh scattering and electron-positron pair production. Figure 2.6 and Figure 2.9 illustrate the significance of these effects based on the incident X-ray energy. The most relevant effect for the EuXFEL energy range is the photoelectric effect and, to a lesser extent, coherent Rayleigh scattering and incoherent Compton scattering. Hence these are discussed in the following section.

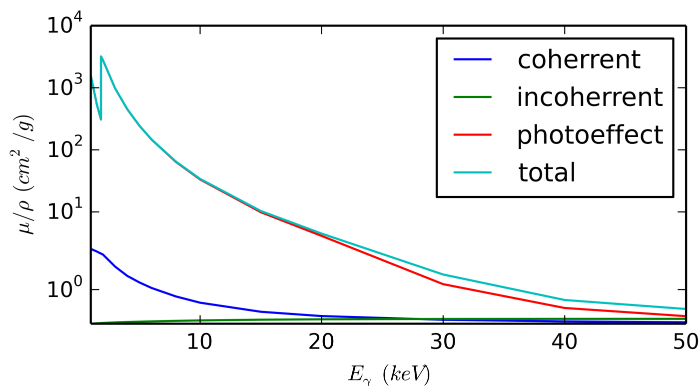

Figure 2.6: Mass attenuation coefficient in silicon as a function of the photon energy in the range of $(1-50)\,\text{keV}$ with contributing sources of attenuation: coherent scattering (blue), incoherent scattering (green) and photoelectric effect (red). Data from [23].

The photoelectric effect

The photoelectric effect is an interaction between a photon and an electron tightly bound to an atom. During the interaction, the photon is completely absorbed, and a photo-electron is released. The release occurs when the photon energy E_{ph} exceeds the binding energy of the electron to atom E_b. The kinetic energy of the photo-electron (E_k) is equal to the incident photon energy reduced by the binding energy of the photo-electron in its original shell:

$$E_k = E_{ph} - E_b. \tag{2.11}$$

Moreover, the release of a photo-electron creates a vacancy filled by an electron from a shell with lower binding energy and a characteristic X-ray, or Auger electron is emitted as shown in Figure 2.7.

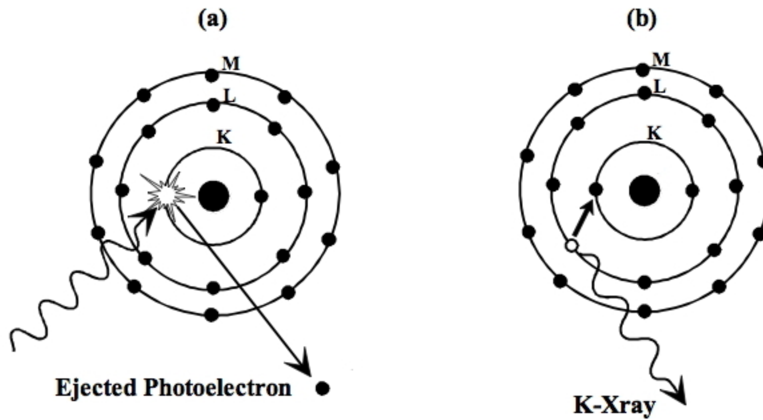

Figure 2.7: Schematic visualization of the photoelectric effect. Left plot shows ionisation of the electron and the right one demonstrates the filling up of the vacancy and production of the characteristic X-ray. Figure adopted from [24].

If the incident photon energy is higher than the binding energy E_b and the predominant interaction mechanism for low energy radiation is the photoelectric effect. The cross-section of the photoelectric absorption per unit mass is approximately proportional to:

$$\tau_{photoelectric} \propto \frac{Z^n}{E_{ph}^{3.5}} \approx Z^5 E_{ph}^{-3.5}, \tag{2.12}$$

where Z is the material atomic number. The exponent n varies between 4 and 5 and E_{ph} is the incident photon energy [25]. The cross-section exhibits characteristic absorption edges when the energy of the absorbed photon coincides with the ionization energies of electrons for certain atomic shells.

Compton scattering

Figure 2.8 illustrates the Compton effect. It is the scattering of an incident photon on an individual atomic electron. When the photon transfers part of its energy to the electron, it is deflected by an angle θ with respect to its original direction. The photon deflection causes a decrease of the photon energy, and its change is given by the Compton wavelength shift formula

$$\Delta\lambda = \lambda' - \lambda = \lambda_c\,(1 - \cos\theta)\,,$$
$$\text{and } \lambda_c = \frac{h}{m_e c}, \tag{2.13}$$

where λ and λ' are the initial photon wavelength, respectively the photon wavelength after the scattering, $\Delta\lambda$ is the Compton shift wavelength of the incident photon, λ_c is the Compton wavelength of the recoil electron and amounts to 2.4×10^{-12} m and θ is the scattering angle of the photon. The energy of the scattered photon E'_{ph} for a given incident photon energy $E_{ph} = \frac{hc}{\lambda}$ is

$$E'_{ph} = \frac{E_{ph}}{1 + (E_{ph}/m_e c^2)\,(1 - \cos\theta.)}. \tag{2.14}$$

The Compton scattering cross-section is given by the Klein-Nishina formula [26], which assumes that the scattering is elastic. This is a good approximation if the photon energies are higher than 1 MeV [27, 28]. When the photon energies are lower (e.g. EuXFEL energy range), the electron binding energy must be considered, and Compton scattering becomes inelastic.

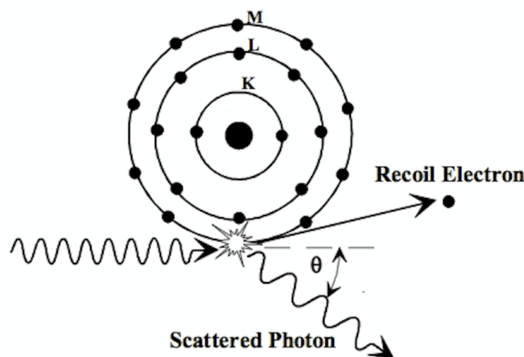

Figure 2.8: Schematic vizualization of Compton scattering. The incident photon is scattered on an atomic electron and a recoil electron is released. Figure adopted from [24].

Rayleigh scattering

Rayleigh scattering is an elastic process of the scattering of photons by atom-bound electrons, leaving the atom neither excited nor ionized. The recoil energy of the atom after absorbing the photon transferred momentum is small, and the scattered photon has essentially the same energy as the original photon. Therefore, Rayleigh

scattering does not contribute to photon absorption. It does, however, have an impact on the direction of the scattered photon.

The probabilities of the photoelectric effect, Compton scattering and the electron-positron pair creation as a function of the photon energy and the atomic number of the target material are shown in Figure 2.9.

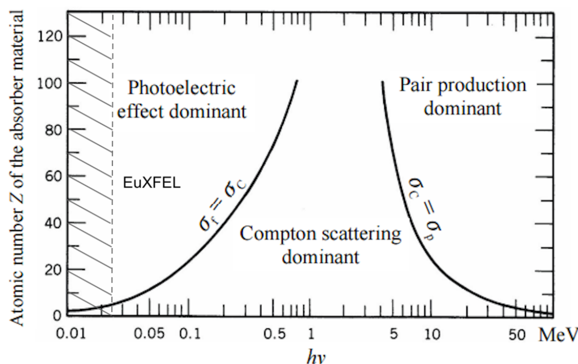

Figure 2.9: The probability of the photoelectric effect, Compton scattering and pair production as a function of a photon energy and atomic number of the material. The hatched area visualizes the energy range of the EuXFEL. Figure adopted from [29].

Attenuation of X-rays by Matter

When X-ray radiation traverses matter, individual photons are absorbed or scattered by the mechanisms described earlier, thus attenuating the intensity of the X-ray radiation. The radiation intensity $I(x)$ after passing a distance x in the material is given by the Lambert-Beer law as

$$I(x) = I_0 e^{-\mu x}, \tag{2.15}$$

where I_0 is the initial intensity and μ is the linear attenuation coefficient. The linear attenuation coefficient expresses the extent of the radiation intensity reduction by traversing the material. It can be interpreted as the average distance travelled by the photon inside the material before an interaction occurs. The coefficient depends on the material as well as on the energy of the radiation. It is often expressed as a mass attenuation coefficient, which is the attenuation coefficient divided by the mass density, i.e. $\mu_m = \frac{\mu}{\rho}$. The mass attenuation coefficient of silicon as a function of the photon energy is shown in Figure 2.6, also visualizing the contribution of individual processes.

Chapter 3

Basic Semiconductor Devices

The following section presents the basic structures used in semiconductor detectors. Knowledge about the properties of these devices is necessary in order to understand the operational principle of semiconductor detectors.

The detection of photons or charged particles by semiconductor detectors is based on electron-hole pair creation, induced by the interaction of ionizing radiation with the detector material. Electrons and holes are separated by an electric field and drift to the electrodes, where the resulting signal is measured. To have a good detector system, large signal amplification and low noise are typically two essential requirements. In order to satisfy the requirement of large signal amplification, radiation should produce many electron-hole pairs, which requires low ionization energy and hence a small band gap. Having a small band gap is in contradiction with the low noise requirement as a smaller band gap implies a higher number of thermally generated charge carriers. If not compensated, the signal from thermally generated electron-hole pairs would be several orders of magnitude higher than the signal generated by photons or charged particles. A depleted region (where the density of free charge carriers is so low that signals in the order of 10^3 electron-hole pairs can be detected) needs to be created to solve this problem. A depletion region suitable for detection is created by using a reversed biased *p*-*n* junction. In the following, its basic characteristics will be discussed.

3.1 The p-n Junction

The *p*-*n* junction is formed by creating a connection between a *p*-type and an *n*-type semiconductor. Consider two homogeneously doped regions: the *p* region with doping concentrations $p_p = N_A$ and $n_p = \frac{n_i^2}{N_A}$ and the *n* region with doping concen-

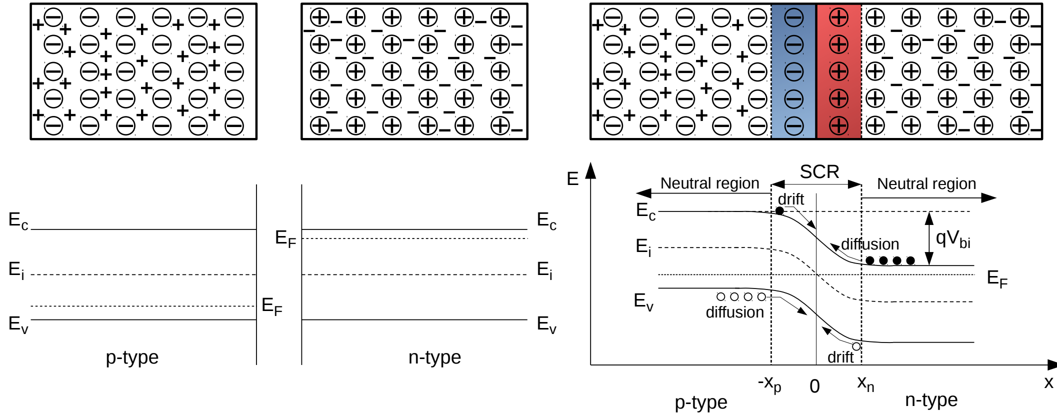

Figure 3.1: Schematic drawing of a p-n junction in thermal equilibrium. Band diagram of separated *p*-type and *n*-type semiconductor (left), formation of *p*-*n* junction (right).

trations $n_n = N_D$ and $p_n = \frac{n_i^2}{N_D}$ are initially separated and in thermal equilibrium (Figure 3.1, left). When the two regions are brought into contact, electrons from the n region will diffuse into the p region and holes from the p region into the n region. As a result, surplus negative charges in the p region and positive charges in the n region are created. Electrons and holes at the boundary will recombine, and a depleted region is created, where the free charge carrier density is strongly reduced (Figure 3.1, right). The diffusion of electrons creates a static space charge of positively charged donor ions in the n region.

Similarly, the space charge of negatively charged acceptor ions is created in the p region. The static charges create an electric field, which creates a drift current in the opposite direction of the diffusion current. The equilibrium state of the p-n junction is reached when the drift and the diffusion current are equal. The electrostatic potential present at the p-n junction interface, known as the built-in voltage, prevents further charge diffusion. The built-in voltage V_{bi} is given as the difference in the intrinsic levels on the neutral p and n regions. Using equation 2.9 and setting acceptor and donor concentrations equal, this gives

$$V_{bi} = \frac{1}{q}(E_i^p - E_i^n) = \frac{k_B T}{q} \ln(\frac{N_A N_D}{n_i^2}). \tag{3.1}$$

Poisson's equation (1D scenario) has to be solved to estimate the width of the depleted region W. Using the abrupt change approximation (abrupt change between neutral and completely depleted space charge region (SCR)), one gets

$$\frac{\partial^2 \phi}{\partial x^2} = \frac{\rho}{\epsilon_r \epsilon_0} = \begin{cases} 0 & x \leq -x_p \text{ and } x \geq x_n, \\ -q\frac{N_D}{\epsilon_{Si}\epsilon_0} & 0 \leq x \leq x_n, \\ q\frac{N_A}{\epsilon_{Si}\epsilon_0} & -x_p \leq x \leq 0. \end{cases} \tag{3.2}$$

Requiring, that the electrical field at the boundaries of the space charge region is zero and that the built-in voltage is equal to the potential difference, i.e. $V_{bi} = \phi(x_n) - \phi(-x_p)$, together with the charge neutrality condition $N_D x_n = N_A x_p$, the integration of equation 3.2 yields

$$W = x_n + x_p = \sqrt{\frac{2\epsilon_{Si}\epsilon_0}{q}\frac{N_A + N_D}{N_A N_D}V_{bi}}. \tag{3.3}$$

In the case of practical detectors, one side is usually doped very asymmetrically, where $N_A \gg N_D$, resulting in a smaller width of the depletion layer of the p region, hence the expression for W in eq. 3.3 can be simplified to

$$W = \sqrt{\frac{2\epsilon_{Si}\epsilon_0}{q}\frac{V_{bi}}{N_D}}. \tag{3.4}$$

If the p-n junction is forward biased, the externally applied voltage will decrease the potential barrier by the value of the applied voltage V to $V_{bi} - V$. The width of the depletion region reduces to

$$W = \sqrt{\frac{2\epsilon_{Si}\epsilon_0}{q}\frac{1}{N_D}(V_{bi} - V)}, \tag{3.5}$$

and the charge transfer across the junction is increased. On the other hand, when connecting a p-n junction with reverse bias, where positive voltage is applied to the n-side of the junction, the potential barrier is increased by the value of V yielding $V_{bi} + V$. For the width of space charge region, this gives

$$W = \sqrt{\frac{2\epsilon_{Si}\epsilon_0}{q}\frac{1}{N_D}(V_{bi} + V)}. \tag{3.6}$$

The reverse bias acts as a supporting built-in potential, suppressing the diffusion current across the junction. A reverse bias causes the width of the depletion region to increase as the majority carriers are attracted towards the external potential. The drift-driven current flowing through the space charge region is the so-called leakage current and is typically several orders of magnitude smaller than the forward diffusion current.

Using equation 2.9 the carrier concentration at an arbitrary position within the junction can be expressed by the potential or the intrinsic energy level E_i at that position as

$$n_n(x) = n_i \exp\left(\frac{E_F - E_i}{k_B T}\right) \exp\left(\frac{q\phi_{(x)}}{k_B T}\right). \tag{3.7}$$

Since $n_n(x) = n_{n_0} = N_D$ and the potential in the neutral n-type region is ϕ_n, we can write

$$n_{n_0} = n_n(x) = n_i \exp\frac{E_F - E_i^n}{k_B T}, \tag{3.8}$$

where n_{n_0} is the equilibrium electron concentration in the n region, n_n and $E_i^n = E_i + q\phi_n$ (p_p and E_i^p) are the electron (hole) concentration and intrinsic energy level in the neutral n region (p region). Combining the two latter equations, for the region $x_n \leq x \leq \infty$ this yields

$$n_n(x) = n_{n_0} \exp\frac{q(\phi_{(x)} - \phi_n)}{k_B T}, \tag{3.9}$$

Assuming the charge carrier concentration to be n_p (electrons) and p_p (holes) in the p-region and n_n and p_n in the n-region, minority charge carrier concentration at the edges of the depletion region can be defined as

$$n_p(-x_p) = n_{n_0} \exp\frac{q(\phi_p - \phi_n)}{k_B T}. \tag{3.10}$$

Since $\phi_p - \phi_n = V - V_{bi}$, where V is the applied voltage, we get

$$n_p(-x_p) = n_{n_0} \exp\left(\frac{-qV_{bi}}{k_B T}\right) \exp\left(\frac{qV}{k_B T}\right). \tag{3.11}$$

The equilibrium potential (built-in voltage) defined by equation 3.1 can be rewritten as

$$V_{bi} = \frac{k_B T}{q} ln\left(\frac{p_{p_0} n_{n_0}}{n_i^2}\right). \tag{3.12}$$

Combining equation 3.11 and equation 3.12 and knowing that $n_{p_0} = \frac{n_i^2}{p_{p_0}}$ we obtain

$$n_p(-x_p) = n_{p_0} \exp\frac{qV}{k_B T}. \tag{3.13}$$

Similarly, for the holes at the boundary of the neutral n region, we would get,

$$p_n(x_n) = p_{n_0} \exp\frac{qV}{k_B T}. \tag{3.14}$$

In the neutral regions of the junction a current flows due to diffusion, i.e the current density in the neutral n region equals

$$J_p = -qD_p \frac{d_p}{d_x}, \tag{3.15}$$

and current density in the neutral p region is

$$J_n = qDn \frac{d_n}{d_x}. \tag{3.16}$$

The continuity equation for holes in the n-type region is

$$\frac{\partial p_n}{\partial t} = D_p \frac{\partial^2 p_n}{\partial x^2} - \frac{p_n - p_{n_0}}{\tau_p}, \tag{3.17}$$

where D_p is the diffusion coefficient of holes, τ_p is the hole lifetime and $L_p = \sqrt{D_p \tau_p}$ is the diffusion length of holes. Assuming a stationary situation ($\frac{\partial p}{\partial t} = 0$), we get

$$D_p \frac{\partial^2 p_n}{\partial x^2} = \frac{p_n - p_{n_0}}{\tau_p}. \tag{3.18}$$

The solution of the above differential equation can be given as

$$p_n(x) = p_{n_0} + A \exp \frac{-x}{L_p} + B \exp \frac{x}{L_p}. \tag{3.19}$$

Using equation 3.14 and $p_n(\infty) = p_{n_0}$ as boundary conditions for equation 3.19 this yields:

$$\begin{aligned}
p_n(\infty) &= p_{n_0} \Rightarrow B = 0, \\
p_n(x_n) &= p_{n_0} \exp \frac{qV}{k_B T} = p_{n_0} + A \exp \frac{-x_n}{L_p}, \\
A &= p_{n_0} \left[\exp\left(\frac{qV}{k_B T}\right) - 1 \right] \exp \frac{x_n}{L_p}, \\
&\Downarrow \\
p_n(x) &= p_{n_0} + p_{n_0} \left[\exp\left(\frac{qV}{k_B T}\right) - 1 \right] \exp \frac{-(x - x_n)}{L_p}.
\end{aligned} \tag{3.20}$$

Therefore, the hole diffusion current in the neutral n region is

$$J_p = \frac{qD_p p_{n_0}}{L_p} \exp \frac{-(x - x_n)}{L_p} \left[\exp\left(\frac{qV}{k_B T}\right) - 1 \right]. \tag{3.21}$$

Using a similar calculation for the diffusion current in the neutral p region, results in

$$J_n = \frac{qD_n n_{p_0}}{L_n} \exp\frac{(x+x_p)}{L_n}\left[\exp\left(\frac{qV}{k_BT}\right)-1\right]. \tag{3.22}$$

The current density in the device is given by

$$J = constant = J_n(x) + J_p(x). \tag{3.23}$$

Assuming no generation/recombination of charge in the transition zone yields

$$\begin{aligned} J_p(-x_p) &= J_p(x_n), \\ J_n(-x_p) &= J_n(x_n). \end{aligned} \tag{3.24}$$

Therefore, the total current in the depletion region can be expressed as

$$\begin{aligned} J &= J_n(-x_p) + J_p(x_n) = \left[\frac{qD_n n_{p_0}}{L_n} + \frac{qD_p p_{n_0}}{L_p}\right]\left[\exp\left(\frac{qV}{k_BT}\right)-1\right], \\ J &= J_S\left[\exp\left(\frac{qV}{k_BT}\right)-1\right], \end{aligned} \tag{3.25}$$

where J_S is known as the saturation current density and is equal to

$$\begin{aligned} J_S &= q\left(\frac{n_{p_0}D_n}{L_n} + \frac{p_{n_0}D_p}{L_p}\right), \\ &= qn_i^2\left(\frac{1}{N_A}\sqrt{\frac{D_n}{\tau_n}} + \frac{1}{N_D}\sqrt{\frac{D_p}{\tau_p}}\right). \end{aligned} \tag{3.26}$$

Equation 3.25 is known as the Shockley equation. It is to note that the above equations are only simplifications, as no charge generation and recombination in the depletion region were taken into account.

As previously mentioned, if the *p*-*n* junction is reverse biased, a small current flows through the depletion region; the leakage current J_L. The leakage current has two contributions, the generation current J_G and the diffusion saturation current J_S, i.e.

$$J_L = J_G + J_S. \tag{3.27}$$

The generation current is given as

$$J_G = -qGW(V), \tag{3.28}$$

where G is the generation rate in the depletion region given by $G = \frac{n_i}{\tau_g}$, under the assumption that $n \cdot p \ll n_i^2$ and with τ_g as generation lifetime. The minus sign

follows from the convention that currents in a forward-biased diode are taken as positive (n-type part connected to the negative terminal and p-type part connected to the positive terminal). As given in equation 3.6, the width of the depletion region depends on the applied voltage, which will also affect the generation current. The additional current generated in the depletion region by the applied voltage can be estimated from the change in the depletion volume as

$$\begin{aligned} J_G &= -q\frac{n_i}{\tau_g}(W - W_0), \\ &= -q\frac{n_i}{\tau_g}\sqrt{\frac{2\epsilon_{Si}\epsilon_0(N_A + N_D)}{qN_AN_D}}(\sqrt{V_{bi} - V} - \sqrt{V_{bi}}). \end{aligned} \tag{3.29}$$

For asymmetrically doped regions, the diffusion term of the highly doped region can be neglected. In the case of a p^+-n junction, the diffusion of the n region will dominate due to the higher concentration of minority charge carriers, diffusing through the depletion region towards the p^+ region. For such a case, the leakage current is given as

$$J_L = q(\frac{n_iW}{\tau_g} + \frac{n_i^2}{N_D}\sqrt{\frac{D_p}{\tau_p}}). \tag{3.30}$$

The above equation shows that if the width of the depletion region is small (forward bias), and the generation lifetime τ_g is long, diffusion will dominate. On the other hand, for a large depletion width (reverse bias) and short τ_g, the generation current dominates. Additionally, if high currents flow through the junction, the voltage drop from the series resistance $R_S \cdot I$ has to be taken into account yielding

$$I = I_S \exp(q\frac{V - R_S \cdot I}{\eta k_B T}). \tag{3.31}$$

Here the additional η factor is the so-called ideality factor and varies between one and two, depending on the recombination process in the diode. In the case of the ideal diode $\eta = 1$. Figure 3.2 shows the current-voltage characteristic of an ideal diode calculated with equation 3.31 neglecting the series resistance voltage drop and with $\eta = 1$.

3.2 Metal-Oxide-Semiconductor Structure

Next to the p-n junction, the metal-oxide-semiconductor (MOS) structure properties and characteristics have to be understood to gain essential knowledge about

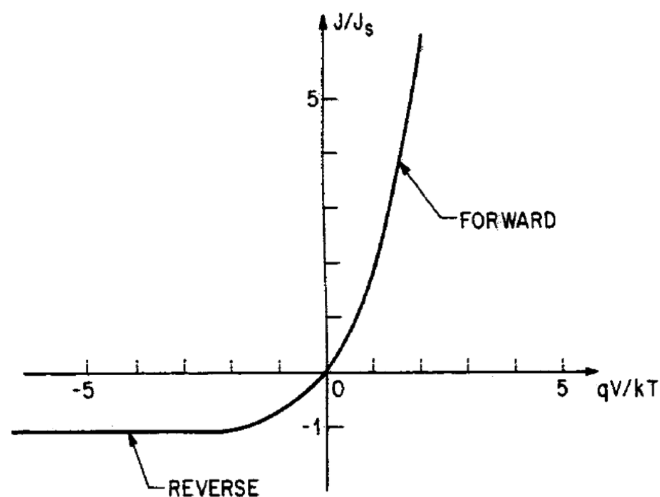

Figure 3.2: Current-voltage characteristic of an ideal diode as a result of the equation 3.31 (adopted from [19]).

semiconductor detectors. The MOS capacitors are the standard structures of the detectors used at the EuXFEL. Knowledge of the MOS structure will be essential for understanding radiation damage expected from X-ray radiation of EuXFEL. The MOS structure is a semiconductor with an additional insulator layer. This is usually an oxide of the substrate used; in the case of silicon, this is silicon dioxide (SiO_2). On top of the SiO_2, a layer of metal or polycrystalline silicon is deposited, creating an electrode known as a gate. The metal and semiconductor that are separated by an insulator can be viewed as a planar capacitor. The left panel in Figure 3.3 schematically shows such a MOS structure. In the following, a detailed discussion of the MOS capacitor operation will be given.

3.2.1 Operation modes

Flat-Band Condition

Suppose the charge carrier concentration in the homogeneously doped n-type semiconductor is uniform and the electric field through the semiconductor is zero. In that case, the so-called flat-band condition is used to describe the situation. A plot of the flat band diagram is shown in Figure 3.3 on the right. The energy difference $q\phi_B$ between E_F and E_i defining the Fermi level is calculated as

$$q\phi_{B_n} = E_F - E_i = k_B T \ln \frac{N_D}{n_i}, \tag{3.32a}$$

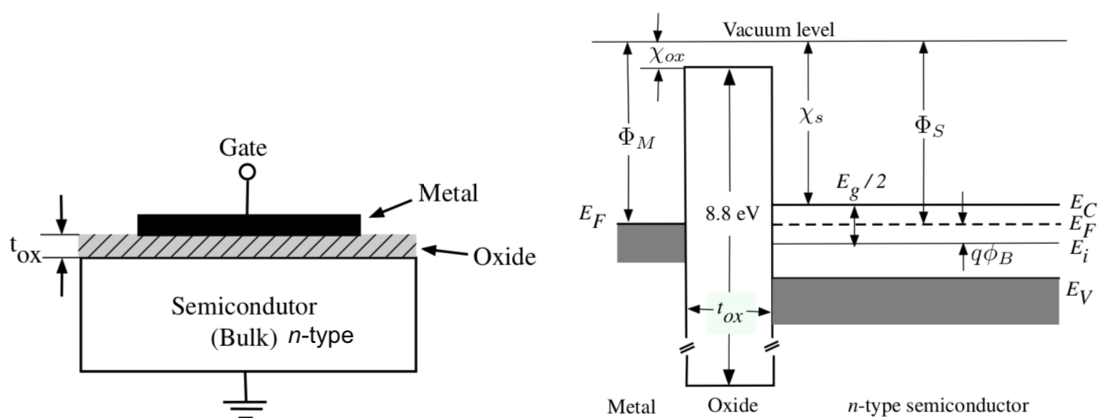

Figure 3.3: Schematic structure of metal-oxide-semiconductor capacitor (left) and its energy band diagram [4].

$$q\phi_{B_p} = E_i - E_F = k_B T \ln \frac{N_A}{n_i}. \tag{3.32b}$$

The semiconductor work function Φ_S can be calculated using the silicon electron affinity $\chi_s = 4.05\,\text{eV}$, which is the energy difference of the conduction band and the vacuum level, giving

$$q\Phi_{S_n} = q\chi_s + E_c - E_i - q\phi_{B_n}, \tag{3.33a}$$

$$q\Phi_{S_p} = q\chi_s + E_c - E_i + q\phi_{B_p}. \tag{3.33b}$$

The energy required to excite an electron from the Fermi level to the vacuum level is the so-called work function. As the work function of a metal Φ_M does not equal the work function of the semiconductor Φ_S, the so-called flat-band voltage V_{FB} has to be applied to achieve the flat-band condition

$$V_{FB} = \Phi_M - \Phi_S. \tag{3.34}$$

This equation can only be used in the case of a charge free oxide and/or silicon-oxide interface. If charges are present, the expression has to be adapted accordingly [30].

Accumulation

Suppose a voltage V_{FB} and $V > V_{FB}$ is applied to the metal gate. In that case, excess electrons will be present at the Si-SiO_2 interface, and the potential at the interface will adapt in the positive direction, causing the energy bands to bend

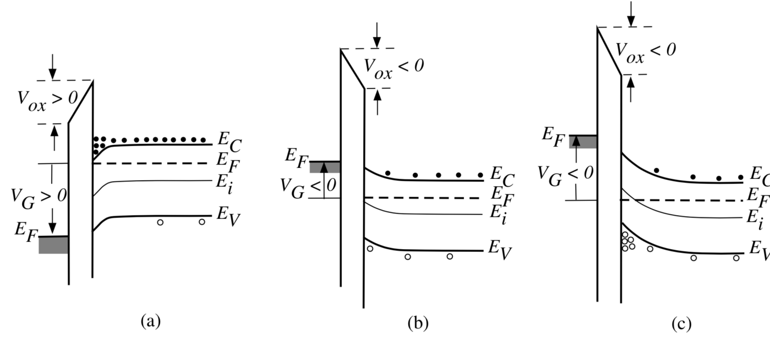

Figure 3.4: Energy band diagram of an n-type MOS structure: (a) accumulation, (b) depletion, (c) inversion. Adopted from [4].

downwards. In this case, the carrier concentration in the semiconductor has an exponential dependency on the energy difference $E_F - E_i$, i.e.

$$\frac{n}{n_i} = \exp\frac{E_F - E_i}{k_B T}. \tag{3.35}$$

The downward bending causes a lowering of the energy $E_F - E_i$, thus giving rise to an accumulation of electrons near the semiconductor-oxide interface. This process is the so-called accumulation mode of a MOS structure. The corresponding energy band diagram is shown in Figure 3.4a.

Depletion

When a voltage $V \leq V_{FB}$ is applied to a MOS structure, the energy bands will bend upwards, electrons are repelled from the surface, and a depletion layer is created. An abrupt change approximation from space charge to the undepleted region can be used to find the electric properties of the depletion region, as the charge carrier concentration will drop to a negligible value compared to the doping concentration on a very short distance. The depletion-layer surface-charge density Q_B, electric field $\mathcal{E}_s$ and potential Ψ_s at the semiconductor surface can be expressed through the depletion-layer depth d_s as

$$Q_B = qN_D d_s, \tag{3.36a}$$

$$\mathcal{E}_s = -\frac{qN_D}{\epsilon_s\epsilon_0} d_s, \tag{3.36b}$$

$$\Psi_s = -\frac{qN_D}{2\epsilon_s\epsilon_0} d_s^2. \tag{3.36c}$$

The electric field in the oxide $\mathcal{E}_{\mathrm{ox}}$ can be derived from $\mathcal{E}_s$ as

$$\mathcal{E}_{\text{ox}} = \frac{\epsilon_s}{\epsilon_{\text{ox}}}\mathcal{E}_s = -\frac{qN_D}{\epsilon_{\text{ox}}\epsilon_0}d_s. \tag{3.37}$$

For the relation between applied voltage and the depth of the depletion layer, we get

$$V - V_{FB} = \Psi_s + d_{\text{ox}}\mathcal{E}_{\text{ox}} = -\frac{qN_D}{\epsilon_0}d_s(\frac{d_s}{2\epsilon_s} + \frac{d_{\text{ox}}}{\epsilon_{\text{ox}}}). \tag{3.38}$$

The depth of the depletion layer is then given as

$$d_s = \sqrt{\frac{\epsilon_s\epsilon_0}{qN_D}(V_{FB} - V) + \left(\frac{\epsilon_s}{\epsilon_{\text{ox}}}d_{\text{ox}}\right)^2} - \frac{\epsilon_s}{\epsilon_{\text{ox}}}d_{\text{ox}}. \tag{3.39}$$

To bend the energy bands upwards, a potential Ψ_s of size

$$\Psi_s = -\frac{qN_D}{2\epsilon_s\epsilon_0}d_s^2 \tag{3.40}$$

is required. The corresponding band diagram of the depleted case is shown in Figure 3.4b.

Inversion

If the applied negative voltage is further increased, the energy bands will bend even stronger, and the intrinsic energy level at the surface increases beyond the Fermi level ($\Psi_s \leq \phi_B$) as shown in Figure 3.4c, creating an excess of holes at the Si-SiO_2 interface. This situation is known as "weak inversion". When further increasing the negative voltage, the hole concentration will exceed the electron bulk concentration, and the state known as "strong inversion" is reached. Once strong inversion occurs, the surface depletion layer reaches its maximum, i.e.

$$d_{\text{max}} = \sqrt{\frac{4\epsilon_s\epsilon_0\phi_B}{qN_D}}, \tag{3.41}$$

and the charge in depletion layer Q_B can be quantified as

$$Q_{B,\,\text{max}} = qN_D d_{\text{max}} = \sqrt{4\epsilon_s\epsilon_0\phi_B qN_D}. \tag{3.42}$$

The charge per unit area in the semiconductor Q_s is equal to the sum of the charge Q_{inv} in the inversion layer and the charge in the depletion region Q_B. The charge in the inversion layer Q_{inv} is proportional to the applied voltage as the gate voltage

variation causes a charge variation in the inversion layer. The proportionality constant between the charge and the applied voltage is the gate oxide capacitance C_{ox}. For the charge density of the inversion layer, this gives

$$Q_{\text{inv}} = C_{\text{ox}}(V_T - V), \tag{3.43}$$

and the charge in semiconductor Q_s is then equal to

$$Q_s = Q_{\text{inv}} + Q_B = C_{\text{ox}}(V_T - V) + qN_D d_{\text{max}}. \tag{3.44}$$

The voltage V_T is referred to as the threshold voltage. It is the voltage required to form the inversion layer

$$V_T = V_{FB} - 2\phi_B + \mathcal{E}_{\text{ox}} d_{\text{ox}}. \tag{3.45}$$

To reach strong inversion, the surface potential Ψ_s has to be moved twice the distance between the Fermi level and the intrinsic energy level in the undepleted bulk, i.e.

$$\Psi_s = -2\phi_B. \tag{3.46}$$

Considering the term $\mathcal{E}_{\text{ox}} d_{\text{ox}}$ to be equal to

$$\mathcal{E}_{\text{ox}} d_{\text{ox}} = -\frac{Q_{B,\,\text{max}}}{\epsilon_{\text{ox}}\epsilon_0} d_{\text{ox}} = -\frac{Q_{B,\,\text{max}}}{C_{\text{ox}}}, \tag{3.47}$$

equation 3.45 can be rewritten as

$$V_T = V_{FB} - 2\phi_B - \frac{\sqrt{4\epsilon_s\epsilon_0\phi_B q N_D}}{C_{\text{ox}}}. \tag{3.48}$$

A further increase of the negative gate voltage below the threshold voltage V_T will cause a large increase of Q_{inv} in the inversion layer, but only a negligible increase of the depletion depth. The depletion depth thus remains a constant at d_{max}. The MOS device with an n-type substrate is commonly referred to as pMOS since the inversion layer is due to holes attracted to the oxide-semiconductor interface. Correspondingly, the MOS device with a p-type substrate is known as nMOS since the electrons are attracted to the oxide-semiconductor interface.

3.2.2 Capacitance-Voltage Characteristics

The capacitance-voltage characteristics provide valuable information about the structure and properties of the MOS device, e.g. determining the oxide thickness d_{ox},

the substrate doping concentration N_D, the flat-band voltage V_G or the threshold voltage V_T. The C-V curve is measured by adding a small sinusoidal signal to a constant DC bias voltage V_G of the MOS device, where sinusoidal capacitive current is measured. The capacity is then calculated as the ratio of the measured capacitive current and the applied sinusoidal voltage. As three different biasing situations of a MOS device are possible, the C-V characteristic will reflect this change and show different behaviour according to the applied gate voltage. It is to note that C-V characteristic is frequency dependent and the change is the most dominant in the inversion case as a certain time is needed to generate minority carriers in the inversion layer. A low frequency measurement maintains thermal equilibrium at all times. At high frequency measurements, one observes that the charge in the inversion layer does not change from the equilibrium value depending on the applied DC voltage. The high frequency capacitance therefore reflects only the charge variation in the depletion layer and the (rather small) movement of the inversion layer charge. Here, only the low frequency and high enough frequency cases, for which thermal equilibrium conditions are met, are discussed.

To obtain the capacitance-voltage characteristic, a simple capacitance model, assuming abrupt-change approximation and series connection of two capacitors (oxide capacitance and depletion layer capacitance), can be used. In the accumulation case, only the oxide layer contributes to the capacitance, as no depletion layer exists. This situation can be described as

$$C = C_{\text{ox}} = \frac{\epsilon_{\text{ox}}\epsilon_0}{d_{\text{ox}}}, \text{ for } V_G \geq V_{FB}. \tag{3.49}$$

For the depletion mode, two capacitances connected in series have to be considered, giving

$$C = \frac{C_{\text{ox}}C_s}{C_{\text{ox}} + C_s} = (\frac{1}{C_{\text{ox}}} + \frac{d_s}{\epsilon_s})^{-1}, \text{ for } V_T < V_G < V_{FB}, \tag{3.50}$$

where the depletion width d_s varies with the applied gate voltage V_G as given by equation 3.39.

In the case of inversion, the capacitance becomes independent of the applied voltage. The low frequency capacitance during inversion is given by the oxide capacitance $C = C_{\text{ox}}$ as the depletion layer width stays constant and changes happen only in the inversion layer surface charge density. In addition to the gate voltage, the high frequency capacitance is measured by applying also an AC voltage. At high frequencies, the inversion layer stays constant, while the depletion layer width varies

with the applied voltage. Hence, the capacitance at high frequencies are given by the oxide capacitance and by depletion layer capacitance

$$C = (\frac{1}{C_{\text{ox}}} + \frac{d_s}{\epsilon_s})^{-1}, \text{ for } V_G \leq V_T. \tag{3.51}$$

The frequency relation of the MOS C-V curve depends on electron and hole lifetime and the energy levels of the defects in silicon. As an example an ideal MOS C-V curve is shown in Figure 3.5 based on the abrupt change approximation and simple capacitance model described above. A MOS device with a SiO_2 thickness of $d_{\text{ox}} = 200\,\text{nm}$ on a silicon substrate with doping concentration $N_D = 1 \cdot 10^{13}\,cm^{-3}$ was assumed. Firstly, a flat band voltage has to be calculated as given by equation 3.34, where $\Phi_M = 4.1\,\text{eV}$ if a gate electrode is made from aluminium. The work function of silicon can be calculated as

$$\Phi_S = \chi_s + E_{g_s}/2 - \phi_B, \text{ where } \phi_B = k_B T \ln \frac{N_D}{n_i}. \tag{3.52}$$

For the flat-band voltage this yields $V_{FB} = -0.39\,V$. Similarly, a threshold voltage can be calculated with the usage of equation 3.48, assuming that $\epsilon_s = 11.7$ [31] and $\epsilon_{\text{ox}} = 3.9$ [32]. This results in a threshold voltage of $V_T = -0.68\,V$. Once V_{FB} and V_T are known, capacitance for each of the three regions (accumulation, depletion and inversion regions) can be evaluated according to equations 3.49–3.51. The resulting approximated C-V characteristic of MOS capacitor is shown in Figure 3.5.

3.2.3 Discussion to p-Type MOS

In the previous paragraph, the MOS device characterization was based on an *n*-type semiconductor as many EuXFEL detectors use it as a primary building sensor component. The following paragraph describes the differences between the *n*-type and the *p*-type MOS devices and provides the most relevant relations for the *p*-type MOS.

As explained previously, accumulation in the *n*-type MOS occurs by applying a positive voltage to the metal gate. On the contrary, to operate the *p*-type MOS in accumulation mode, a negative voltage has to be applied to the gate. The negative charge on the gate attracts holes from the substrate to accumulate near the oxide-semiconductor interface.

Following the mechanisms described for the *n*-type MOS, the depletion of the *p*-type MOS happens by applying a positive voltage. In this situation, the applied electric field repels holes from the interface region and a depletion layer forms.

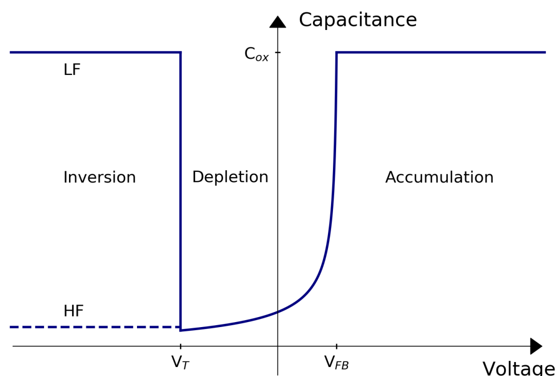

Figure 3.5: Capacitance-voltage characteristic of n-type MOS on silicon substrate with doping concentration of $N_D = 1 \cdot 10^{13}\,\mathrm{cm}^{-3}$ and silicon dioxide thickness of $d_{\mathrm{ox}} = 200\,\mathrm{nm}$. For the calculation of a MOS C-V, a simplified capacitance model with abrupt-change approximation was used. The dashed line represents inversion capacitance at high frequency. No difference exists between low frequency (LF) and high frequency (HF) in the other regions.

When the applied voltage is further increased, the depletion layer goes deeper into the silicon and the concentration of electrons increases, forming an inversion layer at the oxide-semiconductor interface. The maximum width of the depletion layer is given as

$$d_{\mathrm{max}} = \sqrt{\frac{4\epsilon_s \epsilon_0 \phi_B}{q N_A}}. \tag{3.53}$$

The threshold voltage beyond which the inversion occurs is for the p-type MOS device given as

$$V_T = V_{FB} + 2\phi_B + \frac{\sqrt{4\epsilon_s \epsilon_0 \phi_B q N_A}}{C_{\mathrm{ox}}}. \tag{3.54}$$

The capacitance-voltage characteristics of the p-type MOS device is shown in Figure 3.6.

3.2.4 Si-SiO$_2$ MOS Structure

The Si-SiO$_2$ MOS structure is one of the most used and extensively studied metal-oxide-semiconductor systems. The major difference between an ideal MOS structure and a real Si-SiO$_2$ system is the presence of oxide charges in the SiO$_2$ bulk and at the Si-SiO$_2$ interface which will have an influence on the behaviour of a MOS structure.

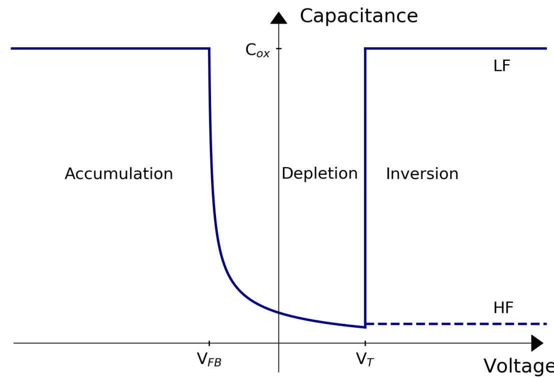

Figure 3.6: Capacitance-voltage characteristic of p-type MOS on silicon substrate with doping concentration of $N_D = 1 \cdot 10^{13}\,\mathrm{cm}^{-3}$ and silicon dioxide thickness of $d_{\mathrm{ox}} = 200\,\mathrm{nm}$. The dashed line represents inversion capacitance at high frequency (labelled as HF). Inversion capacitance at low frequency is labelled as LF.

The properties and nature of such oxide charges will be described in the following chapter. These additional charges will change the flat-band voltage, which depends on the amount and distribution of the charge inside the oxide. To illustrate the problem, we consider a sheet of positive charges with a surface charge density σ at a distance x from the metal. This sheet charge will induce charge partially in the semiconductor and partially in the metal and cause a flat-band voltage change of

$$\Delta V_{FB} = -\frac{\sigma x}{\epsilon_{\mathrm{ox}}\epsilon_0}. \tag{3.55}$$

As can be seen from eq. 3.55, the flat-band voltage depends on both, the surface density of the sheet charge σ and its position within the oxide x. If the sheet charge is located very close to the metal ($x = 0$), no charge will be induced in the silicon and the flat-band voltage V_{FB} will not change. On the other hand, if the charge is very close to the semiconductor, the change in flat-band voltage will reach its maximum. The distribution of charge within the oxide as well as its effect on the flat band voltage will be described in the subsequent chapter.

Chapter 4

X-ray Radiation Induced Defects in Silicon

The detectors' performance in a harsh radiation environment degrades due to the absorbed radiation dose inducing and triggering changes in the detector material. The basics principles of radiation-induced damage will be introduced in this chapter to understand the effects leading to radiation damage and degradation of detectors performance.

Radiation damage effects can be divided into two classes: bulk damage and surface damage. Bulk damage is caused by the interaction of an incident particle with the nuclei of the lattice atoms, causing their displacement from their lattice location [33, 34]. The displacement results in the creation of a Frenkel pair, silicon interstitial and a left-over vacancy. To displace a silicon atom from its lattice position, a minimum recoil energy E_d of approximately 25 eV [35] has to be imparted. Photons need an energy of at least 300 keV [36] in order to provide sufficient energy to create a Frenkel pair. For photon energies < 300 keV, surface driven effects are expected, i.e. damage mainly at the Si-SiO_2 interface. Hence for the EuXFEL energy range (0.25 keV $-$ 25 keV) only surface damage needs to be considered. In the following, only these relevant surface damage mechanisms are discussed in detail.

4.1 The Si-SiO_2 Interface

The symmetry of a silicon crystal is strongly disturbed at its surface due to termination of silicon crystal periodicity as cutting a crystal at some crystal plane leaves open or "dangling" bonds. Considering that the density of silicon atoms at the surface is $\approx 10^{15}\,\mathrm{cm}^{-2}$, this results in the same amount of open bonds. As the

silicon surface is oxidized, most of the bonds will be bound to oxygen, but some will remain open. The term interface trap corresponds to an interface trivalent Si atom with an unpaired valence electron. As the interface traps are electrically active, the following behaviour is expected:

- The interface traps act as generation–recombination centres. They can capture and emit electrons and holes. In the detector's space charge region, this leads to an increase of the reverse-bias current;
- The interface traps act as trapping centres, capturing electrons or holes. Consequently, these are then re-emitted with some time delay. This will lead to less efficient detection in a detector as the amount of the trapped charge will reduce the signal;
- The interface traps change the charge density in the space charge region. The detector thus requires a higher bias voltage to make the detector fully sensitive.

As already mentioned in 3.2.4, the Si-SiO_2 interface contains oxide charges, which are of different type. A classification of these charges following Deal [37] is shown in Figure 4.1. It includes interface-trapped charges (it), fixed-oxide charges (f), oxide-trapped charges (ot) and mobile ionic charges (m). For the quantification of oxide charges, the following quantities are used: the charge per unit area at the Si-SiO_2 interface Q ($\mathrm{C \cdot cm^{-2}}$), the number of charges per unit area N ($\mathrm{cm^{-2}}$), the charge density D in units of ($\mathrm{cm^{-2} \cdot eV^{-1}}$) and the volume charge density ρ ($\mathrm{cm^{-3}}$).

Interface-trapped charges (Q_{it}, N_{it}, D_{it}): These are positive or negative charges in the Si-SiO_2 interface. They occur because of the electronic energy levels located at the Si-SiO_2 interface with energy states in the silicon band gap that can capture or emit electrons or holes. The electronic energy levels are due to structural defects, oxidation-induced defects, metal impurities or defects caused by radiation bond-breaking processes. They are dependent on the chemical composition of the interface, and the interface trap density D_{it} is orientation dependent. For <100> crystal orientation, the interface trap density is approximately one order of magnitude smaller than for <111> orientation [19].

Fixed-oxide charges (Q_f, N_f): This is a positive charge located in the transition region of the Si-SiO_2 interface within approximately 3 nm distance from the interface [19]. It is a charge created during the oxidation process; when oxidation is finished, some ionic silicon can be left near the interface and, together with open silicon bonds (e.g., Si-Si or Si-O bonds) at the surface, may result in a positive

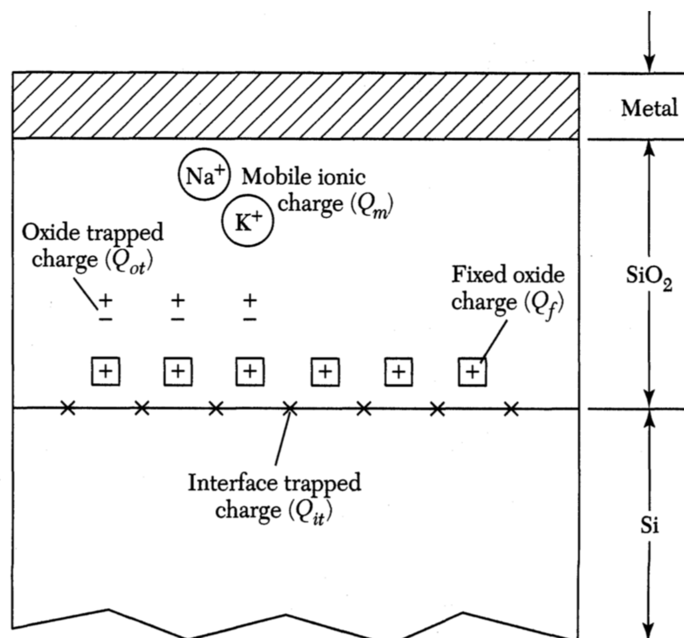

Figure 4.1: Terminology of the charges associated with thermally oxidized silicon. Adopted from [19].

interface charge Q_f. This charge is fixed and can not change its charge state by exchanging mobile carriers with silicon. It is dependent on oxidation and annealing conditions and as well on silicon orientation. It can be regarded as a charge sheet located at the Si-SiO_2 interface. Typical fixed-oxide charge densities for a carefully treated Si-SiO_2 interface system are about $10^{10}\,\mathrm{cm}^{-2}$ for <100> oriented silicon and about $5 \times 10^{10}\,\mathrm{cm}^{-2}$ for <111> oriented silicon [19].

Oxide-trapped charges (Q_{ot}, N_{ot}): The oxide-trapped charges are associated with the electrons or holes trapped in the bulk of the oxide. They can be both positively or negatively charged. They may result from X-ray radiation, high-energy electron bombardment or similar processes. Most of the oxide-trapped charges can be removed by low-temperature (<500 °C) annealing.

Mobile ionic charges (Q_m, N_m): Impurities such as alkali ions Na^+, K^+, Li^+, primarily cause the mobile ionic charges which are mobile within the oxide under raised temperature (>100 C°) and high electric field operation. Under high-bias or high-temperature conditions, ions may move freely and cause a shift of the C-V curves along the voltage axis.

As discussed in 3.2.4, the presence of oxide charges causes the C-V curve of the real MOS diode to deviate from the ideal one, as will be shown later in this section. The following discussion is based on the work done by Sze and Lee [19]. To exemplarily

evaluate the influence of the charges as mentioned earlier, a positive sheet charge per unit area Q_{ox} within the oxide as illustrated in 4.2 will be used. This charge induces negative charges both to the metal and semiconductor, as shown in the top left panel of Figure 4.2. The field distribution shown at the bottom left panel of Figure 4.2 was obtained by integrating the Poisson's equation under the assumption of $\Delta\Phi = 0$.

To reach the flat-band condition, i.e. no charge is induced in the semiconductor (Fig.4.2 top right), a negative voltage has to be applied to the metal. With the increasing negative voltage, the electric field distribution shifts downward until the electric field at the semiconductor surface is zero (Fig.4.2 bottom right). This corresponds to the condition

$$V_{FB} = -\mathcal{E}_{\text{ox}} x_{\text{ox}} = -\frac{Q_{\text{ox}}}{\epsilon_{\text{ox}}} x_{\text{ox}} = -\frac{Q_{\text{ox}}}{C_{\text{ox}}} \frac{x_{\text{ox}}}{d_{\text{ox}}}. \tag{4.1}$$

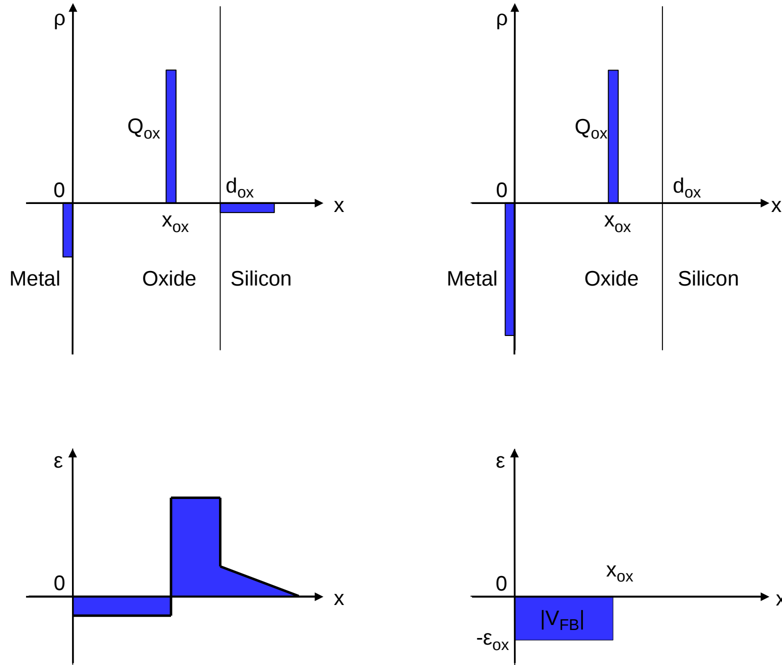

Figure 4.2: Visualization of the sheet charge effect within the oxide. The top left panel shows the SiO_2 sheet charge Q_{ox} inducing charges in the metal and silicon, characterized by volume charge density ρ. The bottom left panel visualizes the electric field ϵ distribution of charges when $V_G = 0$. The right half of the plot shows the same charges (top) and electric field (bottom) when $V_G = V_{FB}$, i.e. under the flat-band condition. Figure adapted from [19].

For the general case of an arbitrary charge distribution within the oxide, we get a flat-band voltage

$$V_{FB} = -\frac{1}{C_{\text{ox}}}\frac{1}{d}\int_0^{d_{\text{ox}}} x\rho(x)dx. \tag{4.2}$$

The volume charge densities of the oxide-trapped charges $\rho_{ot}(x)$ and of the mobile ionic charges $\rho_m(x)$ are defined as

$$Q_{ot} \equiv \frac{1}{d_{\text{ox}}}\int_0^{d_{\text{ox}}} x\rho_{ot}(x)dx, \tag{4.3a}$$

$$Q_m \equiv \frac{1}{d_{\text{ox}}}\int_0^{d_{\text{ox}}} x\rho_m(x)dx, \tag{4.3b}$$

For the case of fixed-oxide charges, which are located very close to the Si-SiO_2 interface, i.e. $x_{\text{ox}} = d_{\text{ox}}$ acknowledging equation 4.1 we find for Q_f

$$Q_f = \frac{Q_{\text{ox}}}{C_{\text{ox}}}. \tag{4.4}$$

Under the assumption that the MOS work function $\Phi_{MS} \neq 0$ and the number of interface-trapped charges is negligible, the flat-band voltage of the real MOS diode will equal to

$$V_{FB} = \Phi_{MS} - \frac{(Q_f + Q_m + Q_{ot})}{C_{ox}}. \tag{4.5}$$

This will cause a shift of the C-V curve as shown in Figure 4.3. Curve a) represents the ideal MOS C-V curve and b) the curve shifted by the amount given by equation 4.5. Additionally, for a high density of interface-trapped charges the curve as illustrated by Figure 4.3, will be parallel shifted and distorted due to the dependency of interface-trapped charges density on the surface potential.

4.2 Physical Processes Underlying Surface Defects Induced by Radiation

The major physical processes leading to radiation-induced surface damage will be discussed in the following based on Mclean and Oldham [38], and Schwank et al. [39]. Figure 4.4 shows a schematic energy band diagram of a MOS device indicating the main processes leading to the build-up of surface damage induced by radiation. In this case, the MOS structure is biased with a positive voltage and exposed to X-ray radiation. The incoming radiation creates electron-hole pairs. In SiO_2, due to

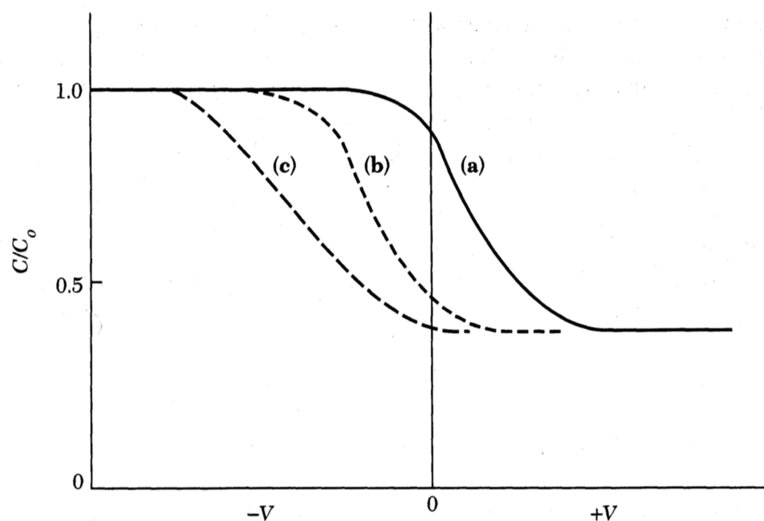

Figure 4.3: Effect of oxide charges and interface traps on the MOS C-V curve: a) Ideal MOS C-V curve, without oxide charges. b) Parallel shift of the curve due to fixed-oxide charge, mobile ionic charge and oxide-trapped charge present in SiO_2. c) Parallel shift and distortion of the C-V curve due to interface traps. Figure adopted from [19].

differing mobilities of created electrons and holes [40], the electrons drift within picoseconds towards the gate electrode. However, a fraction of the electrons and holes will recombine. It is to note that the fraction of recombined electrons and holes depends on the energy and the type of incident radiation [41]. The holes escaping recombination have lower mobility than the electrons and remain close to their generation point, causing a negative threshold voltage shift in a MOS capacitor. As shown in Figure 4.4, electron-hole pair generation/recombination is the first mechanism of MOS radiation response. The second process is the transport of holes that escaped the initial recombination in the Si-SiO_2 interface, which is accomplished by hopping through localized states in the oxide. When the holes reach the interface region, a fraction of them falls into deep, long-lived trap states, forming a positive oxide-trap charge. The fourth process is the radiation-induced build-up of interface traps located directly at the Si-SiO_2 interface. As interface traps are highly dependent on the applied electric field, this will result in a voltage-dependent threshold shift. In the following, the above-mentioned processes are described in greater detail.

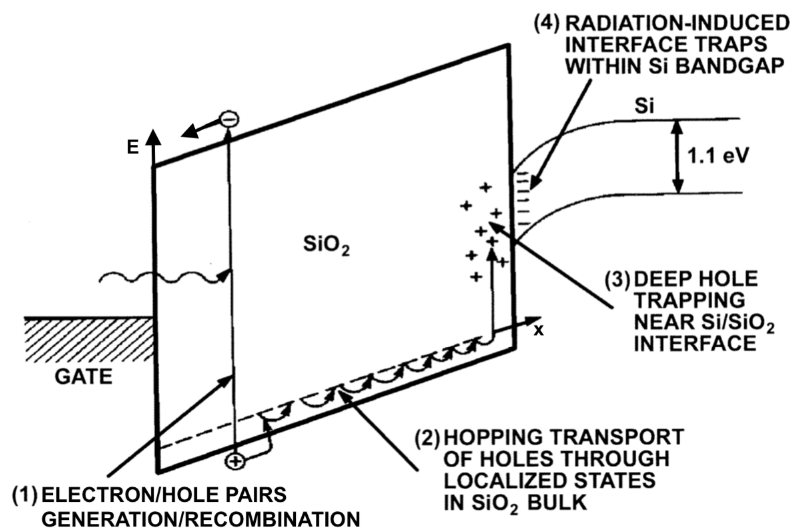

Figure 4.4: Schematic energy band diagram of a positive biased MOS device, indicating the main processes leading to radiation-induced surface damage. Figure adopted from [42].

4.2.1 Electron-Hole Pair Generation

The number of electron-hole pairs generated by ionizing radiation in SiO_2 depends on the mean energy needed for the generation of one electron-hole pair E_p, which is $E_p = 18\,\text{eV} \pm 3\,\text{eV}$ (Ausman and McLean [43]). A more accurate measurement yields the currently established value of $E_p = 17\,\text{eV} \pm 1\,\text{eV}$ [44]. From the value of E_p, the initial electron-hole pair density per unit dose g_0 can be determined. For SiO_2 this results in $g_0 = 8.2 \cdot 10^{14}\,\text{cm}^{-3}\text{Gy}^{-1}$ [44].

Initial Hole Yield The fraction of holes which escape the initial recombination $f_y(E_{\text{ox}})$ depends on the magnitude of the electric field in the SiO_2 separating the electron-hole pairs and on the initial line density of electron-hole pairs generated by the incident radiation. The line density of pairs is determined by the linear energy transfer and is a function of the incident particle type and energy. Furthermore, the line density is inversely proportional to the average separation distance between electron-hole pairs. Therefore, if the line density is high, the spacing of the pairs is low. For a given electric field, this leads to higher recombination with a lower hole yield. The effect of recombination for various incident particles is shown in Figure 4.5, where the fraction of unrecombined holes is shown as a function of the applied electric field. According to Leray and Paillet [45], the hole yield for X- and

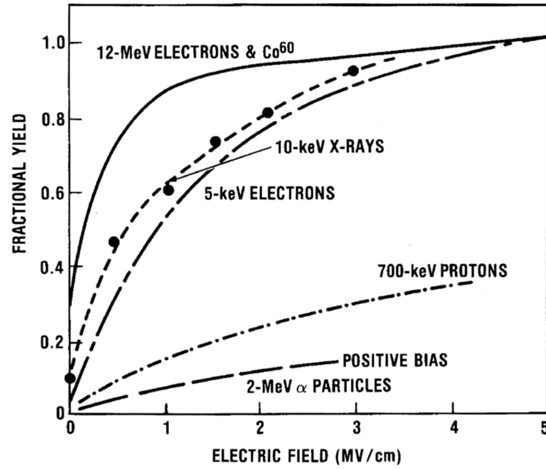

Figure 4.5: The fraction of holes escaping the initial recombination as a function of the applied electric field for different incident particle species. Figure adopted from [42].

γ-rays can be approximated by

$$f_y(E_{\text{ox}}) = \left[1 + \frac{E_c}{E_{\text{ox}}}\right]^{-m}, \tag{4.6}$$

where m and E_c (MV/cm) are coefficients which depend on the radiation type. For 10 keV X-ray photons this results in

$$f_y(E_{\text{ox}}) = \left[1 + \frac{1.35\,\text{MV}\cdot\text{cm}^{-1}}{E_{\text{ox}}}\right]^{-0.9}. \tag{4.7}$$

The total number of holes generated in the oxide that escape the initial recombination, N_h for a given dose D and an oxide thickness d_{ox} is given as

$$N_h = f_y(E_{\text{ox}}) g_0 D d_{\text{ox}}. \tag{4.8}$$

4.2.2 Hole Transport

The transport of holes can be well described by the continuous-time-random-walk hopping transport formalism originally developed by Montroll et al. in [46]. The transfer mechanism is accomplished by polaron hopping of the holes between localized trap states. The moving hole will polarize the neighbouring environment due to its charge forming a polaron. The term polaron refers to the interaction between charge carrier (hole) and surrounding material, creating a lattice distortion in its

immediate vicinity. The polaron increases the effective mass and decreases the mobility of holes. The hole transport in the oxide is highly dispersive, electric field and oxide thickness dependent and above ≈ 140 K also temperature-dependent [42].

4.2.3 Oxide Traps

Due to incomplete oxidation at the Si-SiO_2 transition region, oxygen vacancies are present, acting like trapping centers. These traps are also known as deep hole traps [47]. Oxygen vacancy as presented in [48] is an oxygen atom missing from the SiO_2 lattice leaving a weak Si-Si bond as shown on the left of Figure 4.6, where each Si atom is bonded to three oxygen atoms. After a hole is trapped, the Si-Si bond is broken and the lattice relaxes into two configurations. The silicon atom obtains an unpaired electron and remains in a tetrahedral configuration, while the other silicon atom possesses the trapped hole with a positive charge and relaxes into a planar configuration of the three remaining oxygen atoms as depicted on the right plot of Figure 4.6. This asymmetrical relaxation is possible due to the flexibility of the Si-O-Si bond. The defects produced by such an asymmetrically relaxed oxygen vacancy are known as E' centres and play the most important role in radiation damage related to oxide traps. Oxygen vacancies occur in the greatest density close to the Si-SiO_2 interface due to the lattice mismatch between the silicon bulk and the oxide and due to the diffusion of oxygen from the oxide to the interstitial sites in the Si substrate.

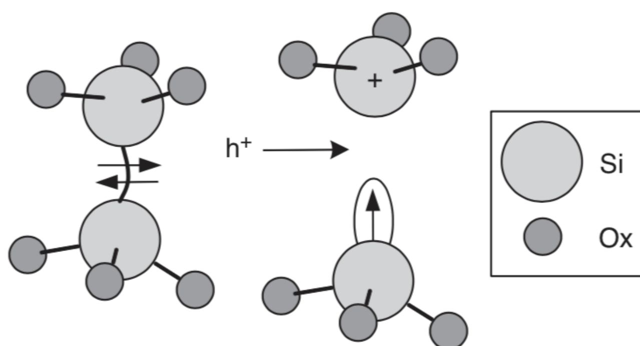

Figure 4.6: Model of an oxide trap creation in SiO_2. The left half of the plot illustrates the oxygen vacancy and week Si-Si bond. After a hole is trapped, the bond is broken, and two configurations are created; silicon with an unpaired electron and silicon with the trapped hole (shown on the right half). Figure adopted from [49].

As oxygen vacancies act like trapping centres, a fraction of holes approaching the interface will be trapped. The fraction of trapped holes is given by the capture cross-section near the interface, which depends on the applied electric field and fabrication process. The number of trapped holes can vary between a few percent for radiation-hard oxide to as much as 50 to 100% for radiation-soft oxide. The positive charge of trapped holes causes a negative threshold voltage shift in the MOS capacitor.

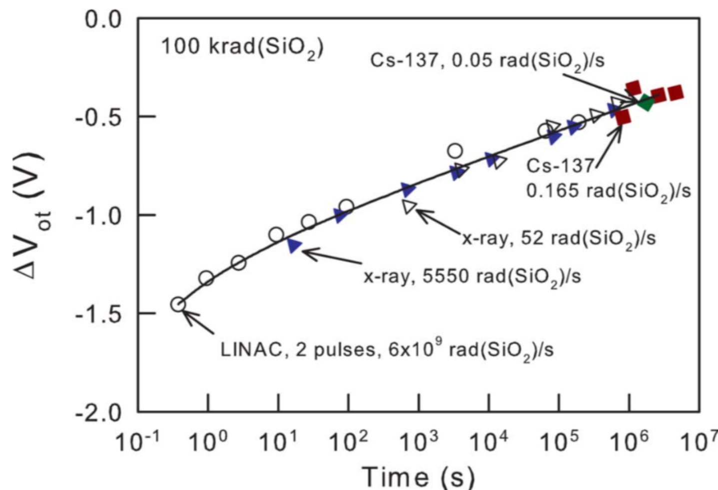

Figure 4.7: Threshold voltage shift due to oxide-trapped charge as a function of time for different levels of irradiation to indicate oxide traps neutralization. Figure adopted from [39].

Oxide-trapped holes undergo a long-term annealing process, sometimes lasting up to years. The time dependence of trapped hole neutralization at room temperature is shown in Figure 4.7, where the oxide-trapped charge induced threshold voltage shift ΔV_{ot} is plotted as a function of time for radiation-hard MOS designs. The neutralization or trapped-hole annealing proceeds by two mechanisms: 1) the tunnelling of electrons from silicon into either oxide traps or electron traps associated with trapped holes, and 2) the thermal emission of electrons from the oxide valence band into oxide traps. The rate at which charge neutralization occurs is strongly affected by the spatial and energy distribution of the oxide traps. For tunnelling, a close vicinity of oxide traps and the Si-SiO_2 interface is required. For thermal emission to occur, the energy levels of oxide traps have to be close to the oxide valence band.

For a sample annealed under a positive bias at 100 °C, it was observed that part of the trapped charge is restored after applying a negative bias, while the other part

of the trapped charge is removed. This led to an idea that instead of an electron tunnelling to the positively charged Si and neutralizing it to reform the Si-Si bond, it tunnels to the neutral Si, forming a dipole structure, where the electron can tunnel back and forth to the substrate in response to bias change [50, 51]. Such oxide traps which can communicate and exchange charge with the silicon substrate are known as border traps. The border traps can be mistakenly accounted for interface traps in C-V measurements.

4.2.4 Radiation-Induced Interface Traps

Interface traps are amphoteric defects, having two energy levels in the Si band gap. Traps in the lower half of the band gap act like donors, i.e. if the Fermi energy at the interface is below the trap energy level, the trap "donates" an electron to the silicon. The trap is hence positively charged. Similarly, the traps in the upper part of the band gap behave like acceptors. Similar to when the Fermi level is above the trap energy level, the trap "accepts" an electron from the silicon. Thus, the trap is charged negatively. Considering an n-type MOS structure under the flat-band condition, the electrons occupy states below the Fermi energy. Therefore, the states in the lower half of the band gap are neutral (occupied donors). The states between midgap and the Fermi energy are negatively charged (occupied acceptors), and the states above the Fermi energy are neutral (unoccupied acceptors). Applying a bias voltage in accumulation mode bends the bands down and thus increases the number of occupied acceptors. In inversion mode, the fraction of interface traps between the midgap and the Fermi level consists now of unoccupied donors, thus leading to a positively charged interface causing a negative threshold-voltage shift.

Interface-trap build-up is a much slower process than the oxide-trap build-up, taking up to 10^3 s until saturation is reached after exposure [42]. The radiation-induced interface trap is based on a Si-atom bound to three Si-atoms and an H-atom. The dominant process has been initially described by McLean [52]. When the Si-H bond is broken, the Si is left with an unpassivated dangling bond. The Si-atom is then depassivated during a two-stage process. In the first stage, radiation-induced holes transport through the oxide and liberate hydrogen in the form of protons. During the second stage, the protons undergo hopping transport to the interface, where they break SiH bonds, creating H_2 and trivalent Si defect. However, other models assume diffusion of neutral hydrogen rather than the drift of protons as the main mechanism for interface trap production. However, the effect of neutral

hydrogen was discovered to be small. The effect called a latent interface trap build-up was also observed and originates in hydrogen diffusion into the gate oxide region, presumably from the field oxide or an encapsulating layer. The latency is caused by diffusion happening on relatively long distances. This effect is difficult to measure as its time scale is beyond the typical duration of laboratory tests, i.e. up to scales of months.

4.3 Factors Influencing Surface Damage

The density of radiation-induced charges, i.e. oxide-trapped charges and interface-trapped charges, are sensitive to operating conditions during irradiation. The most important aspects influencing the level of produced charges, hence the overall radiation-induced damage, will be discussed.

4.3.1 Oxide Layer Thickness

Oxide layers with a thickness in nanometre range lead to an effect known as dose enhancement. Dose enhancement is an effect that arises in the regions near interfaces between materials with different atomic numbers if irradiated with photons. In a MOS capacitor, it is due to the Si substrate material and the Al gate material, which have different atomic mass and total photon interaction cross-sections than SiO_2. This leads to the uneven production of secondary electrons in the adjacent materials causing a dose gradient. The effect is largest for low-energy photons because most of the energy deposition happens via the photoelectric effect as described in section 2.2. The critical aspect for the dose enhancement effect is charged particle equilibrium (CPE). In a homogeneous material, the number of secondary electrons scattering into an increment of volume is equal to the number of electrons scattering out. When the MOS device consists of several thin layers of different materials with different total cross-sections, the CPE is not maintained. This happens because more secondary electrons cross an interface from the high-Z side than from the low-Z side [42]. Figure 4.8 visualizes the difference in the observed dose for a MOS device with a thick (left panel) and thin (right panel) oxide layer. Solid lines in both plots indicate a dose calculated for 10 keV X-rays, using the mass absorption coefficients alone, without secondary electron transport. The dashed line represents the observed dose when secondary electron transport is evaluated. For a thin oxide layer, the secondary electrons can pass through the entire oxide, thus enhancing the

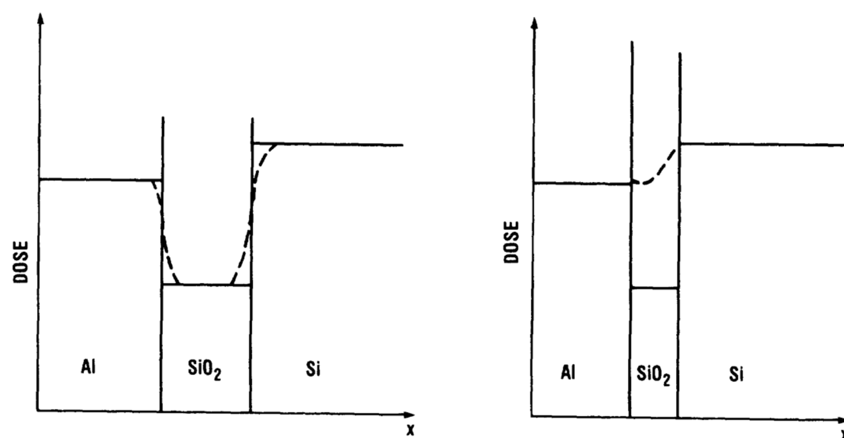

Figure 4.8: Schematic diagram of the dose enhancement effect in the MOS structure with a thick (left plot) and thin (right) oxide layer. Solid lines show the equilibrium bulk dose. Dashed lines represent the actual dose. Figure adopted from [53].

absorbed dose. The oxide thickness has to be at least the thickness of the average secondary electron range to maintain equilibrium, which for 10 keV X-ray photons is $\approx$ 500 nm. As reported in [41], approximately 80% of the incident intensity is transmitted through the 200 nm thick Al gate. However, in the first 100 nm of oxide, almost all of the energy deposition occurs. The dose enhancement factor (DE) can be defined as

$$DE = \frac{\text{local dose in transition region}}{\text{equilibrium bulk dose}}. \tag{4.9}$$

Figure 4.9 shows the dose enhancement factor as a function of oxide thickness. A dose enhancement effect is clearly observable for low-energy X-rays, with an enhancement factor of $\approx$ 1.5 for oxide thickness of 100 nm (black dots labelled as "This work").

4.3.2 Dose-Rate Effects

Different dose rates result in different densities of electron-hole pairs. The density of electron-hole pairs for a high dose rate is larger than that for a low dose rate. As previously described in section 4.2.1, a higher dose rate will lead to increased recombination, hence to a lower overall dose and consequently to less radiation-induced charges. Dose rate effects are observed when a given dose is delivered at different rates in different measurements due to the varying irradiation times.

An additional explanation exists for the lower density of radiation-induced charges

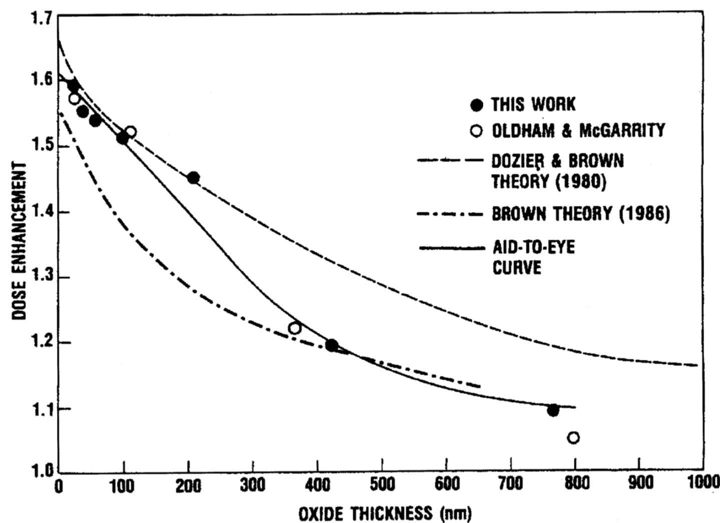

Figure 4.9: Measured and calculated dose enhancement as a function of SiO_2 thickness for 10 keV X-rays. Adopted from [44].

in the case of high dose rates. The accumulated oxide traps result in a space charge which alters the electrical field of the SiO_2 layer. When a positive gate bias is applied, the accumulation of positive charge in the oxide enhances the electrical field between the space-charge region and the silicon. It reduces the electrical field between the space charge and the gate to almost zero. The altered local oxide field will alter the local charge yield and enhance the recombination of electrons and trapped holes.

Fleetwood *et al.* concluded [54] that the build-up of interface traps with post-irradiation annealing time is independent of the dose rate if the time of post-irradiation annealing after the short irradiation (higher dose rate) equals the time of the irradiation with a lower dose rate.

4.3.3 Time and Temperature Effects

Radiation induced charges that are built up in the SiO_2 and at the Si-SiO_2 interface undergo an annealing process. The annealing process is time and temperature dependent with significant variations depending on the nature of the oxide charges. In general, higher annealing temperature and longer annealing times results in more oxide and interface-trap charges being cured. However, at some temperatures reverse annealing may occur, i.e. the charge density increases with the annealing time and hence an optimal ratio between the annealing time and temperature has to be

found.

4.4 Effects of Induced Radiation on MOS Devices

4.4.1 Threshold Voltage Change

As already shown in section 4.1, charges present in the oxide or at the Si-SiO_2 interface cause an overall shift of the C-V characteristics. The oxide-trapped charges cause a shift of the C-V curve and the threshold voltage. The interface-trapped charges cause distortion and stretch of the C-V curve as shown in Figure 4.3c. For the nMOS capacitor, an increase of the threshold voltage will be observed with an increasing density of the radiation-induced charges. As explained previously, irradiation with a low dose rate under positive bias voltage will lead to a higher threshold voltage increase.

4.4.2 Increase of Leakage Current

A build-up of radiation-induced interface-trapped charge causes an increase of the surface recombination velocity. This leads to larger surface generation currents and thus to a higher leakage current with increasing dose [55]. The increased leakage current will consequently increase the dark current in the detector. The dark current level in the sensor is a crucial characteristic as it impacts many operational parameters of the detector, e.g. noise, dynamic range, and others. A detailed discussion on the detector parameters and the role of leakage current will be discussed in the following chapters.

4.4.3 Decrease of Charge Transfer Efficiency

The radiation-induced charges at the Si-SiO_2 interface act like trapping centres. This effect is very important for charge-coupled devices (CCDs). A charge resulting from a photon interaction has to be transferred through many channels (pixels, where each pixel represents a MOS capacitor) to read out a CCD detector (based on MOS). If part of the charge is trapped during the transfer at the readout node, a lower charge than expected will be measured. The parameter measuring the charge losses in a CCD device is the so-called charge transfer efficiency (CTE), i.e. a ratio of charge transferred between two neighbouring pixels to the total amount of charge contained in the pixel before the transfer

$$CTE = \frac{Q_{n+1}}{Q_n}. \tag{4.10}$$

Increased charge trapping hence decreases the CTE [55], and this reduction will lead to an inaccurate representation of the measured quantities, e.g. wrongly measured energy of the incoming radiation.

4.4.4 Decrease of Breakdown Voltage

As experimentally observed by Blackburn et al. [56] and Pugh et al. [57], the breakdown voltage of a MOSFET is strongly affected by ionizing radiation. The breakdown voltage is significantly decreased with increasing total radiation dose for both n- and p-channel devices (Figure 4.10). It was also shown that the response of a breakdown voltage on the total dose depends on the method used to optimize preradiation breakdown voltage [57].

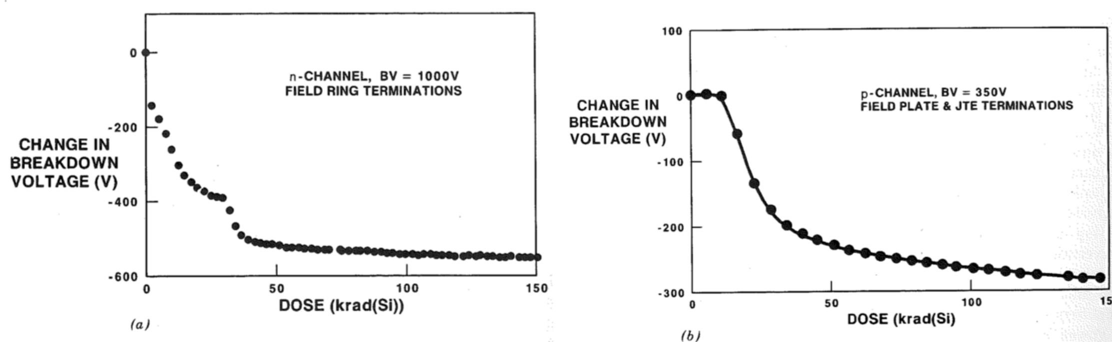

Figure 4.10: Response of breakdown voltage of a high-voltage MOSFETs to increasing radiation dose for n-channel device (left plot) and p-channel device (right plot). Adopted from [58].

4.4.5 Decrease of Charge Carrier Mobility

The charge carrier mobility degrades with increasing radiation dose. The mobility of charges is vital for the detectors operated at high frame rates, e.g. 4.5 MHz detectors at the EuXFEL (see Table 1.1) as the collection of the radiation generated charges has to happen within nanoseconds. Consequently, the decreased charge mobility may result in incomplete charge collection within the integration window of the detector and hence lead to wrongly measured quantities. Sexton and Schwank [59] showed that the mobility decreased is caused by a build-up of interface-trapped charge,

which is induced by radiation. Schwank et al. also showed that the decrease of charge carrier mobility does not depend on the density of the oxide-trapped charge. Figure 4.11 shows a decrease of the carrier mobility with the increasing interface trap density.

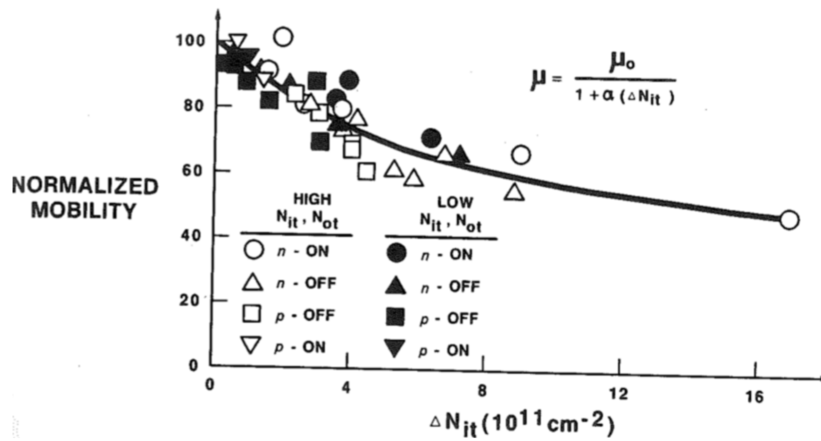

Figure 4.11: Normalized effective channel mobility as a function of radiation-induced interface trap density. Adopted from [58].

Chapter 5

Dissertation Thesis Aims

The main goals of the dissertation thesis can be arranged to the following points:

1. Description of detector parameters, from which radiation damage effects could be estimated and introduction of the tools to analyze and characterize radiation induced effects.
2. Radiation hardness tests of the ePix100a detector in the EuXFEL radiation environment. The detector is important for the scientific operation of the facility. Since it has not been built explicitly for the EuXFEL needs, its tolerance to FEL radiation has not been assessed before.
3. Calculation of the absorbed dose during the observation duration, to analyse impact of the dose to detector components.
4. Understanding the observed radiation damage effects for a specific sensor design.
5. Evaluation of the dose limit reducing the detector operation parameters to such extent that they no longer meet pre-requirements for reliable scientific data production.
6. Estimates on the lifetime of EuXFEL detector systems based on the conducted experiments.

Chapter 6

Detector Performance Parameters Relevant for Radiation Damage

The detector performance parameters that are used to characterize the quality of the data produced by the detector can also be used to indicate radiation-induced damage. The parameters evaluated in the radiation damage study are presented in the following.

6.1 Dark Signal

The dark signal S_d results from a detector signal when the detector is not exposed to any radiation. It has two contributors, i.e. the dark current and the pedestal. The dark current I_{Dark} is due to a current I_t induced by thermally generated electron-hole pairs and an additional leakage current I_l resulting from, e.g. radiation-induced damage, i.e.

$$I_{\text{Dark}} = I_t + I_l \tag{6.1}$$

Ranuárez et al. [60] discuss different components of the leakage current, the models and mechanisms, also involving the role of the radiation-induced interface traps, are presented by Nathan and Das [61] and by Larcher et al. [62].

The pedestal P as used in this thesis is a baseline value generated by detector electronics for its proper functioning, e.g. to avoid negative values at the Analog-to-Digital Converter (ADC) or shift the signal values to a specific ADC range. The contribution of the thermally generated charges can be efficiently decreased by cooling the detector's sensor.

The two parameters associated closely with the dark signal are offset and noise. In general, offset is the average value of the dark signal integrated by the detector, i.e.

$$\text{offset} = \frac{1}{N}\sum_{i=1}^{N}(I_{\text{Dark}} + P). \tag{6.2}$$

The detector's noise represents variations of the dark signal, which are due to contributions of different noise sources, e.g. noise from readout electronics (marked as readout), thermal noise, leakage current variations, and so on. The noise observed at the detector is a superposition of all the contributing sources. A superimposed noise observed for a given detector is usually evaluated by an equivalent noise charge (ENC) given in units of e^- or eV. It is given as

$$ENC_{\text{tot}} = \sigma_{\text{tot}} = \sqrt{\sigma^2_{\text{Thermal}} + \sigma^2_{\text{Leakage}} + \sigma^2_{\text{Readout}} + ...} \tag{6.3}$$

As explained in previous chapters, the radiation-induced damage often induces an increase in the leakage current. Since the leakage current is a contributor to the dark current, its increase will affect both the offset and noise parameters, as shown above. Consequently, the change observed on the offset and noise can be directly linked to the radiation-induced damage, assuming no changes were applied to the sensor or the electronics setup.

6.2 Dynamic Range

The dynamic range of a detector determines its ability to detect low-intensity signals alongside high-intensity signals. In detector systems, where the measured analog quantity is digitized by the ADC, the upper limit is given by the maximal signal the ADC can resolve. The dynamic range is hence given as

$$DR = \frac{\text{Max. signal (e}^-)}{\sigma_{\text{tot}}}. \tag{6.4}$$

As shown in the equation above, the dynamic range represents the signal-to-noise ratio (SNR) for the highest detectable signal, if contribution of the background to the signal is negligible. The lower limit of the dynamic range is determined by the noise of the detector. However, in the detector community, the dynamic range is often understood as the number of ADC levels available for photon detection. The

resolution of the ADC M is usually expressed as bit depth, which represents the number of signal quantization levels

$$N = 2^M, \tag{6.5}$$

which gives a limit to the maximal signal. As explained before, the detector offset is always present in the measured signal, thus acting as a lower limit of the available range of values. Taking the offset as "background" (denoted as "bg"), the number of available levels N_A for our measurement is

$$N_A = N - bg, \tag{6.6}$$

which may then be used to describe the dynamic range of the ADC. This approach is justified if the noise is small in comparison to the overall signal. In the previous section, we have discussed the relation between the leakage current and the detector offset. Analogously, if the offset rises due to radiation-induced leakage current increase, the dynamic range decreases. Hence, we can talk about dynamic range reduction R_{DR}, which can be defined as

$$\begin{gathered} R_{\mathrm{DR}} = \frac{\Delta bg}{N_A}, \\ \text{and } \Delta bg = bg_{\mathrm{post}} - bg_{\mathrm{pre}}, \end{gathered} \tag{6.7}$$

where bg_{pre} and bg_{post} are offset values before irradiation of the detector, respectively after irradiation.

6.3 Energy Resolution

The energy resolution of a detector determines its capability to distinguish photons with different energies. If one considers mono-energetic photons, the number of generated charges will oscillate around the mean value

$$\langle N \rangle = \frac{E}{w}, \tag{6.8}$$

where w is the mean energy needed to create an electron-hole pair (3.65 eV for Si [19]) and E is the energy of the incoming photon. Thie signal osscilation is due to statistical fluctuations in the excitation and ionization processes inside the sensor material. Assuming the charge creation is an independent random process (describable by Poisson statistics), according to the central limit theorem, the distribution

of a sum of a large number of independent variables (generated charges) converges to a normal distribution. Therefore, a Gaussian distribution is often a good description of the shape of a photo-peak with the Full Width at Half Maximum (FWHM) denoting the energy resolution. The measured FWHM of the photo-peak is generally used to describe the energy resolution of a detector. However, as described by U. Fano [63] the energy resolution of a detector is better than described by Poisson statistics as part of the absorbed energy does not invoke ionization but is used for other processes as e.g. lattice vibrations. Hence the process of charge creation is not purely random. The coefficient describing the deviation from Poisson statistics is known as Fano factor F, and it is a material-specific constant. For silicon it amounts to $F = 0.115$ [64]. The energy resolution of a detector is then given as

$$FWHM = 2.355 \times w\sqrt{\frac{FE}{w}}, \tag{6.9}$$

where F is the Fano factor. Additionally, the contribution of the detector noise to the energy resolution has to be considered, yielding

$$FWHM = 2.355 \times \sqrt{RMS^2 + FEw}, \tag{6.10}$$

where RMS (root-mean-square) is the detector noise expressed in eV.

As the energy resolution is also a function of noise, it is expected that a noise increase due to radiation-induced damage will also impact the energy resolution of the detector, resulting in a broadening of the photo-peak.

6.4 Signal-To-Noise Separation

Often, experimental applications (e.g. low energy spectroscopy experiments, imaging experiments) require a detector with single-photon sensitivity, i.e. the capability to resolve single photons from noise. A common requirement for imaging detectors used at FEL facilities is a false hit detection probability per megapixel area, e.g. less than one false hit per million of pixels per image. This approximately corresponds to a photon peak-to-noise separation of $5\,\sigma$ at a certain energy. The lowest acceptable signal-to-noise value is usually considered to be $3\,\sigma$, which corresponds to ≈ 2700 false hits per million pixels. In this context, the detector's noise and the peak width are important performance parameters, which, as already shown, both increase with radiation-induced damage.

6.5 Absolute Gain

In the case of an energy or intensity resolving detector, a relation converting the measured signal into a physical quantity, i.e. energy, is needed. The electrical signal created inside the sensor is amplified, shaped and digitized by the detector electronics. The detector provides output in digital units, so-called Analog Digital Units (ADU). The factor converting the digital unit at the detector output to the physical energy unit at its input is known as absolute detector gain. It is determined by the detector's amplification and digitization stages. The existence of an absolute gain as a conversion coefficient between energy and ADU units is justified when related purely to the measured photo-peak, neglecting the secondary effects of photon redistribution to lower channels, e.g. due to Compton scattering, escape peaks due to internal fluorescence in the sensor material, backscattering[1]or other processes mentioned in section 2.2. Potential changes of the absolute gain due to radiation damage may suggest damage to other detector components, e.g. the pre-amplifier or ADC.

[1]Compton scattering of the incoming photons with the material surrounding the detector at an angle $> 90°$.

Chapter 7

Detector Characterization

The parameters described in chapter 6 are used in this thesis as indicators for radiation-induced damage and provide information about the quality reduction of the produced data. We can evaluate changes in detector performance employing standard detector characterization methods. The basic principles of detector characterization will be therefore discussed.

We can divide the characterization procedures into two categories by the type of detector images used. The first category of procedures uses dark data to estimate the effects of the dark signal, i.e. offset and noise, which we can use to monitor the leakage current increase (see chapter 6). Parameters like energy resolution or absolute gain can be estimated from detector data when illuminated by X-rays. For detector characterization purposes, it is usually desired to irradiate the sensor with photons homogeneously and with the same intensity across the whole sensor area. We refer to such characterization data as flat-field data.

7.1 Dark Characterization

Dark signal characterization of a pixelized detector evaluates detector offset and noise on a per-pixel basis. The result of such a characterization is a set of pixel maps describing the behaviour of the measured dark signal. A value at a defined position in the characterization map refers to the value in a pixel with the same position. Equation 7.1 gives the relation for the offset values, where $p_{x,y,z}$ represent values in a pixel defined by its (x, y) coordinates in a specified image (z). The total number of dark images is specified with N.

$$\overline{p}_{x,y} = \frac{1}{N}\sum_{z=0}^{N-1} p_{x,y,z}. \tag{7.1}$$

.

We use the offset calculated from the dark images to subtract its value from the corresponding images.

Variations in the voltage supplying the readout electronics might induce noise affecting a group of channels with the same value. This effect is the so-called common mode (CM). We determine the CM by calculating the median value per group of channels, e.g. row, column, for which common characteristics exist, e.g. grouping of multiple channels to common readout node. Equation 7.2 gives an example of a common mode calculation for a row. The calculation and correction of the common mode are performed after offset subtraction.

$$\tilde{c}_{x,y,z} = median_{x,z}\left\{s_{x,y,z}|_{y\in[0,N_{ch}]}\right\}, \text{where } s_{x,y,z} = p_{x,y,z} - \overline{p}_{x,y}. \tag{7.2}$$

A noise map is calculated after offset and common mode correction was applied. The noise map is calculated as

$$\begin{aligned} \sigma_{x,y} = \sqrt{\frac{1}{N}\sum_{z=0}^{N-1}(r_{x,y,z} - \overline{r}_{x,y})^2}, \text{where } r_{x,y,z} &= s_{x,y,z} - \tilde{c}_{x,y,z} \\ \text{and } \overline{r}_{x,y} &= \frac{1}{N}\sum_{z=0}^{N-1} r_{x,y,z}. \end{aligned} \tag{7.3}$$

The offset and noise calculation [65] is performed by numerically stable Welford's algorithm [66]. Suppose the calculated offset map or noise map contains pixels, which are significantly above or below the average distribution of values. In that case, these pixels have to be masked and excluded from the analysis.

7.2 X-ray Characterization

The raw flat-field data are corrected for the offset calculated from the dark data taken shortly before the flat-field measurements to keep conditions as similar as possible. Afterwards, the offset corrected data are corrected for common mode. In the next step, we evaluate the charge sharing effect. Charge sharing happens between neighbouring pixels due to the finite size of pixels and charge diffusion. The number of pixels holding charge from one photon event is referred to as an

event pattern. The algorithm [65] evaluates the number of pixels contributing to the event pattern and evaluates if the detected pattern can be attributed to a single photon. The detected pattern is classified as valid only if the neighbouring pixels do not contain another pattern so that the partial charge from the event occurring in the adjacent pixel is excluded. Charge sharing events are classified based on three event thresholds. Primary and secondary threshold are given as $n \times \sigma_{x,y}$. The primary threshold probes the signal in all the pixels, and values exceeding it are marked as photon events. Subsequently, pixels adjacent to a pixel exceeding the primary threshold are checked against the secondary threshold. If any of these pixels exceeds the secondary threshold, the signal is considered to be resulting from the same photon. It is summed up and stored in a pixel containing the highest proportion of the split charge (primary photon incident pixel). It is to note that more-evolved algorithms to correct for a split charge, providing a sub-pixel resolution exist [67]. The upper event threshold verifies if the detected photon event results from an X-ray photon. This is tested by supplying a value in ADU units above which one does not expect the occurrence of the X-ray photon. Event exceeding the upper threshold can result from minimum ionizing particle (MIP), e.g. cosmic ray muon [68]. Event patterns for which no charge sharing with adjacent pixels exist are the so-called single-pixel events (singles). After charge sharing correction, we apply the relative gain correction to remove small pixel-to-pixel variations due to different characteristics of the pre-amplifiers implemented in each pixel. Per-pixel relative gain is calculated using only single-pixel events. These are not biased with the relative differences from other pixels, as is the case for the split event. The calculation is done by estimating a position of a photon peak in each pixel with a Gaussian model and dividing this value by a mean peak position across the whole sensor. A result of the relative gain calculation is a so-called relative gain map. During the relative gain correction, the value in a pixel is divided by a value saved in a relative gain map corresponding to the pixel position.

The spectrum of detected and corrected photon events is modelled with a Gaussian distribution to evaluate energy resolution and the absolute gain of the detector (see chapter 6).

Flowchart of procedures applied on data during characterization process is shown in Figure 7.1.

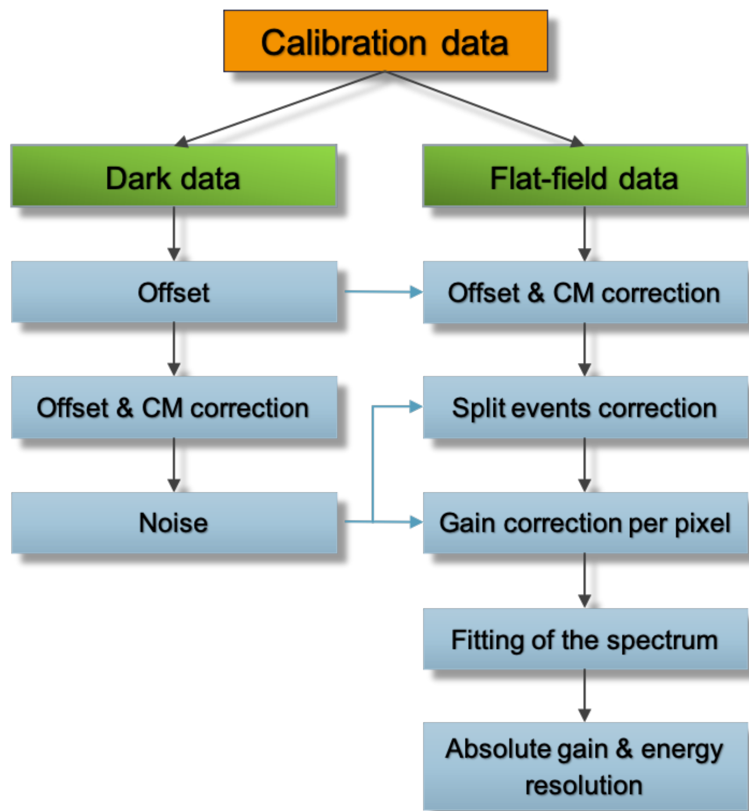

Figure 7.1: Flowchart illustrating the data correction and characterization steps applied to the dark and flat field data. Black arrows visualize the sequence of steps. Blue lines, on the other hand, are illustrating the results obtained from the dark data analysis that are needed as an input for the flat-field data characterization.

Chapter 8

The ePix100a Hybrid Pixel Detector

The ePix detector family developed at SLAC provides multiple variants of hybrid pixel detectors to support a wide range of applications at free-electron laser (FEL) facilities. The ePix detectors are by design a versatile and easy re-configurable camera system with common mechanical, electrical and data acquisition interfaces [69]. The ePix100a variant designed for low noise spectroscopy applications is used at two EuXFEL scientific instruments, namely HED and MID.

8.1 ePix100a Camera Description

The ePix100a is a backside illuminated low noise camera optimized for X-ray experiments requiring high spatial resolution and signal to noise ratio in the energy range between 2 keV and 18 keV [12].

The ePix100a detector module comprises four ASICs flip-chip bonded to a 500 μm thick silicon sensor with pixels of $50 \times 50\,\mu\text{m}^2$, the front-end electronics, the cooling system, its mechanics and housing. It is a 0.5 Mpixel camera with 704×768 pixels. A summary of the main ePix100a characteristics is given in Table 1.1.

The left panel of Figure 8.1 shows a schematic view of a vertical cross-section of the ePix sensor. The backside plane made from aluminium acts as the photon entrance window. The bulk of the sensor is made of p-doped high resistivity silicon with a phosphorus implanted backside (n^+) and a boron implantation at the side of the metal gates (p^+) to create a low resistance contact. Solder bump bonds provide a connection to the ASIC. The 500 μm thick sensor enables the detection of X-ray photons with energies between 3 keV and 13 keV with a quantum efficiency $\geq 80\,\%$ and at the same time efficiently shields the underlying ASIC from X-ray radiation. Due to its backside-illuminated design, sensor structures sensitive to

radiation-induced surface damage (e.g. Si/SiO_2 interfaces) are effectively shielded by the sensor in this energy range.

The ePix100a's ASIC provides signal processing and readout to an array of 352 pixels $\times$ 384 pixels. The dynamic range of the camera is equal to 220 ke^- which is equivalent to $\approx 100 \times 8$ keV photons per pixel. The ePix100a can be operated at a maximum frame rate of 240 Hz. At the EuXFEL, the camera is operated at 10 Hz (train repetition rate). Figure 8.2 shows a simplified schematic of the ePix100a pixel. A low noise charge sensitive pre-amplifier (CSA) with pulsed reset processes the analog signal provided by the sensor, which is subsequently low pass filtered. Next, a correlated double sampling (CDS) stage performs a baseline correction and noise reduction of the signal. Finally, the corrected signal is stored in a buffer. Further processing of the analog signal is organized in a column-parallel fashion. Each ASIC is divided into four banks. The analog output of the pixels of one bank accommodates 96 columns. Columns of each bank are multiplexed to a single analog output and subsequently digitized by an external sigma-delta ADC. Figure 8.1 on the right schematically illustrates a structure of the ePix100a readout. The analog output nodes are arranged on the top and bottom sides of the ASICs and sensor. For a detailed description of the ePix ASIC, detector design and a performance review, the reader is referred to Markovic et al. [11], Blaj et al. [12] and Nishimura et al. [69].

The ePix100a module under study was specifically dedicated to perform the radiation-induced damage study. The module has two ASICs with a good noise performance, one ASIC exhibiting significantly higher noise and one unresponsive ASIC. For the purpose of this study, only the two good ASICs were considered and evaluated. All detector components and structures are identical to the modules used for experimental applications at HED and MID. It is to note that the module under study is not expected or required to provide the scientific grade performance. as described earlier.

8.2 Characterization of the ePix100a Performance

To evaluate the ePix100a performance in terms of parameters described in chapter 6 we have taken sets of dark and flat-field data. Data analysis was done following the procedures described in chapter 7. In the following section, a detailed discussion of the ePix characterization and its results are given.

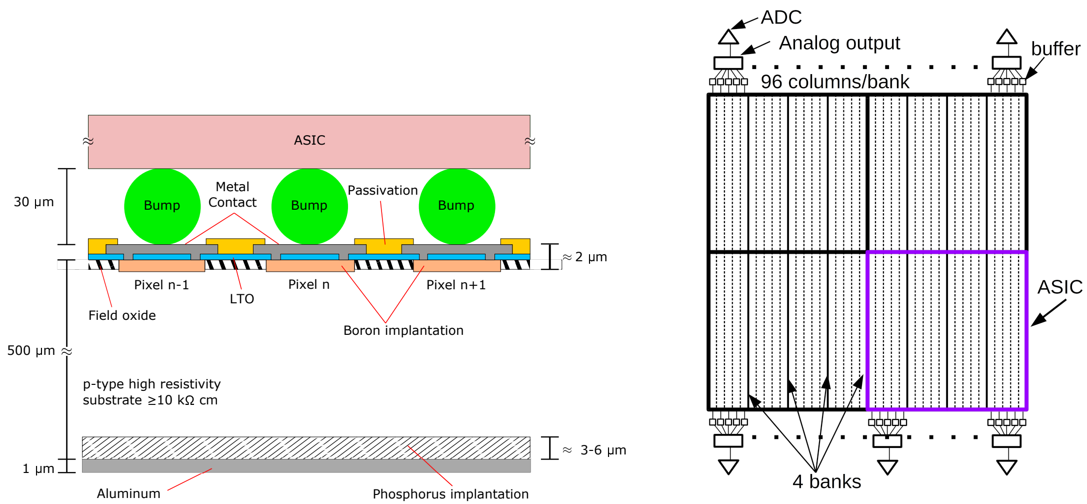

Figure 8.1: Left: Schematic view of the ePix100a sensor cross-section including interconnection bump bonds and the readout ASIC (kindly provided by M. Kuster). The sensor is illuminated from the backside, i.e. from the bottom. Right: Schematic drawing of the ePix100a sensor showing the arrangement of the 4 ASICs required to read out one sensor section with a size of 352 pixels × 384 pixels pixels. Each ASIC is divided into four banks accommodating 96 columns multiplexed to a single analog output digitized by an external ADC.

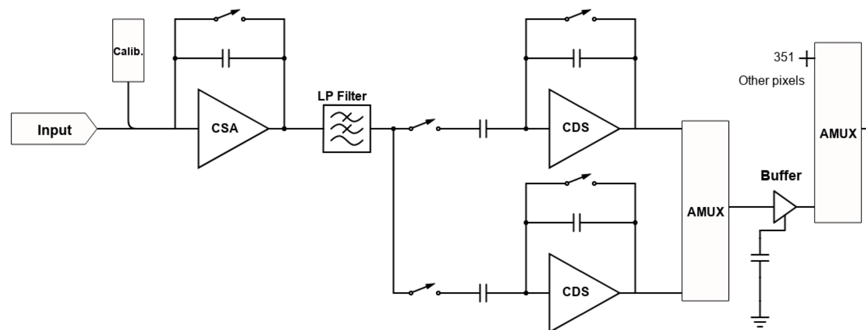

Figure 8.2: Simplified schematic of the ePix100a pixel.

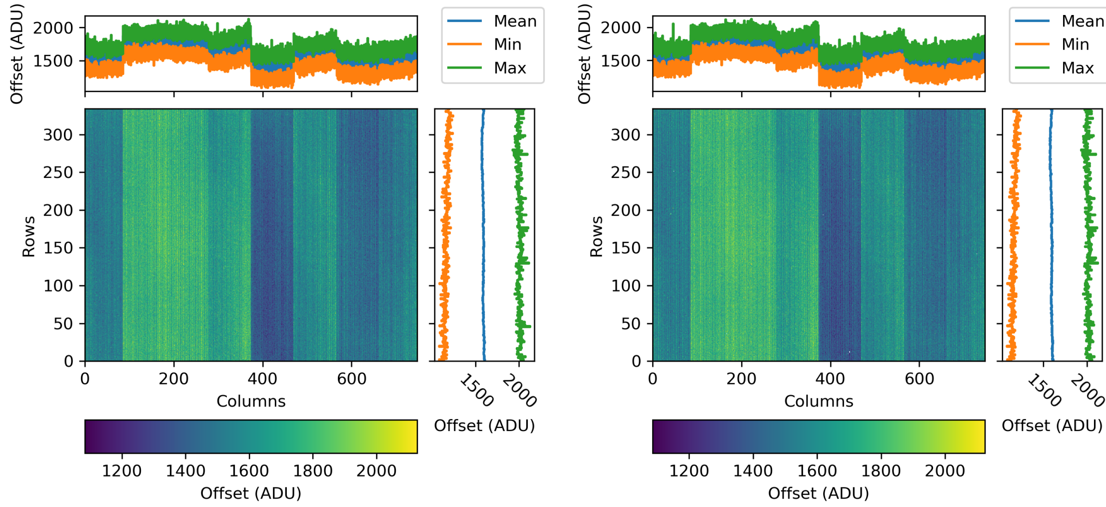

Figure 8.3: Offset maps of the ePix100a resulting from dark data taken at $t_{\mathrm{Int}} = 50\,\mu$s shown on the left and at $t_{\mathrm{Int}} = 800\,\mu$s shown on the right. Top and side panels on both plots show the offset along columns, respectively rows.

8.2.1 Dark Signal Characterization

Characterization measurements were performed under vacuum conditions and at -9 °C to suppress thermal charge generation and with two different integration times, i.e. $50\,\mu$s and $800\,\mu$s. The integration time of $t_{\mathrm{Int}} = 800\,\mu$s was selected due to the higher sensitivity even to small changes in the leakage current induced by the radiation damage, while $t_{\mathrm{Int}} = 50\,\mu$s corresponds to a typical integration time used at HED.

Figure 8.3 shows offset maps calculated for the two integrations times. The panel on the left corresponds to the offset measured at $t_{\mathrm{Int}} = 50\,\mu$s, while the offset map for $t_{\mathrm{Int}} = 800\,\mu$s is shown on the right. The block structure visible in both maps is due to the ASIC readout design as previously described in section 8.1. The spatial offset distribution is comparable for both integration times. The mean value of the offset across two ASICs at $t_{\mathrm{Int}} = 50\,\mu$s is (1589 ± 173) ADU and for $t_{\mathrm{Int}} = 800\,\mu$s we measure (1595 ± 174) ADU. Following the analysis steps, as shown in Figure 7.1, dark data have to be corrected for the common mode. As stated by Blaj et al. [12], the common mode of the ePix100a is induced from the interference of the signals due to the external (off ASIC) digitization. A common mode correction was applied to the data to reduce the influence of common mode noise on the subsequent analysis in three steps:

1. Common mode correction per ASIC

2. Common mode correction per column

3. Common mode correction per row

Figure 8.4 shows the influence of the common mode correction on the dark data. Starting from the top left, the dark image after offset subtraction and before common mode correction is shown. Stripe-like patterns are visible in both row- and column-direction. The difference between the left and right ASIC is also observable. The relative difference of offset-corrected signal variation between the two ASICs is about 7%. Applying CM correction per block of the ASIC yields signal distribution visualized in the top right plot. The difference between the two ASICs reduces to 4%.

Further, correction of common mode per column is applied, removing the vertical noise patterns as shown in the bottom left plot. Finally, a common mode correction to remove the additional signal variation along rows is performed. The fully common mode corrected dark image is shown in the bottom right plot of Figure 8.4.

The left plot of Figure 8.5 shows a histogram of the offset corrected data at different levels of the CM correction; blue line for the dark offset corrected signal, orange line for the dark offset corrected signal with CM correction per ASIC (denoted with B for "block") and green line for the CM correction applied per ASIC, column and row (marked as B+C+R). As can be seen, the peak is narrowing down, and the common mode correction helped decrease its width by $\approx 30\%$.

After the common mode correction has been performed, the noise calculation follows. The spatial distribution of the noise on the sensor can be seen in Figure 8.6 for $t_{\mathrm{Int}} = 50\,\mu$s on the left panel and for $t_{\mathrm{Int}} = 800\,\mu$s on the right panel. The bank structure of the two ASICs is also recognizable in the noise map, with two banks exhibiting a slightly higher noise in comparison to the rest of the banks. The bank on the left ASIC has an RMS noise higher by $1.7\,\mathrm{e}^-$ in comparison to the overall RMS noise of $40.2\,\mathrm{e}^-$ and the bank on the right ASIC by $7.7\,\mathrm{e}^-$.

Moreover, a cloudy noise feature becomes dominant with higher integration time. As the history of the sensor and the readout-ASICs is unknown to the author of this thesis, the origin of the cloudy feature remains unclear. For the radiation damage experiment, we have selected a region with good and homogeneous noise performance to minimize the impact of the cloudy feature, referred to as the region of interest (ROI).

The RMS noise measured at $t_{\mathrm{Int}} = 50\,\mu$s amounts to $40.2\,\mathrm{e}^-$ and for $t_{\mathrm{Int}} = 800\,\mu$s we observe an RMS noise of $48.4\,\mathrm{e}^-$, which is approximately $1.2\times$ higher noise in

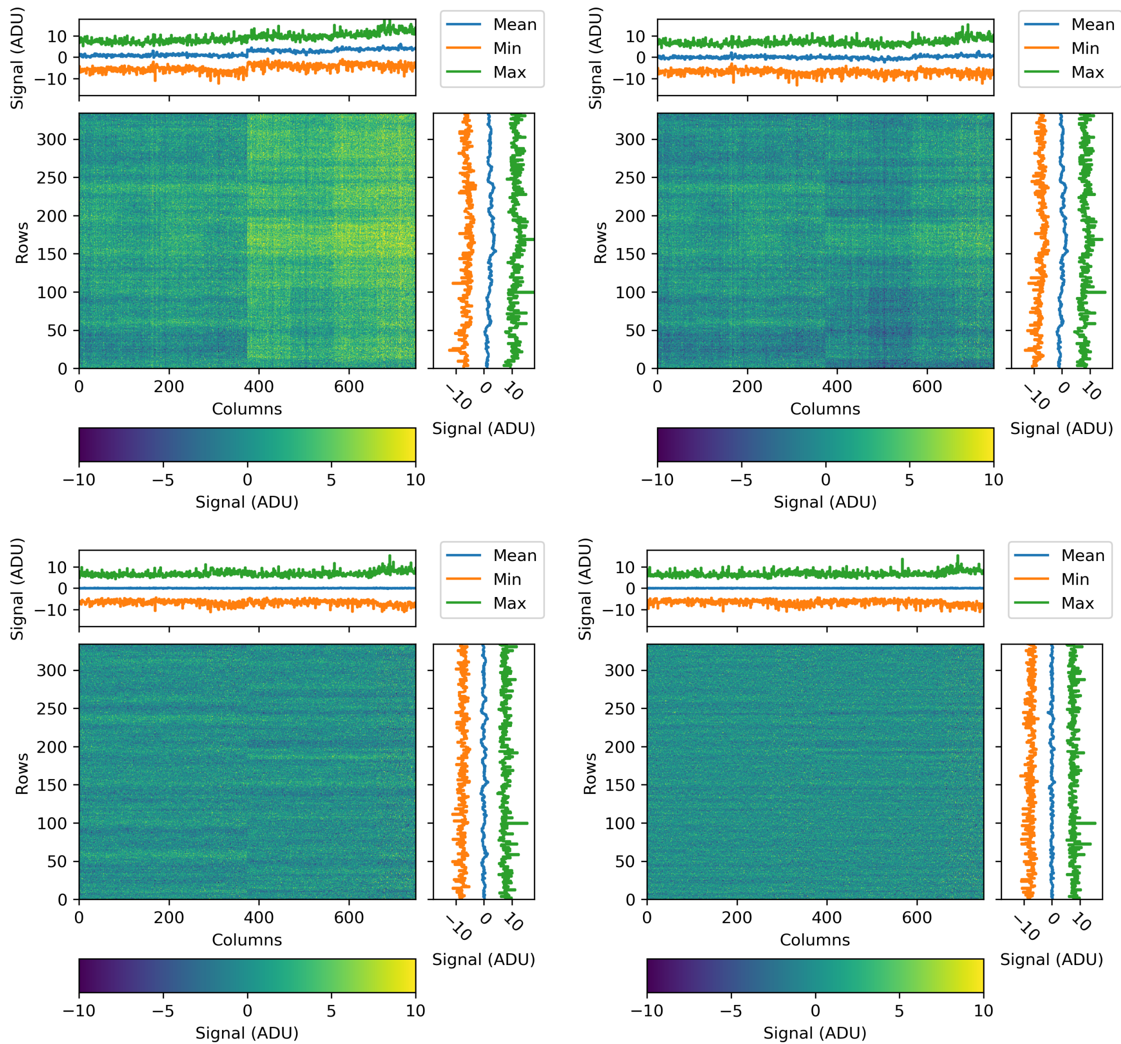

Figure 8.4: Effect of different stages of a common mode correction on the spatial distribution of the offset corrected dark signal. The top left plot shows the offset corrected dark image before CM correction, the top right plot shows the same dark image after the common mode correction per ASIC. The bottom left plot shows the image after applying the ASIC CM correction and correction for columns. The last image on the bottom right shows the image after applying ASIC, column and row wise CM correction.

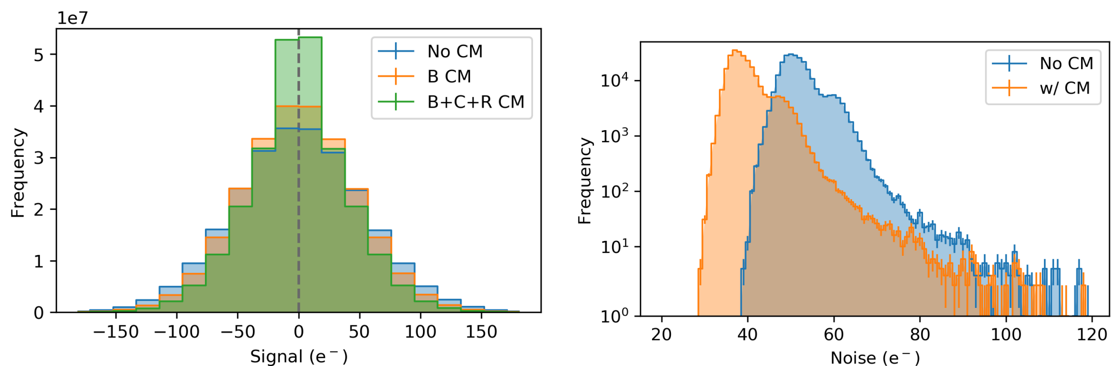

Figure 8.5: Left plot: Histogram of the offset subtracted dark signal at different stages of common mode correction. Blue line - before CM correction, orange line - CM correction per ASIC block (B), green line - CM correction per ASIC, column and row (B+C+R). Right plot: Effect of the common mode correction on the noise. A shift of the noise distribution to lower values after performing common mode correction is apparent.

comparison to the noise at $t_{\mathrm{Int}} = 50\,\mu\mathrm{s}$.

As shown later, the noise is expected to scale linearly with integration time if the primary source of noise is a leakage current, i.e. with a factor of $800\,\mu\mathrm{s}/50\,\mu\mathrm{s} = 16$. However, we observe only an increase by a factor of 1.2. Hence, the contribution of the leakage current is negligible. Since the sensor is cooled to $-9\,^{\circ}\mathrm{C}$, the main contributor is the noise from the readout electronics.

Reduction of the noise after performing the common mode correction is visualized in the right panel of Figure 8.5. The RMS noise after common mode correction decreases from $52.7\,\mathrm{e}^-$ to $40.2\,\mathrm{e}^-$, which is an improvement by 30%. Histograms of the offset (left) and noise (right) for both integration times are shown in Figure 8.7.

Offset (top left $t_{\mathrm{Int}} = 50\,\mu\mathrm{s}$, top right $t_{\mathrm{Int}} = 800\,\mu\mathrm{s}$) and noise maps (bottom left $t_{\mathrm{Int}} = 50\,\mu\mathrm{s}$, bottom right $t_{\mathrm{Int}} = 800\,\mu\mathrm{s}$) of the area selected for the radiation damage experiment to be irradiated with a direct beam are shown in Figure 8.8. The average offset found in the ROI is (1755 ± 113) ADU at $t_{\mathrm{Int}} = 50\,\mu\mathrm{s}$ and at $t_{\mathrm{Int}} = 800\,\mu\mathrm{s}$ we found the offset of (1762 ± 113) ADU. The RMS noise of the selected region amounts to $37.8\,\mathrm{e}^-$ at $t_{\mathrm{Int}} = 50\,\mu\mathrm{s}$, respectively to $47.1\,\mathrm{e}^-$ ($t_{\mathrm{Int}} = 800\,\mu\mathrm{s}$).

8.2.2 Gain Calibration and Performance under Illumination

To characterize the gain and the detector's energy resolution, flat-field data was acquired by homogeneously illuminating the ePix100a sensor with Cu fluorescence

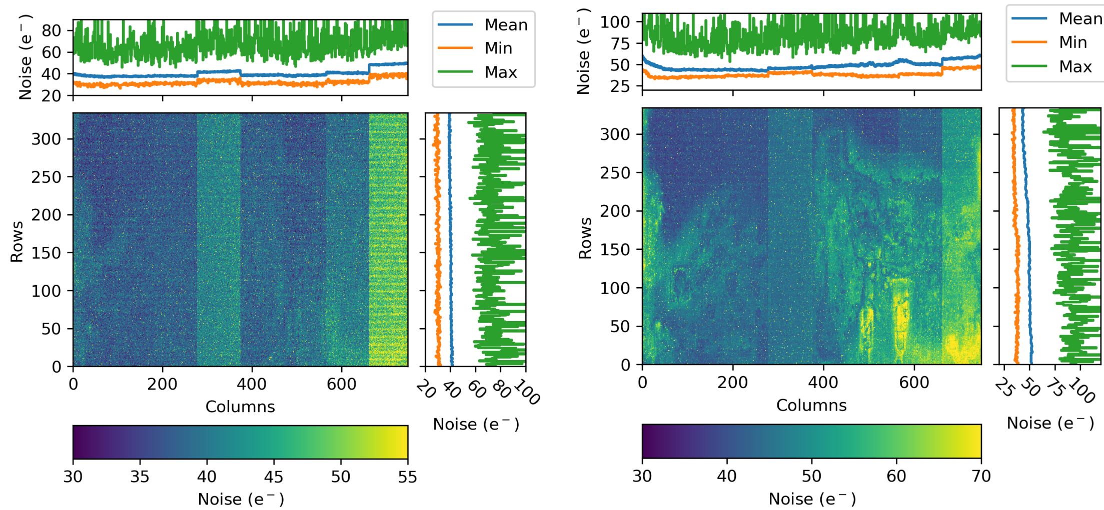

Figure 8.6: Noise maps of the ePix100a resulting from dark data taken at $t_{\mathrm{Int}} = 50\,\mu$s shown on the left and at $t_{\mathrm{Int}} = 800\,\mu$s shown on the right.

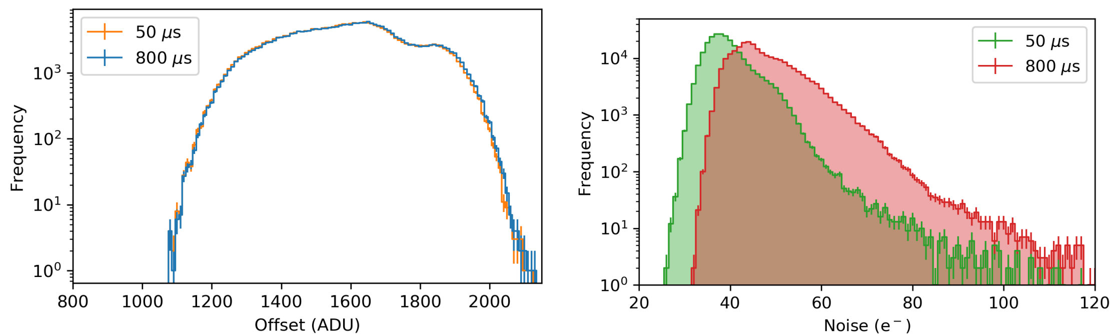

Figure 8.7: Histograms of the offset (left) as measured at $t_{\mathrm{Int}} = 50\,\mu$s (orange line) and at $t_{\mathrm{Int}} = 800\,\mu$s (blue line). The right plot shows the noise at the same integrations time, i.e. at $t_{\mathrm{Int}} = 50\,\mu$s (green line) and at $t_{\mathrm{Int}} = 800\,\mu$s (red line).

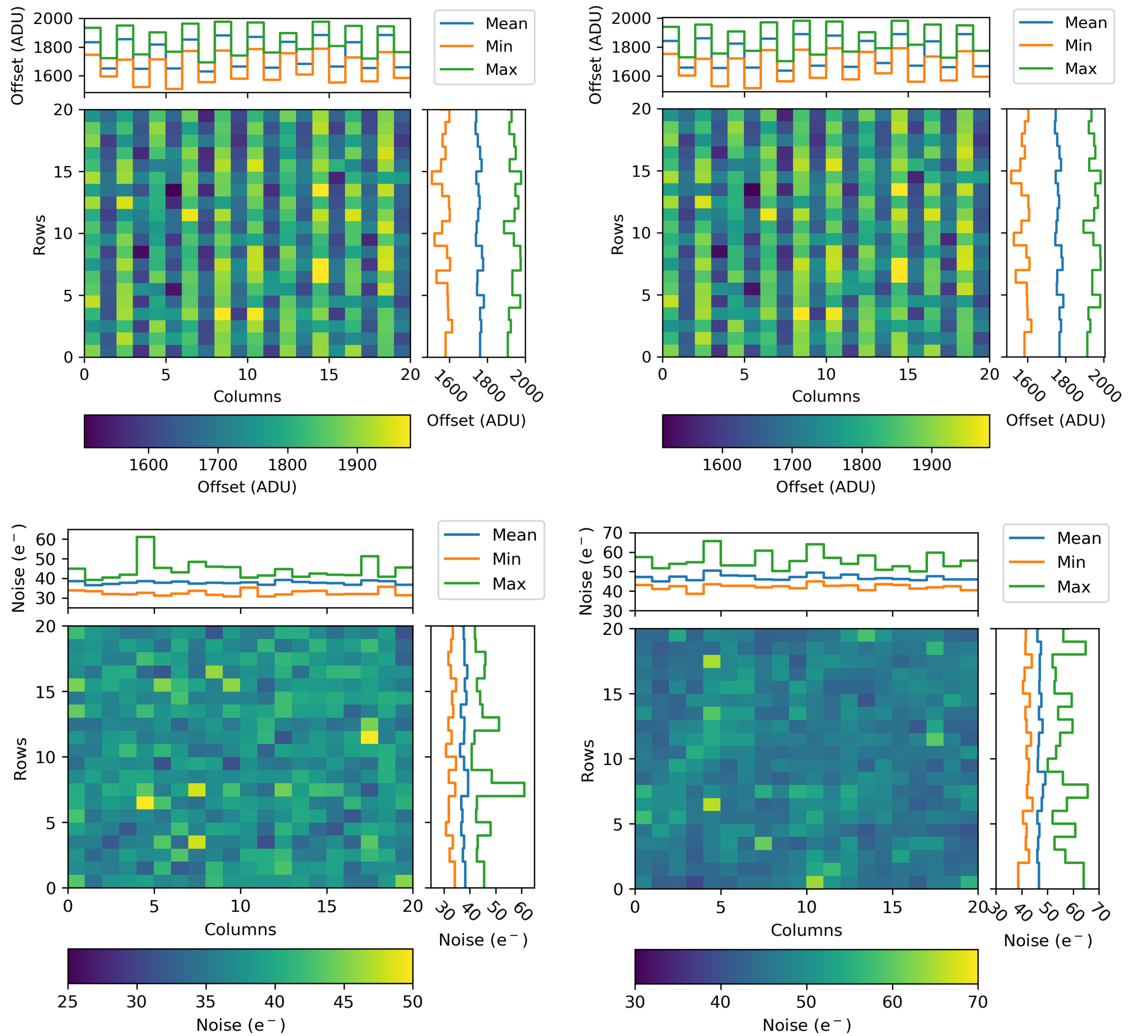

Figure 8.8: Offset and noise maps of a 20 pixels × 20 pixels sensor area selected for irradiation with the direct beam. Top plots visualize the offset measured at $t_{\text{Int}} = 50\,\mu\text{s}$ on the left and at $t_{\text{Int}} = 800\,\mu\text{s}$ on the right. Bottom plots show the noise measured with the same integration times.

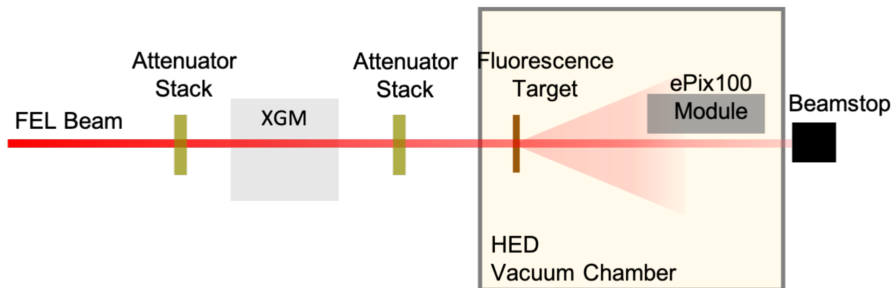

Figure 8.9: Setup used for calibration measurements of the ePix100a. The attenuated beam is directed onto a Cu target. The ePix100a module is moved off-axis to avoid contact with the direct beam. In addition to the Cu fluorescence's photons, the FEL beam (see figure 8.13) was detected due to the placement of the detector in transmission geometry.

photons resulting from the FEL beam impinging a Cu target. The energy of Cu fluorescence photons is $E_{\mathrm{K}\alpha_1} = 8047.78\,\mathrm{eV}$ and $E_{\mathrm{K}\alpha_2} = 8027.83\,\mathrm{eV}$. As can be seen in Figure 8.9, the detector was placed at an angle of 90° with respect to the beam, slightly shifted off the beam axis, and a Cu target was installed in a transmission geometry. This detection geometry yielded a detector illumination with additional 9 keV photons originating in the FEL beam due to scattering of the beam on the target material (see section 2.2).

In accordance the data processing steps described in chapter 7, the collected flat-field data are offset and common mode corrected. Afterwards, charge sharing is evaluated and corrected for, and single-pixel events are used for the following characterization steps. The spectrum of single-pixel events (singles) measured with the ePix detector is shown in Figure 8.10. The energetic proximity of the two Kα lines makes them indistinguishable in measurements with the ePix100a. Instead, we observe a blend of lines with an average energy of 8037.81 eV. The spectrum also contains peaks resulting from multiple photon hits incident on a pixel within one integration cycle (peaks to the right of the main photo-peak).

Gain calibration was performed in two steps: first, the data were corrected for relative gain. The absolute gain (conversion factor between digital and energy units) was subsequently determined from the resulting spectra. The relative gain is calculated from single-pixel events, with a signal above $6\,\sigma$ noise threshold in a given pixel. A relative gain map calculated from the Cu fluorescence single-pixel hits is shown in Figure 8.11 on the left, and the zoom into the region of interest during direct beam irradiation is on the right. The gain variation between pixels is $\approx 4.2\,\%$.

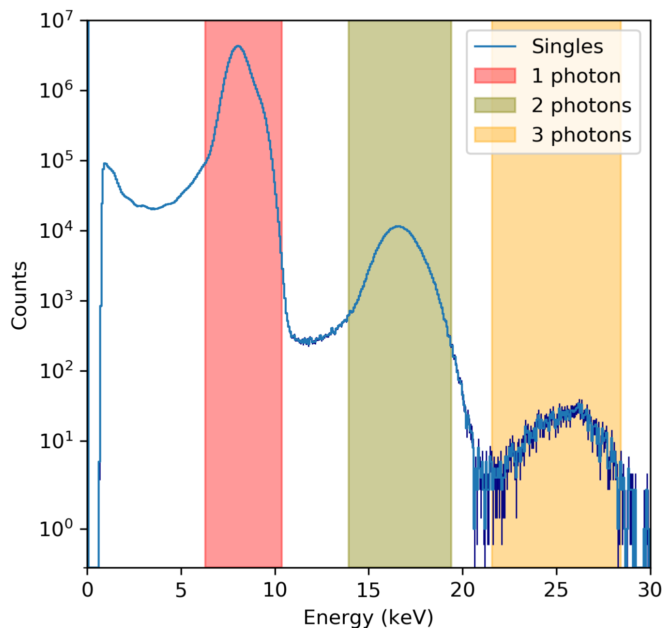

Figure 8.10: Cu-K fluorescence spectrum of photons interacting with single pixels. The spectrum consists of Cu-Kα line blend of 8.037 keV and the 9 keV line resulting from photons of the primary FEL beam (red region), visible as a shoulder on the right side of Cu-K line and lines due to multiple photon hits during one integration window. Peaks resulting from multiple photon hits are marked by the green region (2 photons) and by yellow region (3 photons). Note: The plotted error bars are smaller than the symbol size.

Before the relative gain correction, the 9 keV line is present only as a bump on the Cu-K line blend, without clear separation between the two. The relative gain correction narrows the peaks in the spectrum, thus making the Cu-K and 9 keV line more pronounced (see Figure 8.12). The pixel-to-pixel differences reduce to 0.3% on average.

The absolute detector gain is calculated from a corrected spectrum by determining the positions of the observed lines employing a Gaussian model. In our scenario, I have used three Gaussian lines; two lines to model the Cu-K line and 9 keV line and the third one to compensate for the low energy shoulder of the Cu-K peak due to incorrectly reconstructed events. The incorrect event reconstruction arises when the split charge in the adjacent pixels is not high enough to overcome the secondary threshold. Each of the Gaussian lines is of the form of:

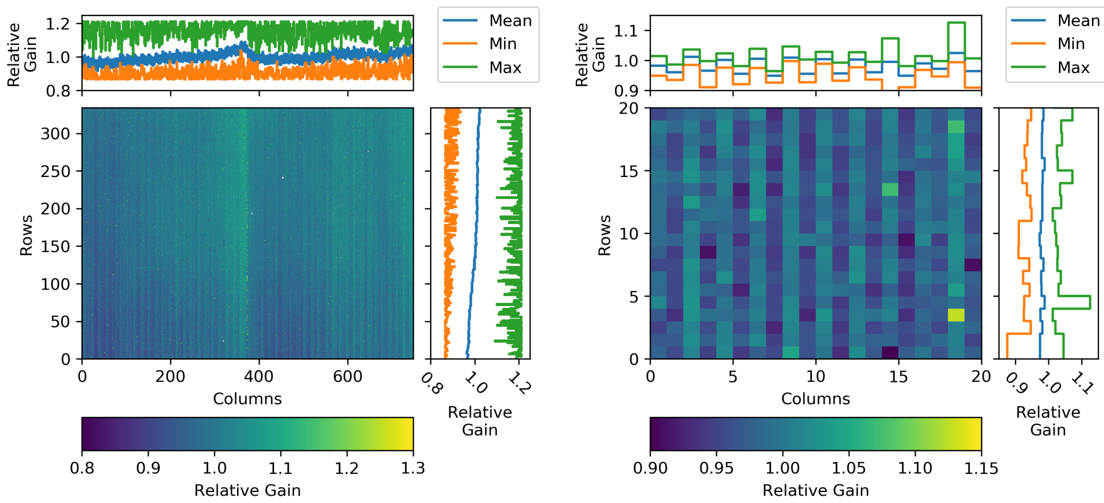

Figure 8.11: Left panel: Relative gain map of the ePix100a used to correct the collected data for pixel-to-pixel variation of the characteristics of the pre-amplifiers present in each pixel. Right panel: Relative gain of the 20 pixels × 20 pixels large ROI.

$$f(x) = A \exp\left(-\frac{(x-\mu)^2}{2\sigma^2}\right), \tag{8.1}$$

where A is the amplitude of the observed line, μ represents the line's position and σ being the standard deviation of the line. The best-fit Gaussian model with its components is shown in Figure 8.13 on the left.

In the next step, the determined position of the Cu-K line and the 9 keV line are plotted against the expected energy. The absolute gain is then represented by the slope of the linear fit of the data. The absolute gain of the ePix100a was calculated to be $g = (69.6 \pm 0.5)$ eV/ADU. The calibrated spectrum is shown in Figure 8.13, where also the expected and measured peak positions are denoted, showing very good agreement between the two with the difference being $< 0.5\%$.

The same procedure has been performed for the region of interest selected for the irradiation experiment. Here we find the absolute gain of (70.1 ± 0.5) eV/ADU. This value is consistent with the global gain uncertainties.

8.2.3 Signal to Noise Ratio, Dynamic Range and Energy Resolution

As presented earlier, the noise level of the non-irradiated ASIC is $\sigma = 147$ eV RMS for the integration time of 50 μs. The signal to noise ratio (SNR) for the Cu-K

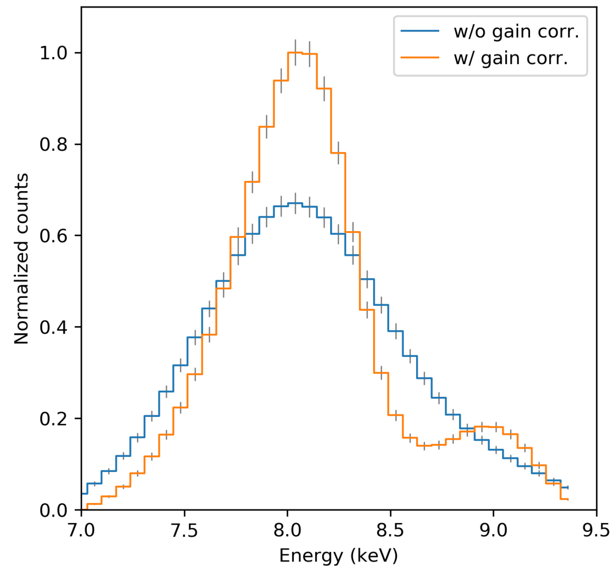

Figure 8.12: Comparison between uncorrected single pixel hit spectrum (blue line) and spectrum corrected for relative gain (orange line). The Cu-Kα line blend and 9 keV line become clearly distinguishable.

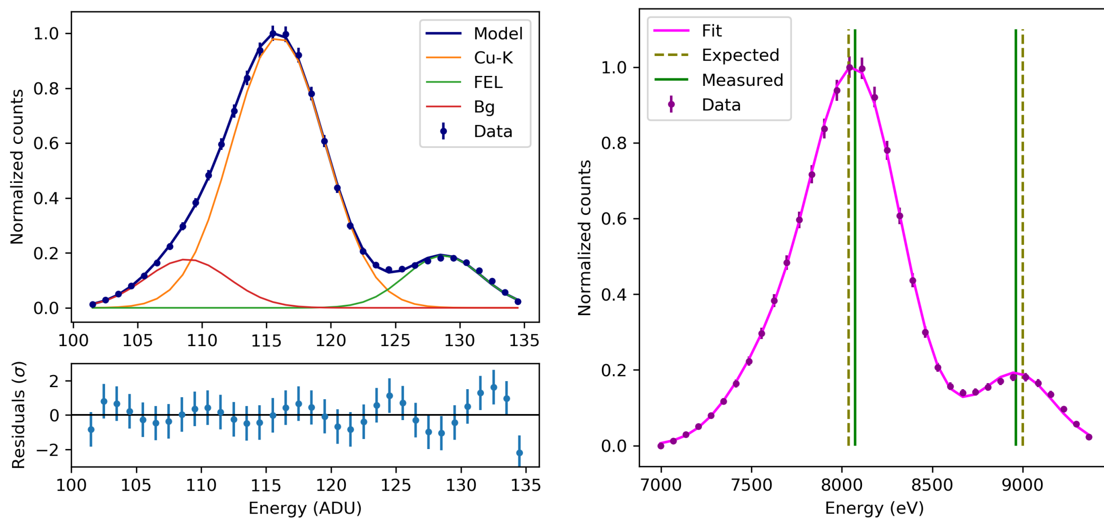

Figure 8.13: Left: The Gaussian model applied to the measured data to determine the position of the lines and their widths. Right: Calibrated spectrum of single-pixel events showing Cu-Kα line average at 8.037 keV and primary beam at 9 keV. Measured (solid green lines) and expected (dashed green lines) energy peaks show good agreement.

fluorescence hence amounts to 55.

The dynamic range as presented in section 6.2 can be given as n number of photons that the ePix100a can resolve instead of ADU values. The ePix100a dynamic range is specified for 8 keV photons, so the same notation is followed here. Using the already determined absolute gain to convert between energy and digital units for the dynamic range, we get 128×8 keV photons.

The energy resolution derived from the Gaussian model applied to the data was found to be (594 ± 43) eV FWHM, while for the ROI, we determined an energy resolution of (641 ± 45) eV. The two FWHM values are compatible within the given uncertainties. Following equation 6.10, we can calculate the expected energy resolution if the measured photo-peak is Fano noise driven. For the calculated energy resolution of the Cu-K line blend across two ASICs, we get 698 eV, while for the ROI, we get an energy resolution of 656 eV. These results suggest the measured energy resolution follows the theoretical value derived from the Fano noise relation and the measured noise, confirming that the photo-peak is Fano-driven.

A summary of all the ePix100a characterized parameters presented in this section is given in Table 8.1.

Table 8.1: Summary of the performance characteristics of the ePix100a detector.

Parameter	$\mathbf{t_{Int}}$	**2 ASICs**	**ROI**
Mean offset (ADU)	50	1589 ± 173	1755 ± 113
	800	1595 ± 174	1762 ± 113
RMS noise (e^-)	50	40.2	37.8
	800	48.4	47.1
Gain (ev/ADU)	50/800	69.6 ± 0.5	70.1 ± 0.5
Dynamic range ($n \times 8$ keV)	50/800	128	128
Energy resolution (eV)	50	594 ± 43	641 ± 45

Chapter 9

Radiation Damage of the ePix100a Detector

The ePix100a plays a key role in the experimental program of the HED instrument. Hence its good scientific performance is essential. The detector is required to provide low noise, i.e. $< 80\,e^{-}$RMS and a peak-to-noise separation $\geq 5\,\sigma$ @ $5\,$keV, thus an radiation-induced noise increase is an important parameter to observe and evaluate closely. Another important parameter is the detector's dynamic range, as its significant reduction will lead to a decreased capability to resolve high-intensity signals.

Understanding the effects of radiation-induced damage on the detector's performance and assessing the detector's lifetime is essential to ensure reliable scientific operation (based on the parameters described above and in chapter 6). It is important to provide a time frame for damage compensation measures to take place in terms of re-calibration, repair or module exchange. In the following chapter, a radiation damage study of the ePix100a will be discussed.

9.1 Motivation for the Radiation Damage Studies of the ePix100a

As discussed in section 1.2, detectors have been specifically designed and built for the needs of the European XFEL. Since high radiation tolerance is one of the requirements for these detectors, the AGIPD detector, together with the LPD detector, have been optimized to incorporate a higher level of radiation hardness into their design. Thorough studies of the influence of X-ray radiation on silicon sensors have

been conducted during the design and development phase of the first generation of these detectors.

At the time of the AGIPD development, no previous studies were addressing highly irradiated silicon sensors by X-rays of the EuXFEL energies. Results by Zhang et al. [70, 71, 72] give insight on the parameters determining the damage depending on the induced dose and their influence on the operation of various types of silicon sensor designs. These studies provided valuable knowledge to design and optimize the sensor parameters as reported by Schwandt et al. [73, 74]. An overview of the AGIPD design challenges and development strategy is given by Klanner et al.[75].

The radiation hardness studies performed for the LPD detector [76] aimed to investigate X-ray radiation damage on different components of the detector assembly, e.g. sensor, ASIC, ASIC memory or bias circuitry. The observations led to an optimization of the assembly layers and to the addition of extra shielding for the most sensitive parts of the detector assembly, e.g. ASIC memory.

Other detectors, not explicitly built for but used at the EuXFEL, were also examined for their radiation hardness and exhibit a certain level of radiation tolerance, e.g. the JUNGFRAU [77] detector.

The studies cited above provide helpful knowledge and valuable observations for the here presented experiment results.

9.2 Experiment Setup

The ePix100a radiation damage experiment conducted at the HED was designed to investigate effects induced by irradiation with the FEL beam. The detector was irradiated with a direct attenuated beam. We have used a beam with a photon energy of 9 keV, corresponding to the commonly used energy at the HED instrument. The full beam energy of the EuXFEL is of the order of mJ. Exposing the detector to the direct beam would cause instantaneous and permanent damage to the detector hardware. We have attenuated the beam below the immediate damage threshold with a configurable stack of Chemical Vapour Deposition (CVD) diamond and Si foils of various thicknesses to avoid the mentioned scenario. An X-ray Gas Monitor (XGM) was continuously monitoring the beam intensity. The XGMs are designed to perform a non-invasive measurement of the X-ray pulse energy with an absolute accuracy of $7\% - 10\%$. A detailed description of the XGM is provided by Sorokin et al. [78], and performance details and an overview of usage scenarios at the EuXFEL

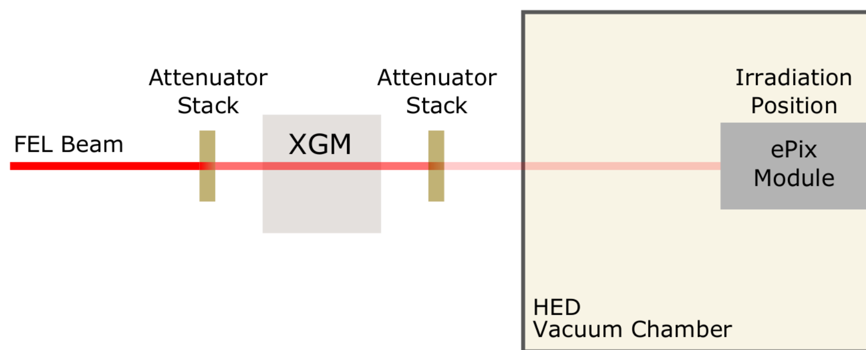

Figure 9.1: Experimental setup used to irradiate the ePix100a detector with the direct beam at the HED instrument (kindly provided by M. Kuster). The primary beam intensity is attenuated by two stacks of absorbers located before and after the X-ray Gas Monitor.

are given by Maltezopoulos et al. [79].

Throughout the course of the experiment, we have operated the detector under vacuum at a pressure of 1×10^{-5} mbar, cooled to $-9\,°\mathrm{C}$ and biased with 200 V. The beam spot area was approximately $1\,\mathrm{mm}^2$, covering an area of $\approx 20\,\mathrm{pixels} \times 20\,\mathrm{pixels}$ of the ePix100a sensor. The beam spot was placed in the area having the lowest pre-irradiation noise as explained earlier in section 8.2. The placement of the irradiation spot on the sensor is shown in Figure 9.2. A summary of the FEL beam settings and detector parameters is given in Table 9.1. The experiment setup used to irradiated the ePix100a with the direct FEL beam is schematically shown in Figure 9.1.

9.3 Experiment Methodology

We have performed the ePix100a irradiation in cycles. Each irradiation cycle consisted of a 20 minutes exposure with a direct FEL beam, followed by dark image measurements with $50\,\mu$s and $800\,\mu$s long integration times. We used the dark measurements to monitor the state of the detector module after each irradiation cycle. We have irradiated the sensor with a dose rate of approximately $180\,\mathrm{kGy/mm^2h}$ at the Si/SiO_2 interfaces in the sensor. In total, we repeated the irradiation cycles 15 times during the course of the study. The sequence of individual steps during the experiment is shown in Figure 9.3.

The experiment further involved calibration data taking prior to and after irradiation to evaluate the performance evolution of the detector. The taken calibration

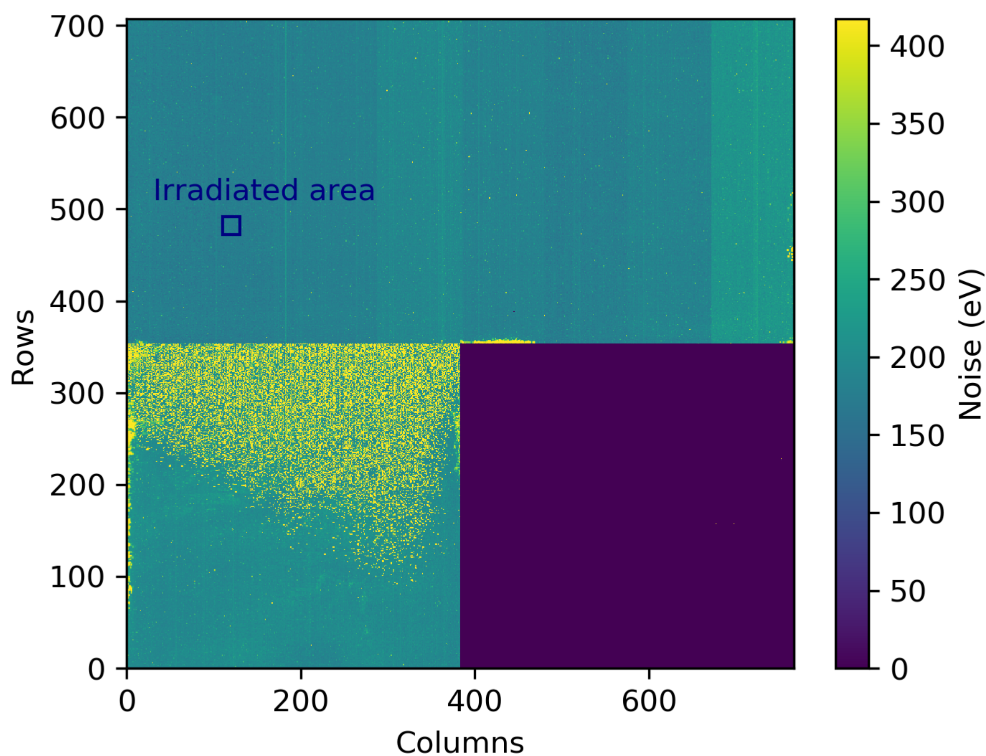

Figure 9.2: The noise map of the ePix100a measured at $t_{\mathrm{Int}} = 50\,\mu$s, visualizing placement and size of the area irradiated by the FEL beam (blue square). The bottom left ASIC exhibits a higher noise level than the two ASICs located on the top. The ASIC on the bottom right does not provide any data.

Table 9.1: Summary of the relevant beamline and detector operation parameters as used during the irradiation experiment.

Beam parameters	
Average beam energy at the detector	10 nJ/Pulse
Photon energy	9 keV
Number of X-ray pulses per train	100 Pulses
Dose rate at the Si/SiO_2 interfaces	180 kGy/h
Beam intensity monitoring	XGMs at HED beamline
Detector parameters	
Pixel size	$50\,\mu m \times 50\,\mu m$
Sensor size	704 pixels × 768 pixels
Sensor thickness	$500\,\mu m$
Irradiated sensor area	20 pixels × 20 pixels ($1\,mm^2$)
Full well capacity	$220\,ke^-$
Frame rate	10 Hz
Integration time	$50\,\mu s$ and $800\,\mu s$
Bias voltage	200 V
Sensor temperature	$-9°$ C
Environment	Vacuum, $p \leq 1 \times 10^{-5}$ mbar

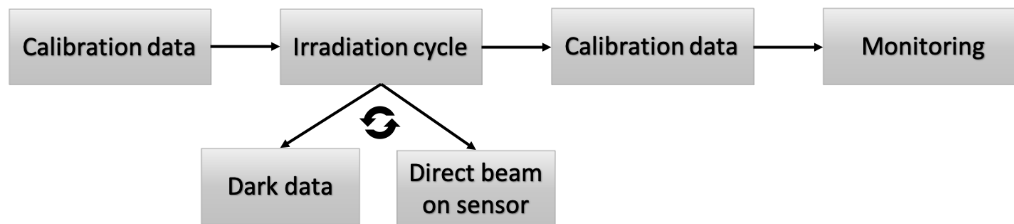

Figure 9.3: Flowchart illustrating individual steps of the irradiation experiment to study radiation-induced damage of the ePix100a detector.

data consists of flat-field measurements using Cu-K fluorescence photons resulting from the irradiation of a 50 μm thick Cu target, taken at 50 μs integration time.

9.4 Dose Evaluation

As stated above, the intensity of the beam was measured by an XGM. However, the XGM measurement does not provide information about the spatial distribution of the beam intensity on the ePix's sensor. In order to determine the intensity profile of the beam, we have performed measurements of the beam profile at low X-ray intensities with the ePix100a detector. These measurements provided us information on the spatially resolved distribution of the beam intensity on the ePix100a sensor.

As explained in section 1.1, the generation of the FEL beam results in the production of harmonic lines of higher energies. In our case, the beam profile contained the fundamental beam energy of 9 keV, and a significant contribution of the third harmonic at 27 keV.

We have measured the beam profile for various attenuation levels of the absorbents to determine the beam's profile more precisely. As the desired attenuation is calculated and optimized for the fundamental energy, higher harmonic energies are attenuated only weakly. Using very high attenuation levels, such that the beam intensity is reduced by 12 orders of magnitude, almost completely suppressing the fundamental beam, allows measuring third harmonic contribution.

The contribution of the third harmonic can be seen in Figure 9.4 on the left. By decreasing the attenuation by two orders of magnitude and subtracting the third harmonic measurement from the measurement with fundamental beam not suppressed, a clear profile of the 9 keV can be obtained as shown on the right of Figure 9.4.

Irradiating the detector with a high beam energy of $\gtrapprox 65$ pJ led to saturation of the signal. Pixels located in the core of the beam became unresponsive during

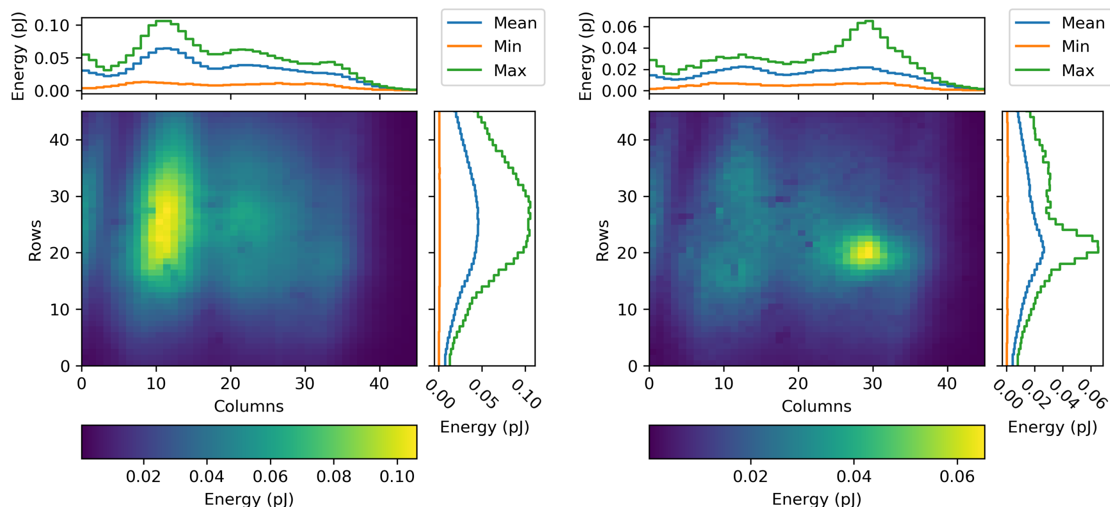

Figure 9.4: Left: Average beam energy observed with the highly attenuated 9 keV beam showing a contribution of the third harmonic at 27 keV. Right: The beam profile of the 9 keV beam after subtraction of the third harmonic contribution (shown on the left side).

the time of irradiation. The size of the resulting unresponsive area is approximately equal to the size of the ROI, i.e. 20 pixel × 20 pixels. This effect is discussed more closely in section 9.5. Here, the importance of the observed effect lies in the possibility to monitor the position of the beam during each irradiation cycle on the ePix100a sensor, thus allowing for a more precise calculation of the per-pixel dose.

The data processing steps performed to calculate the total absorbed per-pixel dose are shown in Figure 9.5. The procedure starts with the evaluation of the position of the inactive pixel area. The Canny edge detection algorithm [80] is employed to detect the edges of the inactive area and assigns a circle to it. The detected circle's centre is assumed to be the beam core's centre. The left panel of Figure 9.6 shows an exemplary result of the inactive area detection. The inactive area is marked with light blue dots, and the white cross corresponds to its centre. Based on the detected circular area, a proportional per-pixel beam distribution $F_{x,y}$ is applied, calculated as

$$F_{x,y} = \frac{E_{\mathrm{B}_{x,y}}}{\sum E_{\mathrm{B}_{x,y}}}, \tag{9.1}$$

where $E_{\mathrm{B}_{x,y}}$ is the beam energy deposited in a given pixel. The pixel with the highest value from the proportional beam distribution is identified as the circle's centre. In the next step, the XGM intensity is converted to photon count numbers N_{ph} and

distributed into the inactive area based on the given proportionality. This procedure is repeated for every image taken during irradiation. The result is the number of photons delivered to a given pixel denoted as photon intake $C_{\mathrm{ph}_{x,y}}$

$$C_{\mathrm{ph}_{x,y}} = \sum_{z=0}^{n-1} (N_{\mathrm{ph}_z} \cdot F_{x,y}). \tag{9.2}$$

The total per-pixel photon intake can be seen in figure 9.6 on the right.

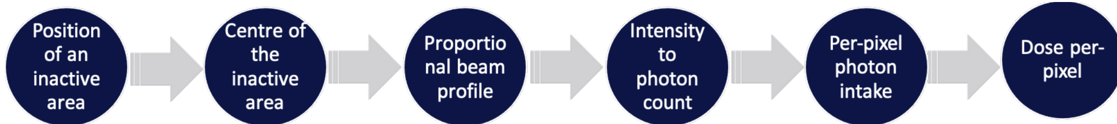

Figure 9.5: Flowchart of the analysis steps to calculate the per-pixel intake of the incoming photons throughout the course of the irradiation experiment.

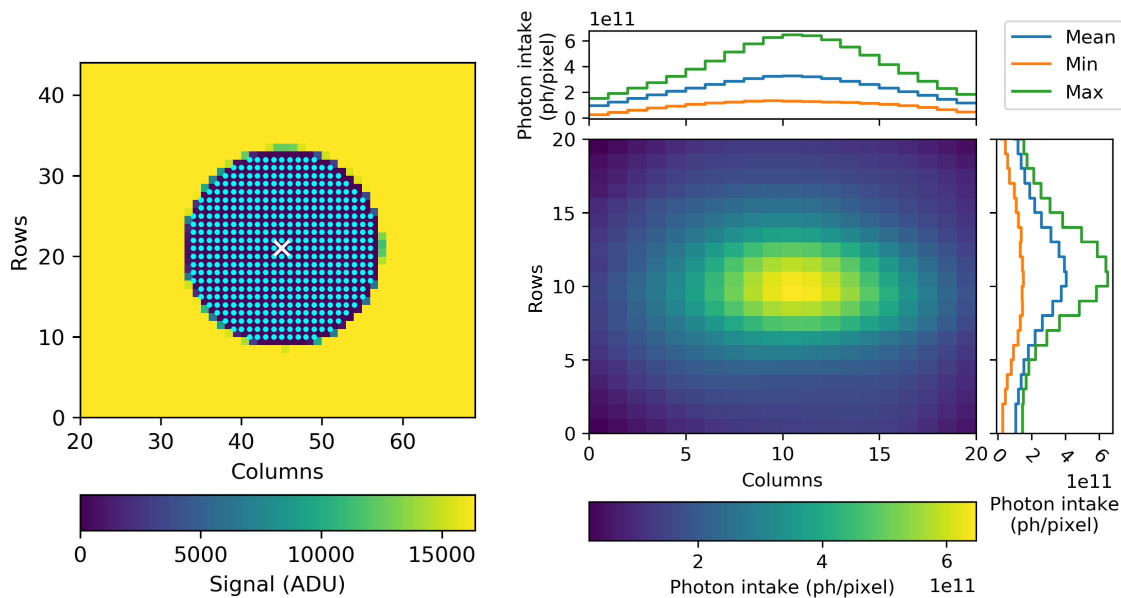

Figure 9.6: Left: The inactive region detected for one image frame. The light blue colour marks the circular area used to determine the centre (marked with white cross). Right: Per-pixel photon intake (photons/pixel) calculated for all irradiation runs.

To estimate the absorbed dose, the MULASSIS tool [81] was used to simulate the dose at different depths of the ePix100a sensor. It is a Geant4 based Monte Carlo simulation tool used to analyse particle fluence and dose in various shielding

materials. The user can configure the type of the radiation source and its energy distribution, the geometry and the shielding materials, the analysis requirements, e.g. particle fluence, the total ionizing dose or pulse-height spectrum (PHS) and define a physics model to be used for the simulation. The MULASSIS uses Geant4 [82] physics models, e.g. standard electromagnetic (EM) processes [83], low energy EM processes [84], coupled hadronic processes [85] and others.

In my simulation, I have used the standard EM physics model [83] with a 9 keV monoenergetic point source. The analysis output was the total ionizing dose. The dose deposited in the ePix100a sensor was simulated by using 13 layers representing the vertical structure of the sensor as shown in Fig. 8.1, namely: $1\,\mu$m Al, $10 \times 50\,\mu$m Si, $2\,\mu$m SiO_2 and $30\,\mu$m Sn. The per-layer simulated dose normalized to $1\,\mathrm{photon/cm^2}$ was combined with the already calculated spatial photon distribution integrated throughout all irradiation cycles yielding a per-pixel dose profile shown in Figure 9.7.

The top image of Figure 9.7 shows dose distribution in the sensor at the depth of the SiO_2 structures. A vertical projection of the dose profile visualizes the dose-depth-distribution through the column (left) and row (right) with the highest absorbed dose in the bottom half of Figure 9.7. As can be seen from the top panels of both plots, the distribution of the dose along the row is broader. This is due to the horizontal movement of the beam spot during irradiation.

The region closest to the surface at the entrance window has received a maximum dose of 1.3 MGy at column number 10 and row number 9. This dose is reduced by a factor of 240 to 5.4 kGy deposited at a depth of the SiO_2 structures due to absorption by the sensor material. The total dose integrated over the spot profile amounts to 180 MGy delivered to the sensor's surface when neglecting absorption in the sensor material. Correspondingly the beam spot integrated dose absorbed at the SiO_2 level is 760 kGy. The dose received by the ASIC is further reduced and can be estimated to < 24 kGy at the surface of the ASIC. The other structural features of the ASIC are neglected in this calculation.

It is to note that we do not expect effects related to dose enhancement as the thickness of the oxide layer is $\approx 2\,\mu$m (see section 4.3.1). Moreover, the dose calculations are not only based on the mass absorption coefficient of the given material but were estimated via Monte Carlo simulation, where the generation and range of secondary electrons in the given material were assumed.

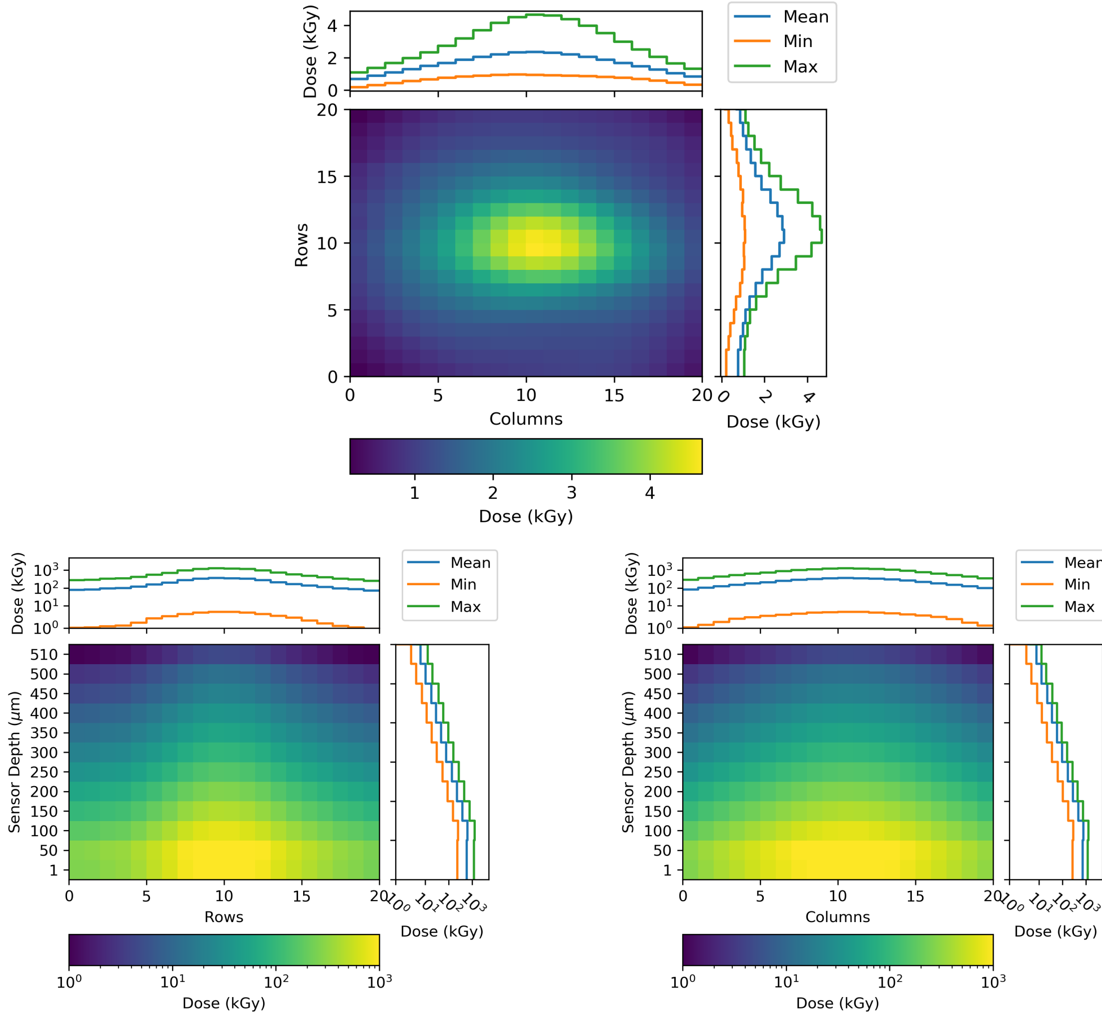

Figure 9.7: Top: The per-pixel dose distribution deposited at a depth of the SiO_2 layers in the region of interest (ROI) is shown. The bottom left corner of the plot corresponds to the bottom left corner of the ROI marked as a blue rectangle and being labelled "Irradiated Area" in Figure 9.2). Bottom: The depth dose distributions along the column 10 (left) and row 9 (right) of the region of interest. The image orientation is the same as the schematic view of the sensor shown in Figure 8.1 left, i.e. the 1μm thick Aluminium entrance window is located at the bottom and the pixel structure on the top of the images. It is to note that the dose values are shown on a linear scale in the top image and on a logarithmic scale in the bottom images.

9.5 Results

9.5.1 Immediate Effects

We have irradiated the ePix100a sensor with a beam attenuated below the immediate damage threshold to maximize the delivered dose. The beam intensity threshold was tested on a noisy ASIC. We have determined that the ePix100a module can withstand intensities with an energy of up to $E_{\mathrm{B}} \geq 1\,\mu\mathrm{J}$ for longer periods of time in the order of minutes. Hence this intensity was used for the module irradiation. Irradiation of the sensor with this intensity caused pixels in the centre of the 20 pixels × 20 pixels large ROI to become unresponsive. Despite their unresponsiveness during irradiation, these pixels were fully functional during the dark signal measurements.

After each irradiation run, the dark data collected exhibited an increasing number of individual pixels with their offset surpassing the upper level of the ADC dynamic range. Figure 9.8 shows the behaviour of pixels shortly after the last irradiation. Most of the area shown has pixels completely saturated with a signal (visualized in yellow colour). A discussion to the observed effects of unresponsive pixels and high-level offset is given in section 9.6.

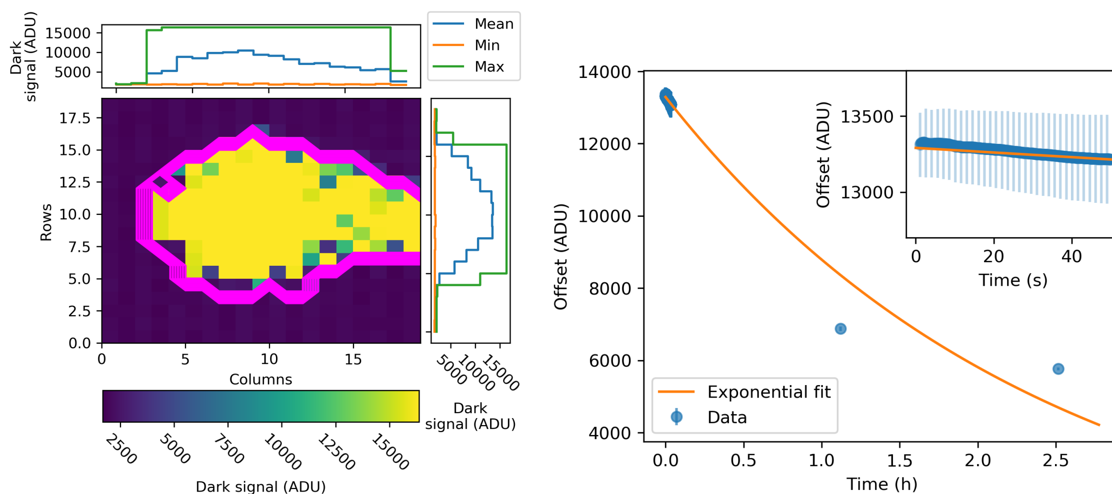

Figure 9.8: Left: Irradiated sensor area demonstrating saturated pixels with a dark signal above the dynamic range of the ADC. Right: An exponential decrease of the dark signal in a span of three hours after the irradiation.

9.5.2 Post-Irradiation Performance

Offset and Noise

During the first three hours following the last irradiation cycle the offset of individual pixels decreased exponentially with time with a decay constant of $-0.413\,\mathrm{h}^{-1}$ as shown in the right part of Figure 9.8 for $t_{\mathrm{Int}} = 800\,\mu\mathrm{s}$.

The offset stabilized three days after irradiation at a higher level of 1832 ADU in comparison to the pre-irradiation level of 1762 ADU. As apparent from Figure 9.9, the level of offset and noise change measured 3 days after irradiation remains the same also for the consecutive days. In general we observe a larger offset and corresponding ENC increase for $t_{\mathrm{Int}} = 800\,\mu\mathrm{s}$.

Evaluating the offset change 46 days after irradiation, yielded an offset increase by approximately 15% for $t_{\mathrm{Int}} = 800\,\mu\mathrm{s}$ and by 1% for $t_{\mathrm{Int}} = 50\,\mu\mathrm{s}$. As shown in the right part of Figure 9.9, the RMS noise observed in these pixels follows the same behaviour. While the noise at $t_{\mathrm{Int}} = 800\,\mu\mathrm{s}$ has increased by 85%, for $t_{\mathrm{Int}} = 50\,\mu\mathrm{s}$ the increase is at the level of 30%.

The measured increase in offset scales linearly with the integration time, i.e. with a factor of $800\,\mu\mathrm{s}/50\,\mu\mathrm{s} = 16$, which is expected if the effect is caused predominantly due to an increase of the dark current. As shown in Figure 9.10, the ratio of offset change for the two integration times approaches the expected factor of 16 when the leakage current increases, which happens for doses above $\approx 4\,\mathrm{kGy}$. The function qualitatively modelling the data consists of three regions describing the expected behaviour of the offset with different integration times. The first region, constant at one, expresses negligible contribution of the leakage current (dose = 0 Gy), hence no difference between shorter and longer integration time exists. As the dose increases, the leakage current exhibits a linear increase (the second region). Finally, it approaches the third region at a value of 16, which is expected when the leakage current dominates.

The spatial distribution of the induced offset (left) and noise (right) changes 46 days after irradiation is shown in Figure 9.11 for $t_{\mathrm{Int}} = 800\,\mu\mathrm{s}$ and for $t_{\mathrm{Int}} = 50\,\mu\mathrm{s}$ in Figure 9.12.

Since different pixels within the ROI have received a different dose and assuming the pixels inside the ROI react similarly to radiation-induced damage, we can evaluate the change of the offset and RMS noise between pre- and post-irradiation conditions depending on the dose. As the design of the pixels is the same, and minor variations in the sensor production process can be neglected, this assumption

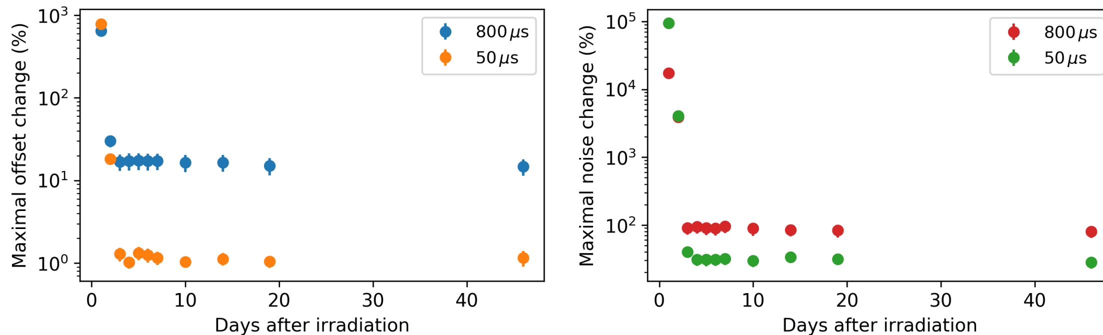

Figure 9.9: Left: Evolution of the offset as observed in the pixel showing the highest relative offset change for the two integration time settings, i.e. $t_{\mathrm{Int}} = 50\,\mu$s and $t_{\mathrm{Int}} = 800\,\mu$s. A stabilized state at increased offset values (with respect to the pre-irradiation offset level) follows the exponential decrease of the offset observed during the first days. Right: Relative change of the noise as observed during the days following the last irradiation cycle. The noise behaviour as a function of time mirrors the time evolution of the offset.

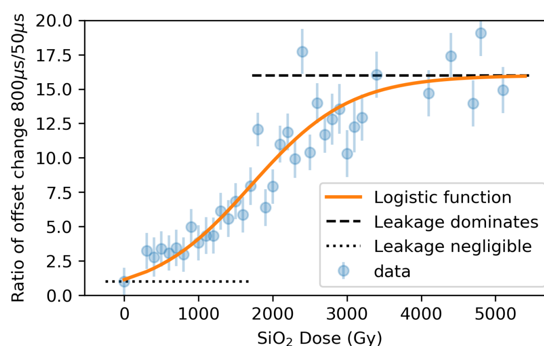

Figure 9.10: Ratio of the offset change measured at $800\,\mu$s and $50\,\mu$s (blue dots). The black line shows the scaling factor of 16 expected from the ratio of the integration times. The ratio of offset change for the two integration times approaches the expected factor of 16 when the leakage current contribution dominates, which happens for doses above $\approx 4\,$kGy.

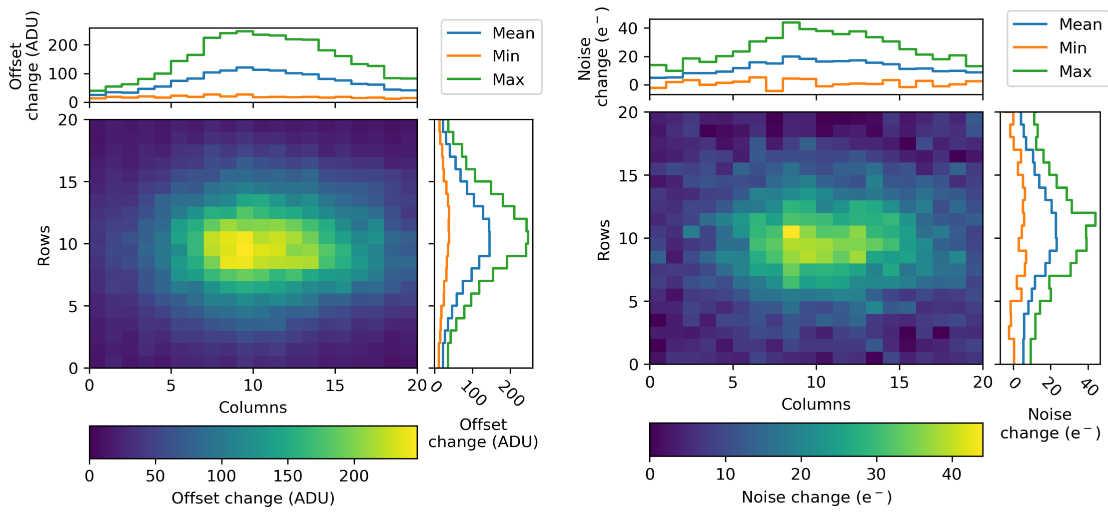

Figure 9.11: Radiation-induced changes of the offset (left) and noise (right) for $t_{\mathrm{Int}} = 800\,\mu\mathrm{s}$ evaluated 46 days after irradiation.

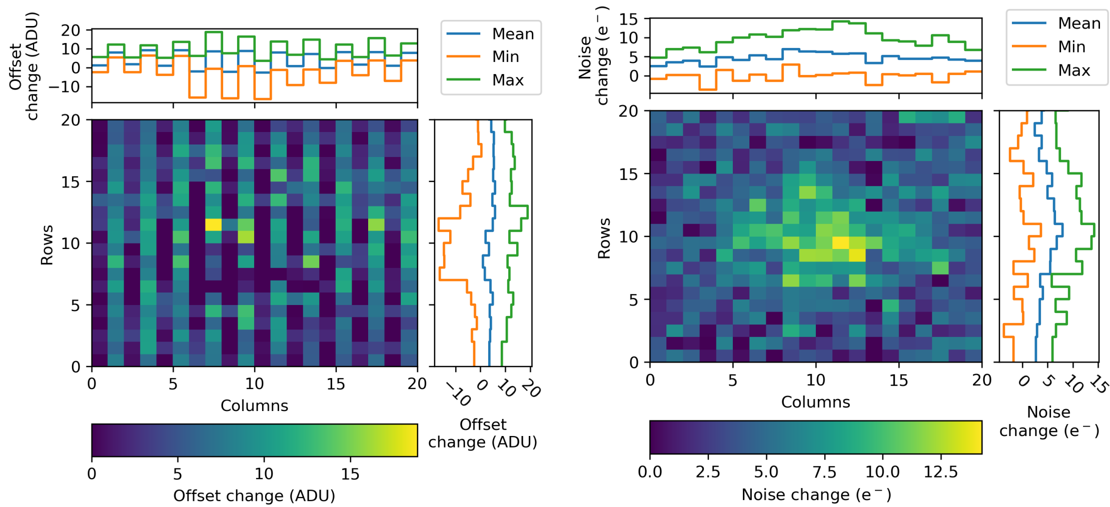

Figure 9.12: Radiation-induced changes of the offset (left) and noise (right) for $t_{\mathrm{Int}} = 50\,\mu\mathrm{s}$ evaluated 46 days after irradiation.

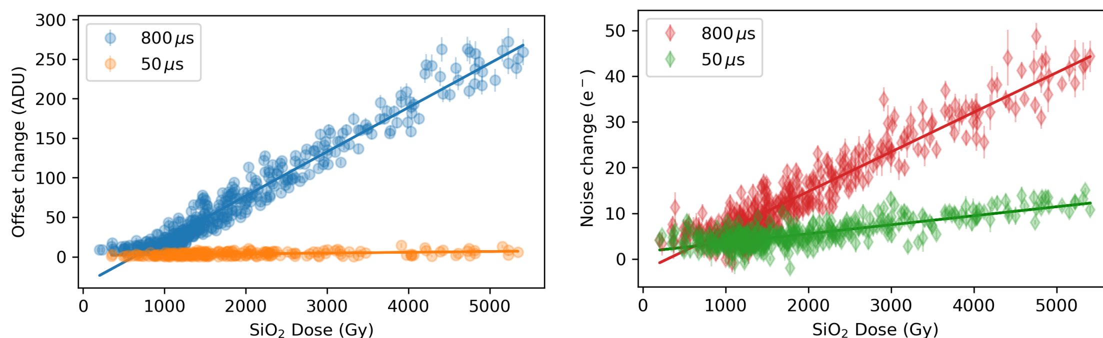

Figure 9.13: Left: The offset change observed in pixels of the ROI (difference between pre- and post-irradiation values) depending on the accumulated dose at the depth of SiO_2 layers is shown for $t_{\mathrm{Int}} = 50\,\mu$s (orange) and $t_{\mathrm{Int}} = 800\,\mu$s (blue). Right: Dependency of the ENC observed in pixels of the ROI on the accumulated dose in units of electrons for the same integration times (green: $50\,\mu$s, red: $800\,\mu$s).

is justified.

Figure 9.13 shows the offset (left) and noise (right) changes depending on the absorbed dose at the depth of the SiO_2 interface as measured 46 days post-irradiation. Here the influence of the longer integration time is clearly visible. The slope derived from fitting a linear function to the data yields an offset and ENC change rate of (56.0 ± 0.6) ADU/kGy and $(8.7 \pm 0.1)\,\mathrm{e}^-$/kGy for $t_{\mathrm{Int}} = 800\,\mu$s and (1.0 ± 0.2) ADU/kGy and $(2.0 \pm 0.1)\,\mathrm{e}^-$/kGy for $t_{\mathrm{Int}} = 50\,\mu$s, respectively.

If absorption of the radiation in silicon is neglected when calculating the dose, the offset and ENC change rate yields (235.9 ± 2.6) ADU/MGy and $(37.4 \pm 0.6)\,\mathrm{e}^-$/MGy for $t_{\mathrm{Int}} = 800\,\mu$s and (4.2 ± 0.6) ADU/MGy and $(8.3 \pm 0.4)\,\mathrm{e}^-$/MGy for $t_{\mathrm{Int}} = 50\,\mu$s The maximum observed increase of the offset reduces the available dynamic range of the detector by approximately 2% for $t_{\mathrm{Int}} = 800\,\mu$s and $\approx 0.1\%$ for $t_{\mathrm{Int}} = 50\,\mu$s.

Gain and Energy Resolution

In order to characterise the gain and energy resolution of the ePix100a after irradiation, we took post-irradiation Cu-fluorescence flat-field data. The data taking took place approximately one and a half hours after completion of the last irradiation cycle. At that time, most of the pixels in the central part of the ROI were still saturated, thus not detecting the charge created by a photon interaction. Due to time-constrained access to the instrument and beam, performing calibration measurements at a later time was not possible. Therefore, we have used pixels located

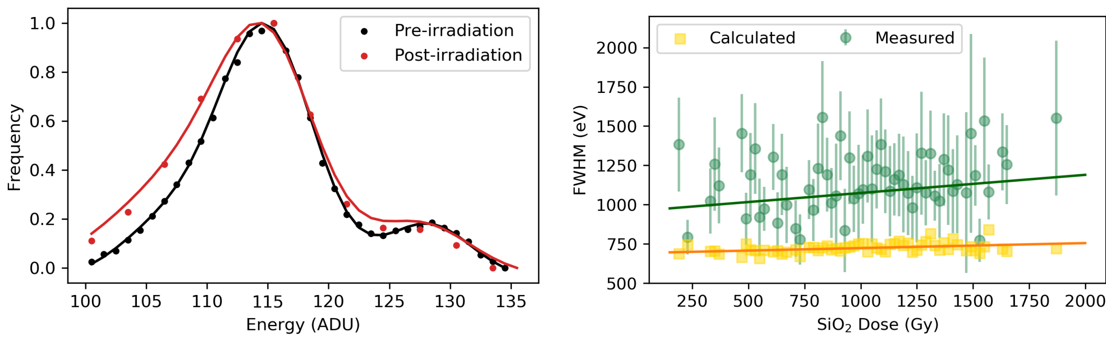

Figure 9.14: Left: The spectral distribution of the Cu-Kα photons and 9 keV photon peak (detected by pixels in the periphery of the ROI) before irradiation (black) and after irradiation (red). Right: The Cu-Kα peak width (assessed as FWHM) depending on the dose absorbed in the SiO_2 layer. Values extracted from the measurement are marked with green dots, while the yellow squares shows the expected FWHM values calculated from the noise.

in the periphery of the saturated area to compare the pre- and post-irradiation performance of the gain and energy resolution.

Figure 9.14 on the left shows a comparison of the measured spectrum of the Cu-K_α line blend and the 9 keV line before (black) and after irradiation (red). The spectrum was calculated from periphery pixels in the ROI. The FWHM of the lines is larger after irradiation, and the lines have a more pronounced low energy tail.

The right plot of Figure 9.14 shows the relation of FWHM on the dose accumulated by each pixel. We observe an increase of the FWHM at the level of (115 ± 71) eV/kGy. Following the Fano statistics-driven energy resolution of a detector described in section 6.3, an expected energy resolution can be calculated based on the measured noise. The yellow squares (labelled as "Calculated") refer to values calculated as given by Equation 6.10. The increase of the FWHM values follows the same slope (within the estimated errors) as the calculated intrinsic resolution values. The intercept values of the linear models are separated by (267 ± 82) eV, which is approximately consistent with the mean noise of peripheral pixels measured after irradiation, i.e. (167 ± 87) eV. These results suggest that a radiation-induced noise increase drives the observed broadening of the Cu-K lines. It is to note that in order to convert ADU values to eV/e^- units a pre-irradiation absolute gain value of $g = (70.1 \pm 0.8)$ eV/ADU was used.

Before irradiation we find (114.75 ± 0.07) ADU for the position of the C-K_α line blend. Figure 9.15 shows the position of the Cu lines extracted from single-pixel

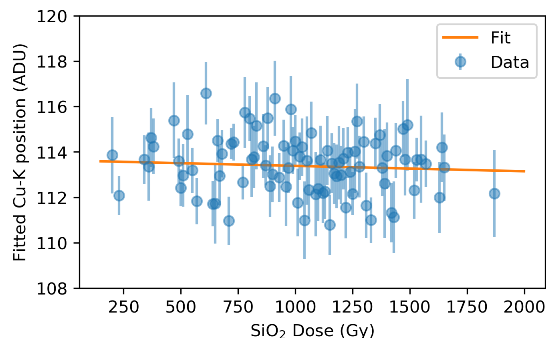

Figure 9.15: Position of the Cu-K line as a function of the absorbed dose in different pixels. The line position was determined by fitting a Gaussian model to the spectra.

spectra of irradiated pixels as a function of the absorbed dose. Applying a linear model to the data yields a slope consistent with 0, indicating that the position of the Cu-K line does not change with dose. The C-K_α lines after irradiation are located at (113.62 ± 0.37) ADU as we determined from the linear model.

As the flat-field calibration measurement contained only pixels with an absorbed dose below 2 kGy, we could not evaluate the behaviour of the gain for the most irradiated pixels.

In order to identify potential gain changes, we performed a charge injection scan with the current sources implemented in each pixel 240 days after irradiation. During this scan, an increasing amount of charge is injected into the pre-amplifier with an internal 10-bit pulser, thus simulating the charge created by photon interactions in the sensor material. In this mode, the sensor does not contribute to the measured signal. We used 1024 steps of the pulser to scan the full dynamic range of the ADC. Gain values depending on the absorbed dose calculated from Cu-K fluorescence data are shown on the left panel of Figure 9.16. The plot shows only gain values for doses below 2 kGy. The slope $(-4.6 \pm 5.7) \times 10^{-5}$ ADU keV^{-1}Gy^{-1} derived from a linear model fitted to the data is consistent with zero. This indicates that the gain does not change significantly up to a dose of $\approx$ 2 kGy. This behaviour changes as soon as higher dose levels were reached. Taking the charge injection data covering the range between 3500 Gy and 5500 Gy into consideration (right part of figure 9.16), we find the gain decreasing with the rate of $(-7.4 \pm 0.5) \times 10^{-5}$ ADU keV^{-1}Gy^{-1} as indicated by the black line in the right panel of Figure 9.16. Based on the estimated slope we expect a gain decrease by 1 ADU/keV per $\approx$ 13.5 kGy.

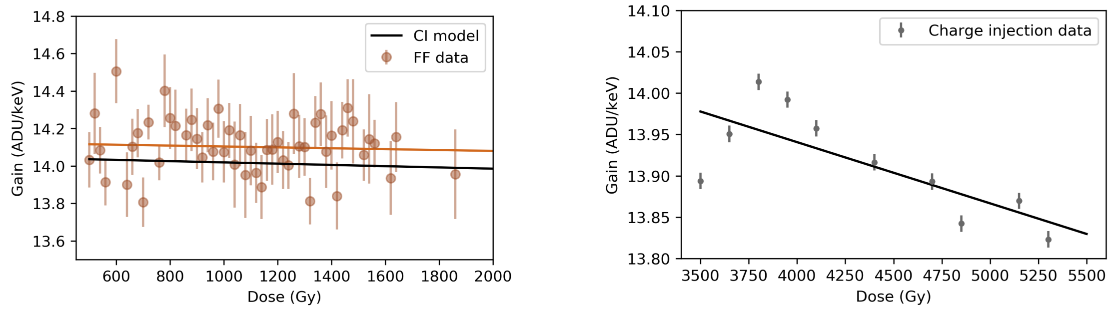

Figure 9.16: Left: Gain estimated from the Cu-K fluorescence data depending on dose. The black line shows a model derived from charge injection data (marked as "CI model") extrapolated to the dose range of $(500 - 5500)$ Gy. Right: The gain calculated from the internal charge injection data in relation to the absorbed dose is shown. Only gain values for a dose above 3.5 kGy were evaluated.

9.6 Discussion of the Observed Effects

9.6.1 Unresponsive Pixels upon Beam Irradiation

Irradiation with the high intensity FEL beam at an energy of $E_{\text{Beam}} \geq 1\,\mu$J caused unresponsive pixels for the beam centre with an area of approximately 20 pixels × 20 pixels. As the ASIC does not implement protection circuitry for signals significantly above the detector's dynamic range, and the pixels are not permanently damaged, the mechanism by which this occurs has to be further investigated. In that matter, we have established contact with the ASIC designers, who are following up with simulations of the electronic circuitry. One should emphasise that the observed effect is short-term and only present during ongoing beam irradiation. It does not lead to permanent damage: after irradiation, these pixels exhibit a dark signal saturating the detector's dynamic range (see section 9.6.2), but recover to an offset level comparable to the surrounding pixels within the following 48 hours.

9.6.2 Offset Surpassing the Dynamic Range of the ADC

Heat Simulation

The energy deposited to the sensor from the intense FEL beam can lead to a temperature rise of the irradiated area. Heating up of the sensor material leads to the generation of thermal charge carriers contributing to the leakage current. To investigate the observed high level of offset surpassing the dynamic range of the ADC, I

have performed a simulation of the heat distribution resulting from irradiation with the FEL beam. The main motivation was to investigate the time-scale of heat dissipation to the sensor material and understand if the accumulated heat could explain the increased offset.

The simulation of heat dissipation was done by numerical solving of a two-dimensional heat equation

$$\frac{\partial u}{\partial t} = \alpha \left(\frac{\partial^2 u}{\partial x^2} + \frac{\partial^2 u}{\partial y^2} \right) \tag{9.3}$$

with a Finite-Difference Method (FDM). The FDM is used to solve differential equations by approximation of derivatives with finite differences as explained in the following. The method is based on Taylor's theorem giving an approximation to an n-times differentiable function around a given point a by a series expansion given as

$$f(x) = \sum_{n=0}^{\infty} \frac{f^{(n)}(a)}{n!}(x-a)^n. \tag{9.4}$$

The derivative of the function f at point a is defined as

$$f'(a) = \lim_{h \to 0} \frac{f(a+h) - f(a)}{h}, \tag{9.5}$$

and if this limit exists, the function is differentiable. The Taylor's expansion of the function f, known as the Taylor polynomial, can be then written as

$$f(x_0 + \Delta x) = f(x_0) + \Delta x f'(x_0) + R_1(x), \tag{9.6}$$

where $R_1(x)$ corresponds to the difference between the original function and the first order Taylor approximation. If $R_1(x)$ is sufficiently small, it can be neglected. Taking $x_0 = a$ and $\Delta x = h$, one can write

$$\begin{aligned} f(a+h) &\approx f(a) + hf'(a), \\ f'(a) &\approx \frac{f(a+h) - f(a)}{h}. \end{aligned} \tag{9.7}$$

The last expression gives a linear approximation to the derivative defined by equation 9.5 [86].

To numerically solve the heat equation (Eq. 9.3) using the FDM, the spatial domain (x, y) and time domain (t) are partitioned as shown in Figure 9.17 left, yielding:

$$\begin{aligned} x_i &= i\Delta x, \\ y_j &= j\Delta y, \\ t_n &= n\Delta t. \end{aligned} \tag{9.8}$$

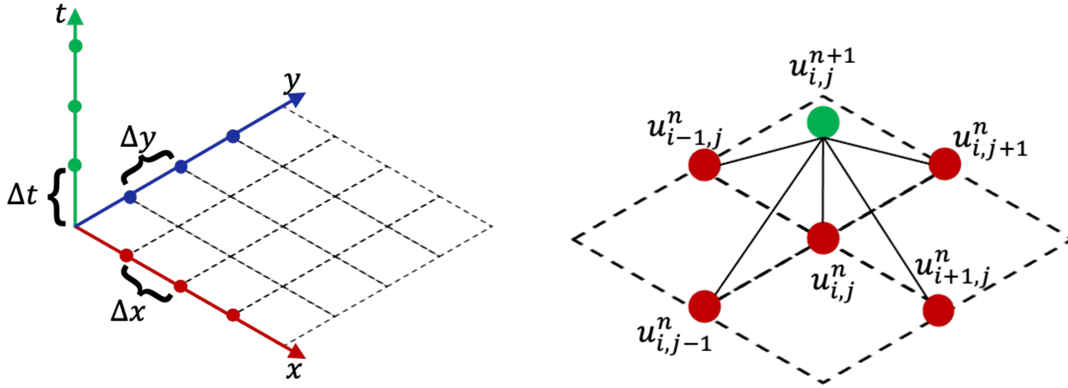

Figure 9.17: Left: Coordinate system for FDM partitioning, where x, y are spatial coordinates and t is the temporal coordinate. Right: Stencil of the explicit finite difference method for a two dimensional problem.

A solution of the heat equation is then given by

$$u(x_i, y_j, t_n) = u_{i,j}^n. \tag{9.9}$$

Using an explicit method of FDM, based on the stencil visualized in Figure 9.17, right panel, the heat equation can be rewritten to

$$\frac{u_{i,j}^{n+1} - u_{i,j}^n}{\Delta t} - \alpha \left(\frac{u_{i+1,j}^n - 2u_{i,j}^n + u_{i-1,j}^n}{\Delta x^2} + \frac{u_{i,j+1}^n - 2u_{i,j}^n + u_{i,j-1}^n}{\Delta y^2} \right) = 0. \tag{9.10}$$

Taking $\Delta x = \Delta y$, a solution of the heat equation in time $n+1$ is given as

$$\begin{aligned} u_{i,j}^{n+1} &= u_{i,j}^n (1 - \frac{4\alpha \Delta t}{\Delta x^2}) + r(u_{i+1,j}^n + u_{i-1,j}^n + u_{i,j+1}^n + u_{i,j-1}^n), \\ \text{where } r &= \alpha \frac{\Delta t}{\Delta x^2}. \end{aligned} \tag{9.11}$$

This explicit method is numerically stable when

$$\begin{aligned} (1 - \frac{4\alpha \Delta t}{\Delta x^2}) &\geq 0, \\ \Delta t &\leq \frac{\Delta x^2}{4\alpha}. \end{aligned} \tag{9.12}$$

The coefficient α is known as the thermal diffusivity of the material.

The sensor to be simulated was represented by a plate of 10 mm × 10 mm. The boundary conditions were defined as follows:

$$
\begin{aligned}
u(x,0,t) &= -9\,^{\circ}\mathrm{C}, \\
u(x,H,t) &= -9\,^{\circ}\mathrm{C}, \\
u(0,y,t) &= -9\,^{\circ}\mathrm{C}, \\
u(W,y,t) &= -9\,^{\circ}\mathrm{C}, \\
u(x,y,0) &= 0\,^{\circ}\mathrm{C}, \\
u(x=5,y=5,0) &= T_{init},
\end{aligned}
\tag{9.13}
$$

where W, H are the width and height of the plate and T_{init} is the initial temperature rise induced by the FEL beam during a 20 minutes long irradiation cycle given as

$$
T_{init} = \frac{Q}{c\rho V}. \tag{9.14}
$$

With $Q = 9.9\,\frac{\mu\mathrm{J}}{\mathrm{s}} \times 1200\,\mathrm{s}$, $c = 0.71\,\frac{\mathrm{J}}{\mathrm{gK}}$, $\rho = 2.33\,\frac{\mathrm{g}}{\mathrm{cm}^3}$, $V = (1 \times 1 \times 0.5)\,\mathrm{mm}^3$, where Q is induced thermal energy, c is the specific heat capacity of silicon, ρ is the silicon density, and V is the volume of the irradiated part of the sensor. As thermal energy, the average energy of the beam delivered per second was taken into account. In reality, the thermal energy delivered to the sensor is lower since a fraction of the beam energy is used for ionization processes. Therefore, using the total beam energy will provide an upper estimate of the time needed to dissipate the accumulated heat in the sensor material. Figure 9.18 shows the temperature distribution across the sensor area of $(10 \times 10)\,\mathrm{mm}^2$, 150 ms after the end of beam irradiation. The result shows that the accumulated heat can be sufficiently dissipated to the sensor material within a fraction of a second. Therefore the contribution of the thermal current several minutes after the irradiation, when dark measurements are performed, is negligible.

Distortion of Depletion Boundary

Another potential explanation of the offset exceeding the dynamic range of the ADC is the mechanism suggested by Schwandt et al. [73]. The generation of electron–hole pairs close to the Si–SiO_2 interface and build-up of positive charge lead to high electric fields near the interface, causing changes to the depletion boundary. Coulombic repulsion between positively doped boron implantation and positive charges accumulating near the oxide layer might result in the shrinking of the boron implanted region on its edges, thus exposing the metal contact as depicted in Figure 9.19. The distorted boron-doped region allows the depleted area to extend to the region

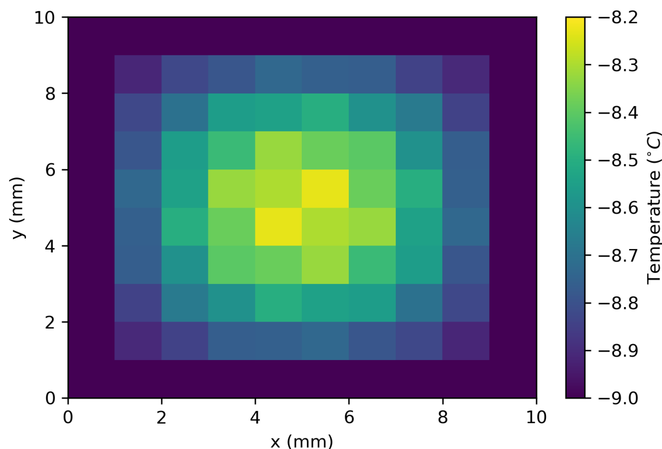

Figure 9.18: Temperature distribution on the 10 mm × 10 mm silicon sensor representation (neglecting its depth) 150 ms after a 20 minutes long irradiation with the direct FEL beam.

close to the metal contact. Potentially, the bending of the depletion boundary can reach the edges of the metal contact and thus increase the electron leakage current. When the generation of new charge carriers is interrupted, the recombination process dominates. Hence, the leakage current will decrease exponentially as observed and shown in the right part of Figure 9.8. A device simulation based on the specific design of the ePix100a sensor would be required to explain the observed behaviour in more detail, which is beyond the scope of this thesis.

9.6.3 Gain Changes

The radiation-induced effects on the gain, visible in the charge injection scan data, were pronounced at higher doses. Performing a charge injection scan allows separating different sources for the potential gain changes. Following the sensor and ASIC layout shown in Figure 8.1, we can identify two sources for the observed effect, radiation damage induced in the sensor and the readout electronics located in the ASIC. As the sensor-induced signal does not significantly contribute to the charge injection measurements, the observed gain changes indicate a radiation-induced effect on the readout electronics in the ASIC. Different mechanisms could lead to such an observed gain decrease. Presently, it is not fully understood which of these mechanisms contribute to the gain change observed in the ASIC, and further investigation is required, which is out of the scope of this thesis.

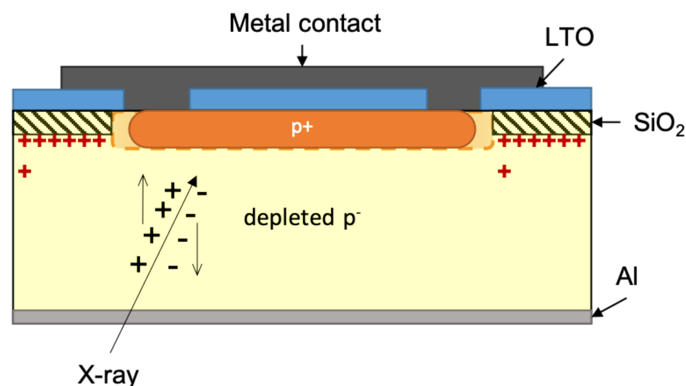

Figure 9.19: Schematic visualization of an ePix100a pixel when irradiated with high intensity. Dashed orange line shows the p^+ boron implanted layer under normal operating conditions. When charges are accumulated near the SiO_2 the boron implantation shrinks and exposes the metal contact to the depleted area.

9.7 Lifetime Estimate of the ePix100a

I have used the radiation-induced damage presented in the previous to estimate the lifetime of the detector depending on the beam energy used during experiments and limits for the measurement time beyond which the performance of the detector will significantly degrade. The estimates presented in the following are based on the extrapolation of the measured relationship of the induced damage and dose absorbed in the SiO_2 layer.

Figure 9.20 illustrates the time needed to reduce the dynamic range depending on the beam energy. A reduction of the dynamic range by 50% can be expected at a dose of ca. 131 kGy for $t_{\text{Int}} = 800\,\mu$s and at ca. 7.4 MGy for $t_{\text{Int}} = 50\,\mu$s deposited in a single pixel. This amounts to ca. 13 MGy for $t_{\text{Int}} = 800\,\mu$s and 740 MGy for $t_{\text{Int}} = 50\,\mu$s of dose deposited in the SiO_2 layer per 20 pixels × 20 pixels area (ROI), assuming a per-pixel beam distribution obtained during radiation damage study. Saturation of the ADC dynamic range will occur at 262 kGy ($t_{\text{Int}} = 800\,\mu$s), respectively at 14.8 MGy ($t_{\text{Int}} = 50\,\mu$s) for a single pixel, i.e. at 26 MGy ($t_{\text{Int}} = 800\,\mu$s) and at 1.48 GGy ($t_{\text{Int}} = 50\,\mu$s) of the total absorbed dose in the ROI. The left panel of Figure 9.20 shows three exemplary cases for the expected dynamic range behaviour: a dynamic range reduction as observed in this radiation damage study (blue dots), an extrapolated loss of 50% of the ADC range (orange dots) and the saturation of the ADC dynamic range due to the leakage current (green dots) for 800 μs integration time. The same cases are plotted for $t_{\text{Int}} = 50\,\mu$s on

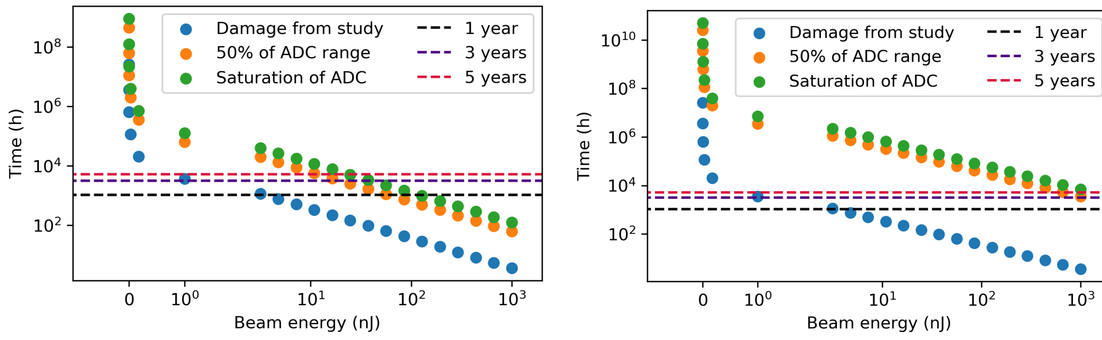

Figure 9.20: Estimate of time needed to reach specific level of the dynamic range reduction at a certain beam energy. Three scenarios are shown; the reduction level observed during this radiation damage study (blue dots), reduction to 50 % of the initial dynamic range (orange dots) and complete saturation of the ADC by the leakage current (green dots). The left plot shows the estimate for $t_{\text{Int}} = 800\,\mu$s and the right plot is for $t_{\text{Int}} = 50\,\mu$s.

the right. The lowest beam energy shown in both graphs corresponds to an energy equivalent to the upper limit of the ePix100a dynamic range, i.e. 100 photons at 8 keV. We assumed that mostly the same region of the detector is illuminated during scientific experiments for the estimate. This assumption is reasonable for small-angle scattering experiments. The horizontal lines in both plots visualize the number of hours the detector can be exposed to the beam during one, three and five years of operation at the EuXFEL to reach the corresponding dynamic range reduction. For our estimate, we assumed 4216 hours of beam time operation per calendar year at the EuXFEL. This value corresponds to the planned X-ray delivery time for the year 2021. As one beamline serves two scientific instruments, the allocated time is shared equally between the two instruments. Moreover, we estimate the detector to be exposed to X-rays only 50% of the available time. If the exposure time is taken as a variable, one can get a complementary estimate to the one shown in Figure 9.20. The estimates are provided for 5 years of operation at the EuXFEL, thus considering in total 10540 hours of the beam. Figure 9.21 illustrates the proportion of beam irradiation on the detector to reach a certain level of the dynamic range reduction at given beam energy.

As explained in section 6.4, peak-to-noise distinction expressed in the unit of standard deviation is often used as a parameter to evaluate the performance quality of spectroscopic detectors. Figure 9.22 shows decrease of a separation power below $5\,\sigma$ (cyan) or $3\,\sigma$ (magenta) at 9 keV if the detector is exposed to a given beam energy

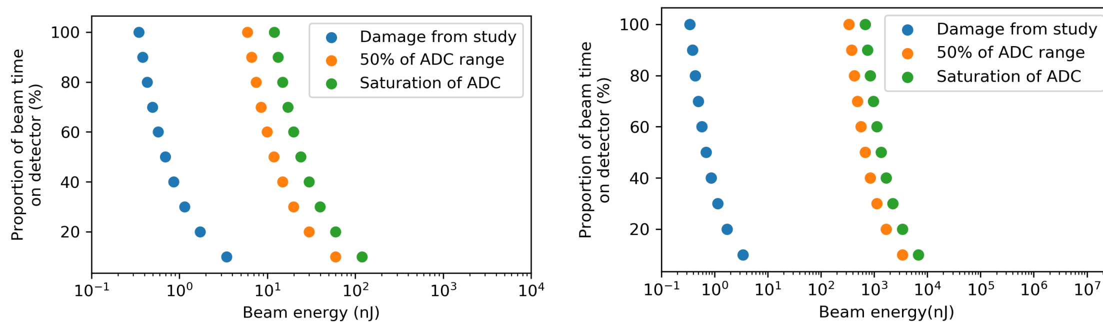

Figure 9.21: Fraction of an allocated beam time delivered to a detector needed to reach a specific level of the dynamic range reduction at certain beam energy. Three scenarios are shown; the reduction level observed during this radiation damage study (blue dots), reduction to 50 % of the initial dynamic range (orange dots) and complete saturation of the ADC by the leakage current (green dots). The left plot shows the estimate for $t_{\mathrm{Int}} = 800\,\mu\mathrm{s}$ and the right plot is for $t_{\mathrm{Int}} = 50\,\mu\mathrm{s}$.

for a specific amount of time. A plot on the left shows the separation power reduction at 800 μs integration time and the right plot at the integration time of 50 μs. As in the previous figure, the horizontal lines represent hours of exposure referenced to number of beam hours at the EuXFEL per calendar year. A critical noise increase, hence reduction in peak-to-noise separation is only expected with exposure to beam energies above the detector's dynamic range. Irradiating the detector for 2 years with a beam energy of 2.5 nJ would cause a drop below 3 σ at 800 μs integration time, while at $t_{\mathrm{Int}} = 50\,\mu\mathrm{s}$ the same energy during 5 years would lead to a drop below 5 σ. Assuming 5 years of operation at the EuXFEL, i.e. 10540 hours and identifying this time with 100 % of detector exposure time to beam an estimate for reduction of a peak-to-noise separation power based on detector exposure to the beam given as a fraction of the total allocated hours for specific beam energy can be made as shown in Figure 9.23

Table 9.2 summarizes estimates for SiO_2 dose thresholds above which the detector will demonstrate degraded performance in terms of reduced ADC range or reduction in peak separation strength.

Gain changes as shown in section 9.5.2 are depending on the absorbed dose only weakly due to significant attenuation by above-located metal connections and silicon sensor. Hence, the primary source for reduced performance is an increase in the detector noise, worsening the detector's energy resolution and reducing photon-to-noise separation power.

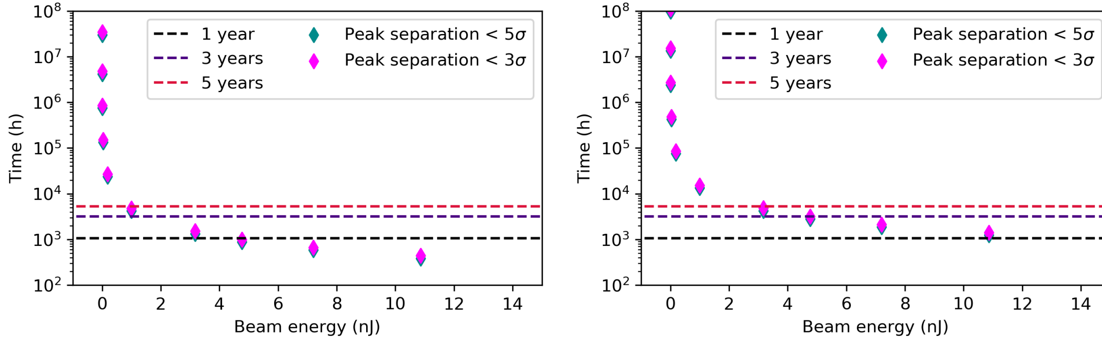

Figure 9.22: Estimate of time needed to reduce a peak-to-noise separation power below $5\,\sigma$ (green) and $3\,\sigma$ (pink) for $t_{\mathrm{Int}} = 800\,\mu$s, shown on the left panel and for $t_{\mathrm{Int}} = 50\,\mu$s shown on the right, in dependency of the used beam energy.

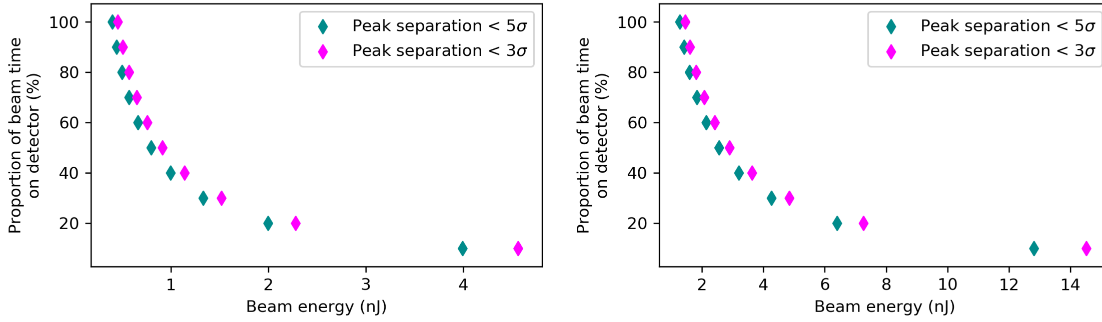

Figure 9.23: Proportion of detector exposure to beam (given as fraction of the total allocated beam hours during 5 years) needed to reduce a peak-to-noise separation power below $5\,\sigma$ (green) and $3\,\sigma$ (pink) at a given beam energy for $t_{\mathrm{Int}} = 800\,\mu$s, shown on the left panel and for $t_{\mathrm{Int}} = 50\,\mu$s shown on the right.

Table 9.2: Estimate of dose thresholds to experience degraded detector performance in terms of ADC range reduction and reduction in peak separation strength.

	Dose absorbed in SiO_2			
Integration time	ADC range reduction		Peak separation	
	50 %	100 %	$< 5\,\sigma$	$< 3\,\sigma$
$50\,\mu$s	7.4 MGy	14.8 MGy	28 kGy	32 kGy
$800\,\mu$s	131 kGy	262 kGy	9 kGy	10 kGy

Chapter 10

Conclusions and Outlook

In this thesis, I investigated the radiation damage of the ePix100a since its tolerance to FEL radiation has not been assessed before. The detector plays a key role in the scientific program of two EuXFEL instruments, i.e. HED and MID. In chapter 4, I introduced the mechanisms leading to surface radiation damage in detectors based on MOS structures and the effects this radiation damage induces. As was shown in chapter 6, the induced radiation damage effects influence the performance parameters of the detector, i.e. offset, noise, dynamic range, energy resolution, signal-to-noise and gain. Hence, the radiation damage of the ePix100a was evaluated and discussed in connection to these parameters. The influence of radiation-induced damage on the performance of the ePix100a detector is presented in chapter 9.

The ePix100a detector was irradiated under controlled conditions with the direct and attenuated EuXFEL beam with X-ray photons with an energy of 9 keV and a beam energy of 1 μJ. Pixels irradiated by this energy do not show a signal-dependent response upon irradiation but remain functional under normal operating conditions. The irradiated area of 1 mm^2 has received a dose of approximately 760 kGy at the depth of Si/SiO_2 in the sensor, which corresponds to 180 MGy delivered to the surface of the sensor.

The offset and noise were evaluated for two integration times, i.e. 50 μs and 800 μs. The integration time of $t_{\text{Int}} = 800\,\mu$s was selected due to the higher sensitivity even to small changes in the leakage current induced by radiation damage, while $t_{\text{Int}} = 50\,\mu$s corresponds to a typical integration time used at HED. The dominating source of the noise before irradiation was noise induced by readout electronics, while after receiving $\gtrapprox 4$ kGy at a depth of SiO_2, the contribution to the noise due to higher leakage current dominates. Hence I can conclude that the observed increase of the offset and noise is due to an increase of the leakage current. The same can be stated

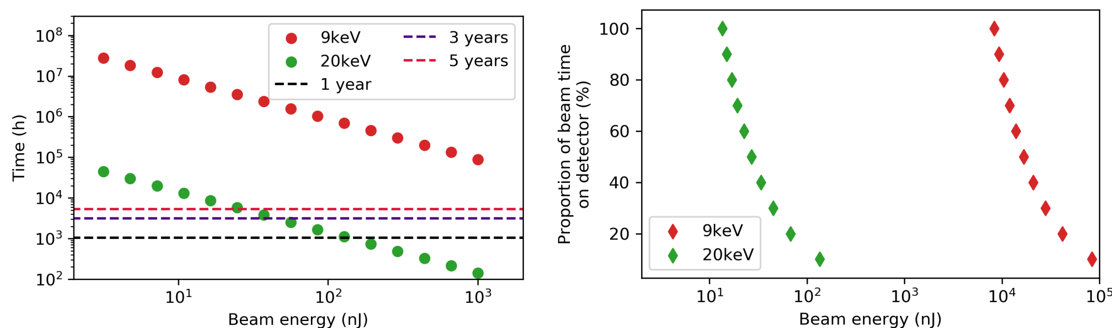

Figure 10.1: Estimates for a gain decrease by 1 ADU/keV for the photon energy of 9 keV (red) and the photon energy of 20 keV (green). Left: The estimate of time needed to observe a gain decrease depending on the used beam energy. Right: The plot shows the proportion of the allocated beam time the detector has to be exposed to during five years of operation at certain beam energy.

for the observed broadening of the Cu-K fluorescence line measured one and a half hours post-irradiation since the measured FWHM is scaling with the increasing noise observed in the pixels. I have observed a FWHM increase by $\approx 115\,\mathrm{eV/kGy}$.

A change of the gain is not expected for a dose $< 4\,\mathrm{kGy}$. Nevertheless, a charge injection scan showed a slight gain decrease for the most irradiated pixels and suggested weak damage occurring at the pixels' readout electronics. The gain depends on an absorbed dose only weakly as the incoming radiation was significantly attenuated by above-located metal connections and silicon sensor. In the case of higher photon energies, the ASIC will become more susceptible to radiation damage. The same energy deposited by, e.g. 20 keV photons would lead to an absorbed dose which is more than three orders of magnitude higher in comparison to 9 keV. Suppose the induced radiation damage on the readout electronics irradiated with 20 keV photons follows the same relation as observed for 9 keV photons. In that case a comparison for a time range to observe gain decrease by 1 ADU/keV can be made. Figure 10.1 illustrates the effect of photon energy on the time needed to observe a gain decrease by 1 ADU/keV at a given beam energy. The horizontal lines on the left panel visualize the number of hours the detector can be exposed to the beam during one, three and five years of operation at the EuXFEL to reach the mentioned gain decrease.

The results from the study of detector performance parameters on radiation-induced damage were extrapolated to assess the lifetime of a detector with regards to the impact of the detector parameters and their time evolution with irradiation on reliable scientific operation. Significant reduction of the dynamic range, i.e.

$R_{\mathrm{DR}} > 50\%$ is expected if the beam energy deposited in the pixel exceeds the dynamic range of the ADC by at least five orders of magnitude (for $t_{\mathrm{Int}} = 800\,\mu$s). Single-photon discrimination at a level of $> 5\,\sigma$ can be achieved with the ePix100a up to a dose of 9 kGy at $t_{\mathrm{Int}} = 800\,\mu$s and up to 28 kGy at $t_{\mathrm{Int}} = 50\,\mu$s. The results presented in this thesis are not exclusive to the EuXFEL but are of generic nature, thus can be transferred to other use cases and facilities.

In the near future, we plan to investigate the possibility of mitigating the radiation-induced damage and restoring the non-irradiated detector performance by sensor annealing to conclude the ePix100a radiation damage study. In the case of experiencing reversible (non-destructive) radiation damage during scientific experiments, this could potentially cure the module without the need to replace it.

I have shown that the main radiation-induced effect causing change to detector performance parameters is the radiation-induced leakage current. As was also shown, the level of the effect on the detector parameters depends on the integration time of the detector, i.e. the longer the integration time is, the higher increase of offset and noise can be expected. The imaging detectors operated at 4.5 MHz have the integration time in the range of tens to hundreds of nanoseconds, e.g. the LPD detector (see appendix A) has integration time of 90 ns. This is more than 500 times shorter time in comparison to the standard integration time of the ePix100a. The leakage current contribution to the noise of the LPD is a factor of 100 lower in comparison to the other noise sources [76], which means that in order to observe an increase of the noise caused by the increase of leakage current, the integration time would have to be two orders of magnitude higher. Figure A.2 in appendix A.2 shows the RMS noise during one year of operation of the most irradiated tiles compared to the least irradiated one. The values between tiles and throughout the whole year are comparable. The spatial noise distribution (see Fig. A.3) does not show any area exhibiting radiation-induced noise increase. The noisier pixels (ASIC) are within expectations and their noise is not related to radiation-induced damage. Hence, the radiation-induced damage comparable to the level presented by this study for a 4.5 MHz operated detector can not be characterized by the offset or noise increase. Instead, the effect on the gain, in the case of irradiation with higher photon energies or charge collection efficiency due to charge mobility decrease, could be of interest (see section 4.4.5).

This study proved that the ePix100a could be used without significant degradation of its performance for several years if the deposited energy in a given pixel throughout this time does not exceed 1 nJ. In such a case, the ageing of the detector

and its electronics will be driven by other processes than radiation damage effects.

Zhrnutie

V mojej práci som sa zamerala na skúmanie radiačného poškodenia detektora ePix100a, keďže detektor zohráva dôležitú úlohu pri experimentálnych meraniach na dvoch experimentálnych staniciach v EuXFEL (HED[87] a MID[88]). Ide o jedinečný a dôležitý výskum v tejto oblasti, keďže doterajšie zdroje neuvádzajú existenciu obnobných meraní.

Vplyv radiačného poškodenia som skúmala vzhľadom na operačné parametre detektora: ofset, šum, dynamický rozsah, energetické rozlíšenie, pomer signál-šum a konverzný faktor. Detektor bol ožarovaný priamym a čiastnočne odtieneným röntgenovým laserovým zväzkom, s použitím 9 keV fotónov s energiou 1 μJ. Pixely ožarované takouto energiou zväzku nevykazovali počas merania žiadny merateľný signál. Po ukončení ožarovania však opäť nadobudli svoju funkčnosť.

Ožiarená plocha veľkosti približne 20 pixelov × 20 pixelov, odhadom 1 mm^2, absorbovala dávku približne 760 kGy na rozhraní Si/SiO$_2$, čo zodpovedá približne 180 MGy na povrchu senzora.

Ofset a šum sa vyhodnocovali pre dva integračné časy, a to pre 50 μs and 800 μs. Dlhší integračný čas sme zvolili pre jeho vyššiu citlivosť na malé zmeny vo zvodovom prúde senzora a kratší čas je zvyčajným integračným časom používaným pri meraniach.

Pred ožarovaním bol hlavným zdrojom šumu deketora šum pochádzajúci z vyčítavacej elektroniky. Keď dávka v SiO$_2$ vrstve presiahne $\approx$ 4 kGy, radiačné poškodenie spôsobí, že sa hlavným zdrojom šumu stane zvodový prúd. Hlavnou príčinou pozorovaného nárastu ofsetu a šumu bol teda nárast zvodového prúdu, ktorý zapríčinilo naindukované radiačné poškodenie.

Nárast šumu viedol aj k zhoršeniu energetického rozlíšenia detektora. V závislosti od dávky sa fotopík rozšíril približne o 115 eV/kGy.

Pre dávky nižšie ako 4 kGy sa zmena konverzného faktora neočakáva. Vzhľadom na distribúciu zväzku na ožarovanej ploche 20 pixelov × 20 pixelov, jednotlivé pixely s vyššou absorbovanou dávkou vykazovali miernu zmenu konverzného faktora. Zá-

vislosť konverzného faktora od dávky je nízka, kvôli výraznej absorpcii žiarenia v objeme kremíkového senzora. Ak by sa však na ožarovanie použili fotóny s vyššou energiou, vyčítavacia elektronika by bola oveľa náchylnejšia na poškodenie. Napríklad, v prípade použitia 20 keV fotónov by bola absorbovaná dávka o tri rády vyššia, v porovnaní s 9 keV fotónmi.

Vzhľadom na absorbovanú dávku boli namerané zmeny v parametroch detektora použité na odhad životnosti tohto detektora. Životnosť detektora sa posudzovala vzhľadom na hodnoty parametrov, ktoré musí dosahovať pri experimentálnych meraniach. Výrazné zníženie dynamického rozsahu sa očakáva v prípade, že energia deponovaná v senzore počas jeho používania, presiahne dynamický rozsah ADC najmenej o päť rádov (pre $t_{\mathrm{Int}} = 800\,\mu$s). Schopnosť rozlišovania jednotlivých 9 keV fotónov s rozlíšením $> 5\,\sigma$ sa zachová, ak dávka nepresiahne 9 kGy pre $t_{\mathrm{Int}} = 800\,\mu$s, a až do dávky 28 kGy pre $t_{\mathrm{Int}} = 50\,\mu$s.

Uvedené experimentálne výsledky nie sú platné výhradne iba pre EuXFEL, ale sú aplikovateľné aj pre iné zariadenia. V blízkej budúcnosti plánujeme skúmať žíhanie senzora ako spôsob ozdravenia detektora a návrat k pôvodným parametrom. Ak by sa pozorovalo zhoršenie parametrov detektora, možnosť žíhania by umožnila nápravu, bez nutnosti výmenny takto poškodeného detektora.

Prezentovaný výskum ukázal, že hlavný vplyv na zmenu parametrov mal nárst zvodového prúdu ako dôsledok radiačného poškodenia. Taktiež sa ukázalo, že čím je vyšší integračný čas, tým výraznejší je vplyv zvodového prúdu. Zobrazovacie detektory snímajúce s frekvenciou 4.5 MHz, majú integračný čas v rozmedzí desiatok až stoviek nanosekúnd. Napríklad integračný čas LPD detektora je $t_{\mathrm{Int}} = 90$ ns. To je vyšše 500-násobné skrátenie času, v porovnaní so štandardným integračným časom ePix100a. Zvodový prúd LPD prispieva k celkovému šumu detektora 100-násobne menej v porobnaní s inými zdrojmi [76]. Inak povedané, aby bolo možné pozorovať nárast šumu spôsobený nárastom zvodového prúdu, integračný čas by musel byť o dva rády dlhší. Pri 4.5 MHz detektore teda platí, že jeho riadiačné poškodenie nemôže byť vyhodnotené pomocou nárastu ofsetu alebo šumu. Vhodnejšími parametrami na sledovanie by v tomto prípade boli konverzný faktor alebo účinnosť zberu nosičov náboja. Pre efektívny zber náboja pri 4.5 MHz detektore je dôležitá pohyblivosť vytvoreného náboja, ktorá, ako bolo spomínané, sa riadiačným poškodením znižuje.

Náš výskum ukázal, že radiačná odolnosť detektora ePix100a je dostatočná, pričom umožňuje niekoľkoročnú prevádzku bez výraznejšieho znehodnotenia jeho parametrov. Platí to za predpokladu, že energia deponovaná v pixeloch počas tohto obdobia nepresiahne 1 nJ. V takom prípade by primárnemu poškodeniu detektora a

jeho elektroniky dominovali iné mechanizmy, než procesy vyplývajúce z radiačného poškodenia.

Appendices

Appendix A

The LPD Detector

A.1 Mapping

Figure A.1 shows the naming convention used for tiles and modules of the LPD detector. The LPD is a modular hybrid one-megapixel detector system consisting of four movable detector quadrants (denoted with Q). Each quadrant is made from four supermodules (denoted with M). The supermodules are built from so-called tiles, which are pixel sensor units. The one-megapixel system comprises 256 detector tiles. The LPD sensors are fabricated from high resistivity silicon. A tile sensor area is composed of 32×128 pixels with $500 \times 500\,\mu m^2$ size with a sensor thickness of $500\,\mu m$. Each sensor is bump bonded to 8 ASICs with one ASIC covering readout channels of 512 pixels, i.e. 32×16 pixels.

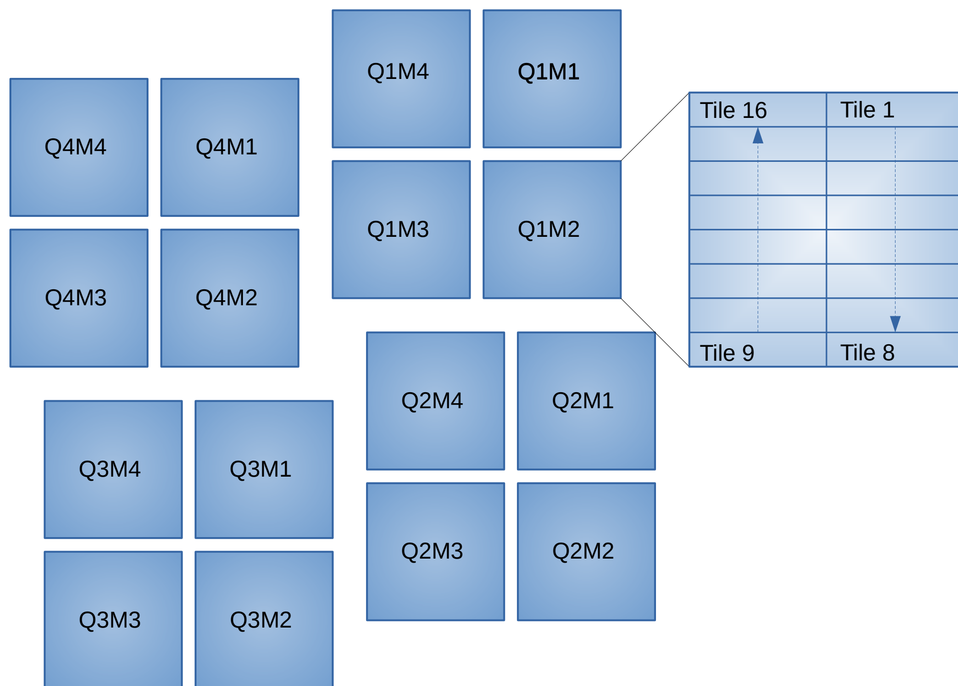

Figure A.1: The drawing illustrates the placement of the LPD modules and the corresponding naming convention.

A.2 Time Evolvement of the Noise

Figure A.2 shows the RMS noise evolvement of the selected tiles during one year of operation. Tiles from the right central part of the detector were selected as they were the most exposed to the radiation, namely tiles 8 and 9 from Q1M3 and tile 8 from Q1M2. A tile from the most distant corner, i.e. tile 16 from Q4M4, was evaluated to compare noise values for the least irradiated detector part.

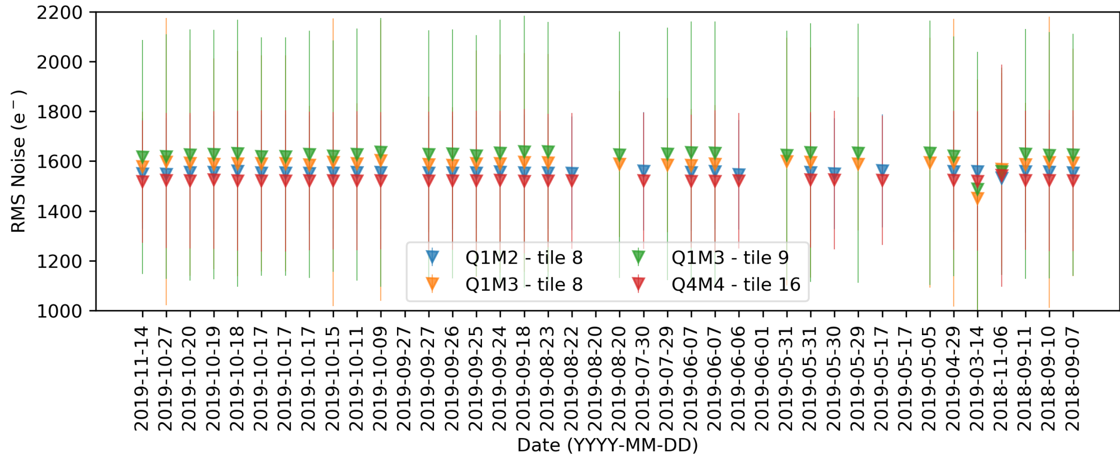

Figure A.2: RMS noise values of the selected LPD tiles collected during one year of operation. Tiles from the most exposed modules (Q1M2, Q1M3) were compared with the most distant tile of the LPD with regards to the amount of received radiation. No significant change in noise values is present. The naming convention for the LPD building blocks and their placement is shown in A.1

.

A.3 Spatial Distribution of the Noise

Figure A.3 shows the spatial distribution of the RMS noise of the same tiles plotted in Figure A.2 for the 27th of October 2019. The noisier pixels appearing close to the edges of the ASICs (visualized by white lines) are typical LPD feature and are due to the design of the ASICs. The two noisy areas spanning through two ASICs in tile 9 of Q1M3 are due to damage on the sensor or the electronic, not related to radiation damage. The LPD detector is operated in an ambient atmosphere. Hence it is prone to environmental damage by, e.g. collection of dust on sensors, humidity effects on electronics, unintentional mechanical damage caused by handling and others.

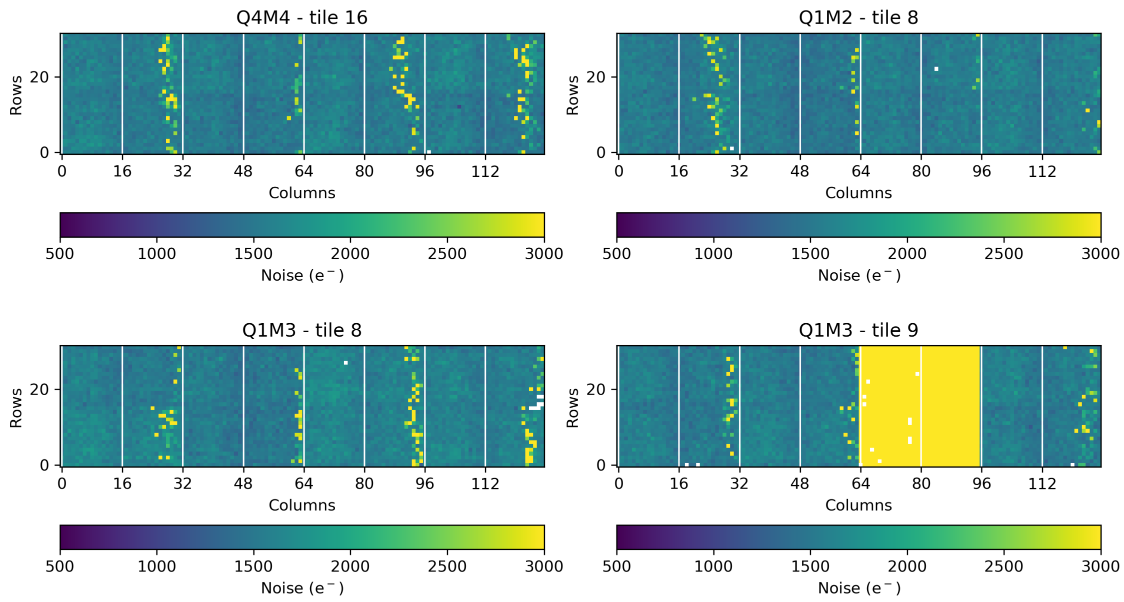

Figure A.3: Spatial distribution of noise of the selected LPD tiles. The same tiles are plotted as in Figure A.2 for the 27th of October 2019. The white lines visualize 8 readout ASICs present per tile.

Bibliography

1. TSCHENTSCHER, T. et al. Photon Beam Transport and Scientific Instruments at the European XFEL. *Applied Sciences*. 2017-06-09, vol. 7. Available from DOI: `10.3390/app7060592`.
2. SALDIN, E. et al. *The Physics of Free Electron Lasers*. Springer Science & Business Media, 2013.
3. CLARKE, James A. *The Science and Technology of Undulators and Wigglers*. Oxford University Press on Demand, 2004. Available from DOI: `10.1093/acprof:oso/9780198508557.001.0001`.
4. SCHWANDT, J. *Design of a Radiation Hard Silicon Pixel Sensor for X-ray Science*. 2014. PhD thesis. Hamburg University.
5. GRAAFSMA, H. Requirements for and Development of 2 Dimensional X-ray Detectors for the European X-ray Free Electron Laser in Hamburg. *Journal of Instrumentation*. 2009-12-14, vol. 4, no. 12, pp. P12011. Available from DOI: `10.1088/1748-0221/4/12/P12011`.
6. KUSTER, Markus et al. Detectors and Calibration Concept for the European XFEL. *Synchrotron radiation news*. 2014-07-22, vol. 27, no. 4, pp. 35–38. Available from DOI: `10.1080/08940886.2014.930809`.
7. ZHANG, J. *X-ray Radiation Damage Studies and Design of a Silicon Pixel Sensor for Science at the XFEL*. 2013. PhD thesis. Hamburg University.
8. ALLAHGHOLI, A et al. AGIPD, a High Dynamic Range Fast Detector for the European XFEL. *Journal of Instrumentation*. 2015-01-21, vol. 10, no. 01, pp. C01023. Available from DOI: `10.1088/1748-0221/10/01/C01023`.
9. PORRO, Matteo et al. Development of the DEPFET Sensor with Signal Compression: A Large Format X-ray Imager with Mega-Frame Readout Capability for the European XFEL. *IEEE Transactions on Nuclear Science*. 2012-10-

11, vol. 59, no. 6, pp. 3339–3351. Available from DOI: 10.1109/TNS.2012.2217755.

10. PORRO, Matteo et al. The MiniSDD-based 1-Megapixel Camera of the DSSC Project for the European XFEL. *IEEE Transactions on Nuclear Science*. 2021-04-29. Available from DOI: 10.1109/TNS.2021.3076602.
11. MARKOVIC, B et al. Design and Characterization of the ePix100a: A Low Noise Integrating Pixel ASIC for LCLS Detectors. In: *2014 IEEE Nuclear Science Symposium and Medical Imaging Conference (NSS/MIC)*. 2014-11-08, pp. 1–3. Available from DOI: 10.1109/NSSMIC.2014.7431230.
12. BLAJ, G et al. X-ray Imaging with ePix100a: A High-Speed, High-Resolution, Low-Noise Camera. In: *Hard X-Ray, Gamma-Ray, and Neutron Detector Physics XVIII*. 2016-09-30, vol. 9968, 99680J. Available from DOI: 10.1117/12.2238136.
13. DENES, P et al. A Fast, Direct X-ray Detection Charge-Coupled Device. *Review of Scientific Instruments*. 2009-08-06, vol. 80, no. 8, pp. 083302. Available from DOI: 10.1063/1.3187222.
14. JANUSCHEK, Friederike et al. Performance of the LBNL FastCCD for the European XFEL. In: *2016 IEEE Nuclear Science Symposium, Medical Imaging Conference and Room-Temperature Semiconductor Detector Workshop*. 2016-11-29, pp. 1–3. Available from DOI: 10.1109/NSSMIC.2016.8069829.
15. JUNGMANN-SMITH, JH et al. JUNGFRAU 0.2: Prototype Characterization of a Gain-Switching, High Dynamic Range Imaging System for Photon Science at SwissFEL and Synchrotrons. *Journal of Instrumentation*. 2014-12-15, vol. 9, no. 12, pp. P12013. Available from DOI: 10.1088/1748-0221/9/12/P12013.
16. HART, Mathew et al. Development of the LPD, a High Dynamic Range Pixel Detector for the European XFEL. In: *2012 IEEE Nuclear Science Symposium and Medical Imaging Conference Record (NSS/MIC)*. 2012-11-27, pp. 534–537. Available from DOI: 10.1109/NSSMIC.2012.6551165.
17. KUSTER, Markus et al. The 1-Megapixel pnCCD Detector for the Small Quantum Systems Instrument at the European XFEL: System and Operation Aspects. *Journal of Synchrotron Radiation*. 2021-03, vol. 28, no. 2, pp. 576–587. Available from DOI: 10.1107/S1600577520015659.

18. PETRUCCI, RH et al. *Temperature and Conductivity* [online]. 2020-08-25 [visited on 2020-05-06]. Available from: `https://chem.libretexts.org/@go/page/36874`.

19. SZE, SM et al. *Semiconductor Devices: Physics and Technology, 3rd Edition*. Wiley Global Education, 2012-05. ISBN 978-0-470-53794-7.

20. MISIAKOS, K et al. Accurate Measurements of the Silicon Intrinsic Carrier Density from 78 to 340 K. *Journal of applied physics*. 1993-05, vol. 74, no. 5, pp. 3293–3297. Available from DOI: `https://doi.org/10.1063/1.354551`.

21. CARSTEN, Niebuhr. *Solid State Detectors* [online] [visited on 2019-01-24]. Available from: `http://www.desy.de/~niebuhr/Vorlesung/Detektor/Vorlesung_4.pdf`.

22. THOMPSON, D. *Thermoelectric Properties of Silicon Germanium: An In-depth Study to the Reduction of Lattice Thermal Conductivity*. 2012-08. Available also from: `https://tigerprints.clemson.edu/all_dissertations/984`. PhD thesis. Clemson University.

23. BERGER, MJ. NIST Standard Reference Database 8 (XGAM). *National Institute of Standards and Technology, Gaithersburg, MD, USA*. 2010. Available from DOI: `10.18434/T48G6X`.

24. BUSHBERG, Jerrold T et al. *The Essential Physics of Medical Imaging*. Lippincott Williams & Wilkins, 2011-12-28. ISBN 978-0-7817-8057-5.

25. KNOLL, GF. *Radiation Detection and Measurement*. John Wiley & Sons, 2010-08. ISBN 978-0-470-13148-0.

26. KLEIN, O et al. Über die Streuung von Strahlung durch freie Elektronen nach der neuen relativistischen Quantendynamik von Dirac. *Zeitschrift für Physik*. 1929-11, vol. 52, no. 11, pp. 853–868. ISSN 0044-3328. Available from DOI: `10.1007/BF01366453`.

27. HUBBELL, John H. Polarization Effects in Coherent and Incoherent Photon Scattering: Survey of Measurements and Theory Relevant to Radiation Transport Calculations. *Indian Journal of Physics*. 1992, vol. 67, pp. 463–479. Available also from: `https://core.ac.uk/download/pdf/158962211.pdf`.

28. HUBBELL, John H. *Bibliography and Current Status of K, L, and Higher Shell Fluorescene Yields for Computations of Photon Energy-Absorption Coefficients*. 1989. Technical report. US Dept. of Commerce, National Institute of Standards and Technology.

29. *Interaction of Gamma Radiation with Matter* [Nuclear Power Web] [visited on 2019-01-09]. Available from: `http://www.nuclear-power.net/nuclear-power/reactor-physics/interaction-radiation-matter/interaction-gamma-radiation-matter/#prettyPhoto`.

30. LUTZ, G. et al. *Semiconductor Radiation Detectors*. Springer, 1999.

31. YANG, Xiaofan et al. Permittivity of Undoped Silicon in the Millimeter Wave Range. *Electronics*. 2019-08-10, vol. 8, no. 8, pp. 886. Available from DOI: `10.3390/electronics8080886`.

32. GRAY, Paul R et al. *Analysis and Design of Analog Integrated Circuits*. Wiley, 2001. ISBN 978-0-470-24599-6.

33. AFFOLDER, A et al. Silicon detectors for the sLHC. *Nuclear Instruments and Methods in Physics Research Section A: Accelerators, Spectrometers, Detectors and Associated Equipment*. 2011, vol. 658, no. 1, pp. 11–16. Available from DOI: `10.1016/j.nima.2011.04.045`.

34. LINDSTRÖM, Gunnar. Radiation Damage in Silicon Detectors. *Nuclear Instruments and Methods in Physics Research Section A: Accelerators, Spectrometers, Detectors and Associated Equipment*. 2003-10-11, vol. 512, no. 1, pp. 30–43. ISSN 0168-9002. Available from DOI: `10.1016/S0168-9002(03)01874-6`.

35. VAN LINT, Victor AJ et al. Mechanisms of Radiation Effects in Electronic Materials. Volume 1. *NASA STI/Recon Technical Report A*. 1980, vol. 81.

36. VAN GINNEKEN, A. *Nonionizing Energy Deposition in Silicon for Radiation Damage Studies*. 1989. Technical report. Fermi National Accelerator Laboratory.

37. DEAL, B. E. Standardized Terminology for Oxide Charges Associated with Thermally Oxidized Silicon. *IEEE Transactions on Electron Devices*. 1980, vol. 27, no. 3, pp. 606–608.

38. MCLEAN, F Barry et al. *Basic Mechanisms of Radiation Effects in Electronic Materials and Devices*. 1987-09-01. Technical report. HARRY DIAMOND LABS ADELPHI MD.

39. SCHWANK, James R et al. Radiation Effects in MOS Oxides. *IEEE Transactions on Nuclear Science*. 2008-09-30, vol. 55, no. 4, pp. 1833–1853. Available from DOI: `10.1109/TNS.2008.2001040`.

40. HUGHES, RC. Charge-Carrier Transport Phenomena in Amorphous SiO2: Direct Measurement of the Drift Mobility and Lifetime. *Physical Review Letters*. 1973-04-13, vol. 30, no. 26, pp. 1333. Available from DOI: `10.1103/PhysRevLett.30.1333`.

41. DOZIER, CM et al. Effect of Photon Energy on the Response of MOS Devices. *IEEE Transactions on Nuclear Science*. 1981-12, vol. 28, no. 6, pp. 4137–4141. Available from DOI: `10.1109/TNS.1981.4335689`.

42. OLDHAM, Timothy R et al. Total Ionizing Dose Effects in MOS Oxides and Devices. *IEEE transactions on nuclear science*. 2003-07-09, vol. 50, no. 3, pp. 483–499. Available from DOI: `10.1109/TNS.2003.812927`.

43. AUSMAN JR, George A et al. Electron-Hole Pair Creation Energy in SiO2. *Applied Physics Letters*. 1975, vol. 26, no. 4, pp. 173–175. Available from DOI: `10.1063/1.88104`.

44. BENEDETTO, Joseph M et al. The Relationship Between 60Co and 10-keV X-ray Damage in MOS Devices. *IEEE Transactions on Nuclear Science*. 1986-12, vol. 33, no. 6, pp. 1317–1323. Available from DOI: `10.1109/TNS.1986.4334599`.

45. LERAY, Jean-Luc. Total Dose Effects: Modeling for Present and Future. In: *IEEE NSREC Short Course*. 1999, vol. 23, pp. 225–231. No. 3.

46. MONTROLL, Elliott W et al. Random Walks on Lattices. II. *Journal of Mathematical Physics*. 1965, vol. 6, no. 2, pp. 167–181. Available from DOI: `10.1063/1.1704269`.

47. OLDHAM, Timothy R. *Ionizing Radiation Effects in MOS Oxides*. World Scientific, 2000-01. ISBN 978-981-281-364-0. Available from DOI: `https://doi.org/10.1142/3655`.

48. FEIGL, Frank J et al. Oxygen Vacancy Model for the E1' Center in SiO2. *Solid State Communications*. 1974-02-01, vol. 14, no. 3, pp. 225–229. Available from DOI: `10.1016/0038-1098(74)90840-0`.

49. FLEETWOOD, Daniel M et al. *Defects in Microelectronic Materials and Devices*. CRC Press Taylor & Francis Group, 2008-11-19. ISBN 9781420043761.

50. LELIS, AJ et al. Reversibility of Trapped Hole Annealing. *IEEE Transactions on Nuclear Science*. 1988-12, vol. 35, no. 6, pp. 1186–1191. Available from DOI: `10.1109/23.25437`.

51. LELIS, AJ et al. The Nature of the Trapped Hole Annealing Process. *IEEE Transactions on Nuclear Science*. 1989-12, vol. 36, no. 6, pp. 1808–1815. Available from DOI: 10.1109/23.45373.

52. MCLEAN, FB. A Framework for Understanding Radiation-Induced Interface States in SiO2 MOS Structures. *IEEE transactions on Nuclear Science*. 1980-12, vol. 27, no. 6, pp. 1651–1657. Available from DOI: 10.1109/TNS.1980.4331084.

53. OLDHAM, TR et al. Comparison of 60Co Response and 10 KeV X-ray Response in MOS Capacitors. *IEEE Transactions on Nuclear Science*. 1983-12, vol. 30, no. 6, pp. 4377–4381. Available from DOI: 10.1109/TNS.1983.4333141.

54. FLEETWOOD, DM et al. Using Laboratory X-ray and Cobalt-60 Irradiations to Predict CMOS Device Response in Strategic and Space Environments. *IEEE Transactions on Nuclear Science*. 1988-12, vol. 35, no. 6, pp. 1497–1505. Available from DOI: 10.1109/23.25487.

55. CHANG, CP. Radiation Hardened N-Buried Channel CCD's Using Backside Phosphorus Gettering. *IEEE Transactions on Nuclear Science*. 1978-12, vol. 25, no. 6, pp. 1454–1458. Available from DOI: 10.1109/TNS.1978.4329552.

56. BLACKBURN, DL et al. The Effect of Ionizing Radiation on the Breakdown Voltage of Power MOSFETs. *IEEE Transactions on Nuclear Science*. 1983-12, vol. 30, no. 6, pp. 4116–4121. Available from DOI: 10.1109/TNS.1983.4333092.

57. PUGH, RD et al. Characteristics of the Breakdown Voltage of Power MOSFETs After Total Dose Irradiation. *IEEE Transactions on Nuclear Science*. 1986-12, vol. 33, no. 6, pp. 1460–1464. Available from DOI: 10.1109/TNS.1986.4334623.

58. MA, Tso-Ping et al. *Ionizing Radiation Effects in MOS Devices and Circuits*. John Wiley & Sons, 1989-04. ISBN 978-0-471-84893-6.

59. SEXTON, Fred W et al. Correlation of Radiation Effects in Transistors and Integrated Circuits. *IEEE Transactions on Nuclear Science*. 1985-12, vol. 32, no. 6, pp. 3975–3981. Available from DOI: 10.1109/TNS.1985.4334053.

60. RANUAREZ, Juan C et al. A Review of Gate Tunneling Current in MOS Devices. *Microelectronics reliability*. 2006-12, vol. 46, no. 12, pp. 1939–1956. Available from DOI: 10.1016/j.microrel.2005.12.006.

61. NATHAN, V et al. Gate-Induced Drain Leakage Current in MOS Devices. *IEEE transactions on electron devices*. 1993-10, vol. 40, no. 10, pp. 1888–1890. Available from DOI: 10.1109/16.277353.

62. LARCHER, Luca et al. A Model of the Stress Induced Leakage Current in Gate Oxides. *IEEE Transactions on Electron Devices*. 2001-02, vol. 48, no. 2, pp. 285–288. Available from DOI: 10.1109/16.902728.

63. FANO, Ugo. Ionization Yield of Radiations. II. The Fluctuations of the Number of Ions. *Physical Review*. 1947-07, vol. 72, no. 1, pp. 26. Available from DOI: 10.1103/PhysRev.72.26.

64. LOWE, BG. Measurements of Fano factors in Silicon and Germanium in the Low-Energy X-ray Region. *Nuclear Instruments and Methods in Physics Research Section A: Accelerators, Spectrometers, Detectors and Associated Equipment*. 1997-11-11, vol. 399, no. 2-3, pp. 354–364. Available from DOI: 10.1016/S0168-9002(97)00965-0.

65. EUXFEL. *XFEL Detector Tools' Documentation*. 2020. Available also from: https://in.xfel.eu/readthedocs/docs/pydetlib/en/latest/index.html. Revision 2f1352a2.

66. WELFORD, BP. Note on a Method for Calculating Corrected Sums of Squares and Products. *Technometrics*. 1962, vol. 4, no. 3, pp. 419–420. Available from DOI: 10.1080/00401706.1962.10490022.

67. IHLE, S et al. Direct Measurement of the Position Accuracy for Low Energy X-ray Photons with a pnCCD. *Journal of Instrumentation*. 2017-02-06, vol. 12, no. 02, pp. P02005. Available from DOI: 10.1088/1748-0221/12/02/P02005.

68. GROOM, Donald E et al. Passage of Particles Through Matter. *The European Physical Journal C-Particles and Fields*. 2000-03, vol. 15, no. 1, pp. 163–173. Available from DOI: 10.1007/BF02683419.

69. NISHIMURA, K et al. Design and Performance of the ePix Camera System. In: *AIP Conference Proceedings*. 2016-07-27, vol. 1741, p. 040047. No. 1. Available from DOI: 10.1063/1.4952919.

70. ZHANG, Jiaguo et al. Study of X-rayRradiation Damage in Silicon Sensors. *Journal of Instrumentation*. 2011-11, vol. 6, no. 11, pp. C11013–C11013. Available from DOI: 10.1088/1748-0221/6/11/c11013.

71. ZHANG, Jiaguo et al. Investigation of X-ray Induced Radiation Damage at the Si-SiO2 Interface of Silicon Sensors for the European XFEL. *Journal of instrumentation*. 2012-12, vol. 7, no. 12, pp. C12012. Available from DOI: `10.1088/1748-0221/7/12/c12012`.

72. ZHANG, Jiaguo et al. Study of X-ray Radiation Damage in the AGIPD Sensor for the European XFEL. *Journal of Instrumentation*. 2014, vol. 9, no. 05, pp. C05022. Available from DOI: `0.1088/1748-0221/9/05/C05022`.

73. SCHWANDT, J et al. Optimization of the Radiation Hardness of Silicon Pixel Sensors for High X-ray Doses using TCAD Simulations. *Journal of Instrumentation*. 2012-01, vol. 7, no. 01, pp. C01006. Available from DOI: `10.1088/1748-0221/7/01/c01006`.

74. SCHWANDT, Joern et al. Design and First Tests of a Radiation-Hard Pixel Sensor for the European X-Ray Free-Electron Laser. *IEEE Transactions on Nuclear Science*. 2014, vol. 61, no. 4, pp. 1894–1901. Available from DOI: `10.1109/TNS.2014.2304239`.

75. KLANNER, R. et al. Challenges for Silicon Pixel Sensors at the European XFEL. *Nuclear Instruments and Methods in Physics Research Section A: Accelerators, Spectrometers, Detectors and Associated Equipment*. 2013, vol. 730, pp. 2–7. ISSN 0168-9002. Available from DOI: `https://doi.org/10.1016/j.nima.2013.05.166`.

76. KOCH, Andreas et al. Performance of an LPD Prototype Detector at MHz Frame Rates under Synchrotron and FEL Radiation. *Journal of Instrumentation*. 2013-11-04, vol. 8, no. 11, pp. C11001. Available from DOI: `10.1088/1748-0221/8/11/C11001`.

77. JUNGMANN-SMITH, JH et al. Radiation Hardness Assessment of the Charge-Integrating Hybrid Pixel Detector JUNGFRAU 1.0 for Photon Science. *Review of Scientific Instruments*. 2015, vol. 86, no. 12, pp. 123110. Available from DOI: `10.1063/1.4938166`.

78. SOROKIN, Andrey A et al. An X-ray Gas Monitor for Free-Electron Lasers. *Journal of synchrotron radiation*. 2019-07, vol. 26, no. 4, pp. 1092–1100. Available from DOI: `10.1107/S1600577519005174`.

79. MALTEZOPOULOS, Theophilos et al. Operation of X-ray gas monitors at the European XFEL. *Journal of Synchrotron Radiation*. 2019, vol. 26, no. 4. Available from DOI: `10.1107/S1600577519003795`.

80. CANNY, John. A Computational Approach to Edge Detection. *IEEE Transactions on pattern analysis and machine intelligence*. 1986-11, no. 6, pp. 679–698. Available from DOI: `10.1109/TPAMI.1986.4767851`.

81. LEI, F et al. MULASSIS: A Geant4-Based Multilayered Shielding Simulation Tool. *IEEE Transactions on Nuclear Science*. 2002, vol. 49, no. 6, pp. 2788–2793. Available from DOI: `10.1109/TNS.2002.805351`.

82. PIA, MG et al. The Geant4 Toolkit: Simulation Capabilities and Application Results. *Nuclear Physics B-Proceedings Supplements*. 2003-09, vol. 125, pp. 60–68. Available from DOI: `10.1016/S0920-5632(03)90967-4`.

83. CHAUVIE, S et al. Geant4 Electromagnetic Physics. In: *Advanced Monte Carlo for Radiation Physics, Particle Transport Simulation and Applications*. Springer, 2001, pp. 153–158. Available from DOI: `10.1007/978-3-642-18211-2_26`.

84. CHAUVIE, S et al. Geant4 Low Energy Electromagnetic Physics. In: *IEEE Symposium Conference Record Nuclear Science 2004*. 2004, vol. 3, pp. 1881–1885. Available from DOI: `10.1109/NSSMIC.2004.1462612`.

85. WELLISCH, JP. Hadronic Shower Models in Geant4—the Frameworks. *Computer physics communications*. 2001-10-15, vol. 140, no. 1-2, pp. 65–75. Available from DOI: `10.1016/S0010-4655(01)00256-9`.

86. APOSTOL, Tom M. *Calculus, Volume 2*. New York: Wiley, 1967. ISBN 978-0-471-00007-5.

87. HED. *Scientific Instrument HED* [online]. 2021 [visited on 2021-05-05]. Available from: `https://www.xfel.eu/facility/instruments/hed/index_eng.html`.

88. MADSEN, A. et al. Materials Imaging and Dynamics (MID) instrument at the European X-ray Free-Electron Laser Facility. *Journal of Synchrotron Radiation*. 2021-03, vol. 28, no. 2, pp. 637–649. Available from DOI: `10.1107/S1600577521001302`.

List of Author's Publications

Scientific articles in peer reviewed (CC) journals

[I] KLAČKOVÁ, I., et al. Characterization of the ePix100a and the FastCCD Semiconductor Detectors for the European XFEL. In *Journal of Instrumentation*. Vol. 14, (2019), Art. no. C01008 [11] s. (2019: 1.454 - IF, Q3 - JCR Best Q, 0.805 - SJR, Q1 - SJR Best Q)

Cited in:

ROVEZZI, Mauro, et al. TEXS: In-Vacuum Tender X-ray Emission Spectrometer with 11 Johansson Crystal Analyzers. In *Journal of synchrotron radiation*, 2020, vol. 27, no., pp. 813-826. ISSN 0909-0495.

[II] **Submitted and in review process** KLAČKOVÁ, I., et al. Radiation Hardness Study of the ePix100 Sensor and ASIC under Direct Illumination at the European XFEL. In *Journal of Instrumentation.*

Published scientific contributions at international conferences

[III] JANUSCHEK, Friederike, KLAČKOVÁ, I., et al. Performance of the LBNL FastCCD for the European XFEL. In *2016 IEEE Nuclear Science Symposium, Medical Imaging Conference and Room-Temperature Semiconductor Detector Workshop*. IEEE, 2017, Art. no. 8069829 [3] s. ISBN 978-1-5090-1643-3.

Cited in:

MERCURIO, Giuseppe, et al. First Commissioning Results of the KB Mirrors at the SCS Instrument of the European XFEL. In *Advances in Metrology for X-Ray and EUV Optics VIII. International Society for Optics and Photonics*, 2019, vol. 11109, ISSN 0277-786X.

Published scientific contributions at domestic conferences

[IV] KLAČKOVÁ, Ivana - ŠAGÁTOVÁ, Andrea - FÜLÖP, Marko - NEČAS, Vladimír. Homogeneity of Electron Accelerator Dose Distribution. In *APCOM 2015 : Proceedings of 21st international conference on applied physics of condensed matter. Štrbské Pleso, Slovak Republic. June 24-26, 2015*. vol. 1 Bratislava : STU, 2015, S. 248-251. ISBN 978-80-227-4373-0.